# Mixing kinematics in granular materials using x-ray rheography.

DIKSHIT BABU NEPAL

THE UNIVERSITY OF SYDNEY

Supervisor: Prof. Itai Einav
Associate Supervisor: Dr. James Baker

A thesis submitted in fulfilment of
the requirements for the degree of
Doctor of Philosophy

School of Civil Engineering
Faculty of Engineering
The University of Sydney
Australia

2 September 2025

## Statement of originality

I confirm that, to my knowledge, this thesis is my original work and has not been submitted for any degree or other purpose. The intellectual content is entirely my own, with all assistance and sources appropriately acknowledged.

Grammarly and generative AI tools, such as OpenAI's ChatGPT, helped me with sentence structure, spell-checking, and formatting. However, the research, concepts, analysis, and findings are my own. I take full responsibility for the thesis submitted, ensuring that it is my original work and that I have used generative AI within the allowed guidelines.

Dikshit Babu Nepal

# Abstract

This dissertation introduces a novel method for understanding granular mixing kinematics through high-speed X-ray observations. It contains three interlinked main chapters, each addressing key challenges and building upon the previous ones to enhance our understanding of mixing kinematics in cylindrical mixers.

The first chapter uses the X-ray rheography image analysis method to determine internal velocity fields in antisymmetrical granular flows, such as those in a two-bladed impeller mixer. This chapter highlights the significant role of X-ray sources and detector alignment in capturing antisymmetric flow characteristics, setting a methodological basis for subsequent chapters.

The second chapter is focused on creating an experimental setup and framework for examining granular mixing dynamics via X-ray rheography. A granular mixer was designed for X-ray imaging from three orthogonal views. The experimental results obtained using the rheography method were compared with those from the discrete element method (DEM) simulations, which replicated the experimental mixing scenarios studied to evaluate the effectiveness of X-ray rheography in the analysis of mixing kinematics. This chapter establishes the foundation for an extensive investigation of mixing kinematics for different particle shapes in the third chapter.

The third chapter examines the influence of the particle shape and impeller blade angle on mixing kinematics. We examine 3D velocity fields and fabric orientation by mixing spherical glass beads, slightly elongated barley, and long jasmine rice. Our findings indicate that elongated particles align along their main principal axis, which impacts their mixing kinematics, while spherical particles, being axisymmetric, exhibit no notable alignment. DEM simulations confirm these findings, emphasising the effectiveness of the X-ray method in studying the internal mixing kinematics of diverse particle shapes.

# Acknowledgement

I gratefully acknowledge the Faculty of Engineering for their generous provision of the scholarship and stipend, which have been essential in supporting my doctoral studies.

I would like to thank my supervisors, Professor Itai Einav, Dr. James Baker (now at Liverpool John Moores University) and Dr. Francois Guillard (who has supported me as an associate supervisor in James' absence), whose support and expertise have been crucial in advancing this research. I also thank my thesis committee for their feedback, which has refined my study. I appreciate Dr. Benjy Marks, Associate Professors Yixiang Gan and Mohammad Saadatfar, Dr. Sudip Laudari, and the Granular group for enriching our meetings and my academic experience. I extend my appreciation to the faculty and staff of the Civil Engineering Department for their commitment and especially to Todd Budrodeen for technical support with the experimental setup.

My gratitude extends to my family, Mummy, Buwa, and sister Dikshya/ Sharad/ Rihan, for their unwavering support. I am especially grateful to my wife, Prakriti Pokhrel, for her love and faith. I also thank Mamu, Papa, Akriti didi, and Abhishek dai for their blessings. My appreciation extends to The Marphas, my cricket family, for supporting my well-being, and to brothers/sisters/friends and colleagues for their continuous support and presence during this experience. Lastly, for everyone who has influenced my PhD journey, your encouragement has been pivotal.

# Contents

CHAPTER 1

# Introduction

Granular materials are essential in industries such as mining, civil engineering, and glass production (Bridgwater 2003; Shinbrot et al. 2006; Muzzio et al. 2003; Havlica et al. 2015). They are also used to produce everyday products, such as bread, cakes, and medicine. The products we consume and use are the result of mixing various granular materials. For example, in the pharmaceutical industry, drug production involves mixing particles of different sizes and shapes in a mixer to achieve a homogeneous mixture. Many questions arise when it comes to the homogeneity of the mixture, such as what makes a good mix, whether it is necessary to have the correct quantity of ingredients, whether it is essential to mix the particles completely on a microscopic level, and whether the granular mixing pattern depends on the size and shape of particles and its interaction with the impeller blades of the mixers. A lack of proper understanding of the mixing process could result in varying doses among different batches of the same product, posing a serious threat to the safety of patients who consume the finished product. To overcome such a problem, a deeper understanding of how the granular media mix is crucial.

The physics of granular media is complex, making the study of granular mixing challenging. At the particle level, intricate interactions occur due to friction when individual particles come into contact (Andreotti et al. 2013). As the number of particles in a mixture increases, the complexity of their interactions also increases, making monitoring the behaviour of each grain impractical, especially on an industrial scale. Although it is possible to describe these media using continuum models, the need to distinguish between the microscopic scale of individual grains and the macroscopic statistical scale raises concerns about the accuracy of these continuum descriptions. In addition, the variability of the size and shape of the granular materials (see Figure 1.1) induces heterogeneity and intricate dynamic alignments within the samples (Guillard et al. 2017), complicating the prediction of behaviour. This emphasises the

FIGURE 1.1: Examples of granular media (Andreotti et al. 2013)

need for a deeper understanding of mixing kinematics to predict and optimise the mixing of these materials effectively.

A few studies have investigated mixing kinematics using camera images captured through transparent walls or open surfaces. Particle image velocimetry (PIV) is the most widely used technique to measure flow velocity fields from such images (e.g. Lueptow et al. 2000; Sanvitale and Bowman 2016). When integrated with camera images, the PIV technique lays a solid foundation for experimental research in this field (Conway et al. 2005; Lekhal et al. 2006). Pictures taken from the surface can offer valuable insights; however, because granular materials are opaque, the conclusions drawn from these studies do not directly represent the overall behaviour in the bulk of the studied problem. In particular, such granular materials exhibit different behaviours near boundaries due to the formation of boundary layers (Rognon et al. 2015; Miller et al. 2013). Thus, relying solely on external observations to explain mixing kinematics can be misleading. An alternative method, positron emission particle tracking (PEPT), has also been used to study particle motion and mixing (Marigo et al. 2013). Although PEPT offers valuable insights into internal mixing kinematics, it has some limitations. The need for radiolabelled particles can restrict its application. In addition, the behaviour of tracer particles may not accurately represent the bulk material if there are differences in size, density, or interactions with the medium.

Alternative techniques to examine internal granular flow include refractive index matched scanning (RIMS) observations (Wiederseiner et al. 2011, Dijksman et al. 2012, Brodu et al. 2015), magnetic resonance imaging (MRI) (Nakagawa et al. 1993, Ehrichs et al. 1995, Kawaguchi et al. 2006) and ultrasonic imaging (Han et al. 2016). RIMS can capture dynamic

conditions; however, it requires a viscous fluid with a refractive index that matches that of particles, which can alter the characteristics of natural flow (Huang et al. 2005, and Rognon et al. 2011). Other methods, such as MRI and ultrasonic imaging, face cost, safety, resolution, and invasiveness challenges. Due to these experimental challenges, discrete element method (DEM) simulations (Boonkanokwong et al. 2016, Remy et al. 2009, Hare and Ghadiri 2013, Capece et al. 2015, and Guo et al. 2017) are commonly used to explain the mixing kinematics of bulk materials. However, these simulations come with limitations. They frequently depend on simplifying assumptions that may not accurately represent real grain behaviour and cannot handle the large number of particles involved in large-scale problems.

X-ray computed tomography (CT) (Kou et al. 2017, Saadatfar et al. 2012, Athanassiadis et al. 2014, Taillandier-Thomas et al. 2016, Desrues et al. 1996, Mueth et al. 2000, Hall et al. 2010, Hasan and Alshibli 2010, and Grudzień et al. 2011) is commonly used in geoscience to build 3D maps of the density of granular materials (Morin 1988, Baxter et al. 1989, Royer et al. 2005). A key advantage of the X-ray technique is minimising the effects of boundary layers on kinematic measurements (Nedderman and Laohakul 1980). However, X-ray CT is limited in capturing quasi-static deformations because of the time delays associated with incremental loading and the need to rotate the sample to obtain 3D information. Predicting internal kinematics effectively requires high-temporal-resolution imaging capable of capturing rapid changes without interrupting the process. These limitations make traditional X-ray CT unsuitable for applications involving continuous flow or for investigating grain kinematics around impellers in continuous mixing processes.

Recent technological advances have enabled the collection of consecutive radiographs at high frame rates, facilitating the study of continuous flow. To this end, high-speed radiography has been used in the investigation of Newtonian fluids (Lee and Kim 2003, Lee et al. 2014) and granular flow (Guillard et al. 2017), whereby the focus is on analysing the beam-averaged flow of the entire bulk in the projected sense. X-ray radiographs taken to capture continuous flow present two main benefits: They enable beam- and time-averaged assessments of particle orientation during flow using the Fourier transform method (Guillard et al. 2017). Second, while these radiographs do not provide direct depth information, they are instrumental in analysing out-of-plane velocity distributions through deep velocimetry (Baker and Einav 2021).

This technique offers more detailed information than traditional PIV. By incorporating out-of-plane velocity data from orthogonal scanning angles and applying a Sudoku-based optimisation method (Baker et al. 2018), it becomes possible to estimate internal velocity fields. Furthermore, capturing radiographs from three orthogonal directions enables the reconstruction of three-dimensional velocity fields. This X-ray rheography approach provides a non-invasive means of measuring internal velocities, making it a powerful tool for studying dense granular flows.

Examining the kinematics of granular mixing is complex, and conducting experimental analyses using X-ray rheography carries various challenges. These challenges include: 1) acquiring clear radiographs from three orthogonal angles can be problematic due to a motorised blade positioned at the centre of the mixer, which could obstruct the X-ray; and 2) previous studies indicate that two-blade mixers can produce antisymmetrical granular flows (Bai et al. 2017). In such a situation, it is imperative to determine the correct X-ray orientation to reconstruct the optimal velocity field. Thus, taking into account the identified technical challenges and research gaps, this study aims to:

(1) Develop and construct an experimental granular mixer to investigate the kinematics of mixing via X-ray rheography.
(2) Examine the applicability of X-ray rheography to analyse the mixing kinematics of granular materials around impellers.
(3) Study how the angles of the impeller blades affect the flow of different-shaped granular materials.

To achieve these research goals, the subsequent chapters of this thesis consist of five additional sections, each focused on specific objectives.

- Chapter 2 reviews current research on the mixing kinetics of granular materials, considering both experimental and computational methods.
- Chapter 3 investigates the impact of antisymmetry of flow patterns during mixing with two impeller blades. This chapter aims to create a numerical model of idealised antisymmetric flow and use it to produce artificial X-ray projections, with which we analyse and then determine the correct X-ray orientation for optimal results.
- Chapter 4 is centred on the design of a granular mixer for X-ray investigation and its experimental evaluation. This section compares the kinematic results from mixing

experiments with those predicted by a DEM model of the same granular mixing problem.

- Chapter 5 delves into how the angle of the impeller blade affects mixing kinematics and the fabric orientation field when mixing various particle shapes, including spherical and elongated particles.
- Lastly, Chapter 6 will discuss and summarise the findings and limitations of the study.

CHAPTER 2

# Literature review

This chapter reviews some of the experimental and computational methods previously developed and used to explain the kinematics of granular mixing. It presents a range of techniques, such as conventional photography, particle image velocimetry (PIV), positron emission particle tracking (PEPT), magnetic resonance imaging (MRI), refractive index matching scanning (RIMS), and the discrete element method (DEM). Although traditional experimental methods have greatly improved our understanding of flow patterns and mixing kinematics, they often face challenges, especially in explaining three-dimensional internal flows in opaque granular systems. Other advanced non-destructive test techniques contributing to better insights into bulk dynamics also usually experience issues related to low spatial resolution, low temporal resolution, lengthy processing times, or the need for specialised experimental setups. This situation underscores the benefits that may arise from developing novel non-invasive observation technologies dedicated to granular flow problems, especially methods engineered to investigate granular mixing. The last part of this chapter examines how X-ray technology can be used to uncover internal kinematics in granular mixing.

## 2.1 Overview

The mixing of granular materials is essential in industries such as ceramics, construction and pharmaceuticals (Bridgwater 2003; Shinbrot et al. 2006; Muzzio et al. 2003; Havlica et al. 2015). Standard mixing apparatuses involve rotating cylinders and stirred tanks typically equipped with one or more blades (Stewart et al. 2001; Laurent et al. 2000). Understanding the mixing kinematics is critical to improving the mixing efficiency in various industrial applications. Thus, studies have demonstrated great innovations in this field, with most of the research focussing on methods to optimise the particle mixing process (Liu et al. 2017, Sanvitale et al. 2022,

Ottino and Khakhar 2000). In contrast, few other research studies are based on understanding the physics behind mixing kinematics in stirred vessels. These scientific investigations have revealed intricate patterns, including particle heaps (Bagster and Bridgwater 1967) that circulate before the stirring blade. Despite this knowledge, particle flow behaviour in a stirred vertical cylinder remains unclear, motivating this project's in-depth exploration.

## 2.2 Experimental methods

This section summarises previous studies on mixing kinematics, focussing on findings from basic photographic observations to more sophisticated experimental techniques.

### 2.2.1 Photographic images

The flow patterns in a vertical cylinder stirred by a flat blade were studied using conventional photography of the bed walls of the mixers (Bridgwater et al. 1969, Bagster and Bridgwater 1967). These studies demonstrated that particles form a heap in front of the blade, rising and rolling into the discharge area behind it (see Figure 2.1). These flow patterns change (see Figure 2.2) depending on the volume of the particle bed.

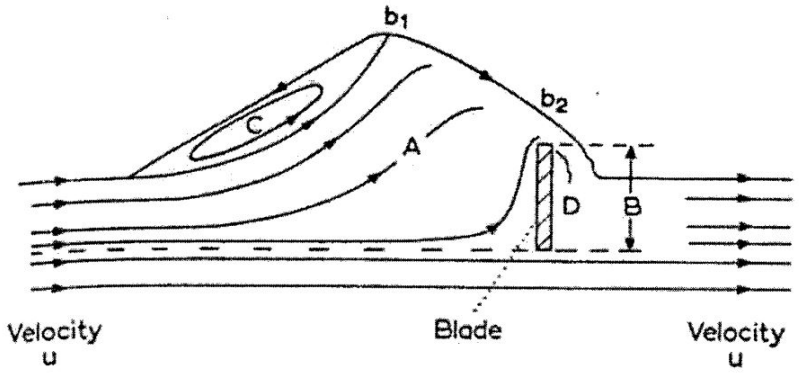


FIGURE 2.1: Granular flow over a stationary blade includes a rising region (A), recirculating region (B), discharge region (D), and discharging free surface (bl-b2) (Bridgwater 1976).

In addition, factors such as blade velocity, sample height, and blade angle influence the recirculating flow patterns around the pile ( Novosad 1964). A similar study ( Novosad 1968) used coloured layers in dissection beds to observe particle movement near the outer edge of a

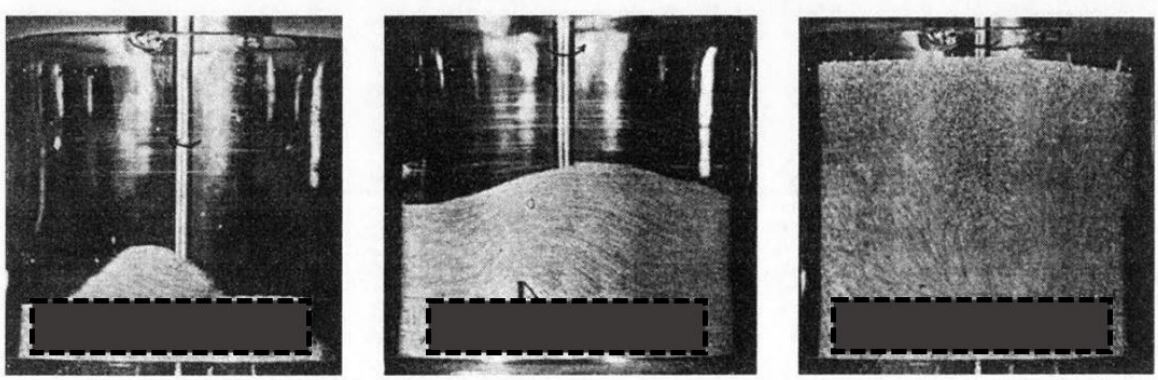

FIGURE 2.2: Particle flow patterns in a vertical cylindrical mixer are photographed through transparent walls. The images capture mixed materials (Novosad 1964), with a rectangular border showing the blade area.

blade, primarily providing qualitative information. However, the exact quantitative effects of these factors are not well understood.

### 2.2.2 Particle image velocimetry (PIV)

Researchers used PIV, a noninvasive technique, to analyse velocity fields to gather quantitative data on granular mixing, marking a significant advancement in the field. PIV is an optical technique that measures surface kinematics by analysing consecutive digital images. By analysing the displacement of particles in the images, PIV generates two-dimensional velocity fields at various times and locations within the flow. Advanced techniques based on PIV, such as stereoscopic PIV ( Prasad 2000), dual-plane stereoscopic PIV ( Kähler and Kompenhans 2000), scanning planar PIV ( Brücker 1997), tomographic PIV ( Elsinga et al. 2006), and holographic PIV ( Katz and Sheng 2010), utilise multi-plane approaches to capture volumetric data for three-dimensional displacements. Furthermore, by using multiple cameras, the volumetric particle tracking velocity (Bhattacharya and Vlachos 2020) was used to track the three-dimensional positions of individual particles over time. The PIV method captures detailed velocity fields without disturbing the flow (Westerweel et al. 2013) and has been used primarily for transparent fluids. These studies have established guidelines for the PIV method to ensure accurate fluid flow measurements (Keane and Adrian 1992). These guidelines can also be applied to optical imaging of dense granular flows (Lueptow et al. 2000).

In the study by Lekhal et al. 2006, PIV was used to investigate the granular mixing (see Figure 2.3). This research integrates camera imaging and PIV techniques to provide some quantitative insight into the dynamics of granular mixing. The camera imaging captures the formation of peaks and valleys on the surface of the granular bed as the blade agitates the material (see Figure 2.4).

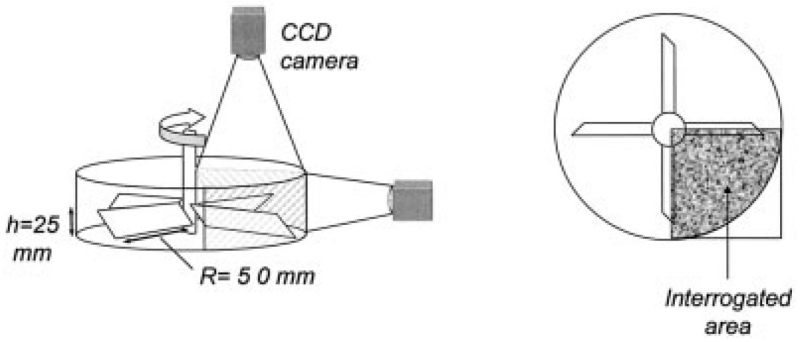


FIGURE 2.3: Four-blade agitated bed geometry. Hatched regions are interrogated by PIV (Lekhal et al. 2006).

PIV analysis of these images reveals that the primary flow occurs before the blade, driving the movement of the grains. Behind the blade, wake interactions create slopes that converge at a sink point, characterised by near-zero velocity, which indicates flow recirculation and energy dissipation in specific areas. Together, these methods highlight critical flow characteristics and structural changes during mixing. However, these studies predominantly focus on flow boundaries due to the opacity of the grains and do not capture the internal dynamics within the mixer. Although we can quantitatively measure the flow at the surface and boundary using this method, it is uncertain whether these observations truly reflect bulk behaviour.

The challenge of measuring internal motion limits the effectiveness of PIV and camera images in situations where surface and internal flows may differ (Slominski et al. 2007), highlighting the need for a much more advanced experimental method to infer three-dimensional internal information.

### 2.2.3 Magnetic resonance imaging (MRI)

MRI is widely recognised for its role in medical diagnostics (Katti et al. 2011) and has also become a valuable non-invasive tool in scientific research. Using magnetic fields and radio

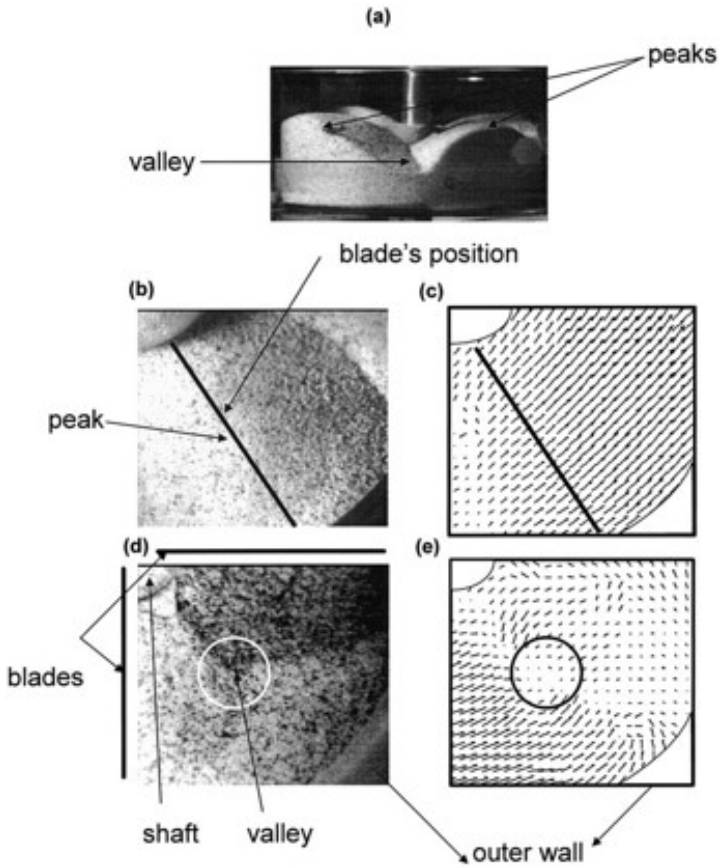


FIGURE 2.4: Instantaneous views of the agitated mixer: (a) Side view; (b) Peak; (c) PIV at b; (d) Valley; (e) PIV at d (Lekhal et al. 2006).

waves, MRI produces highly detailed 3D images that enable researchers to visualise and study complex systems in granular media (Hill et al. 1997b, Hill et al. 1997a). Several studies have successfully used MRI to investigate the flow behaviour of granular materials (Stannarius 2017, Nakagawa et al. 1993), revealing important information on their bulk dynamics. However, the MRI technique has inherent limitations when applied to granular systems. The MRI technique is restricted by its long image acquisition time and the requirement of carbon-based particles. These limitations hinder its effectiveness in studying fast and dynamic granular mixing that requires high temporal precision.

### 2.2.4 Refractive index matched scanning (RIMS)

RIMS is a technique that involves immersion of transparent particles in a fluid that has the same refractive index as the particles, making the solid medium transparent and allowing optical

access to most of the granular material (Dijksman et al. 2012). A laser sheet is used to illuminate a section of the fluorescently labelled fluid phase in the suspension, which has been matched for refractive index to perform RIMS. The laser sheet is sequentially moved through different sections of the grain-fluid medium, capturing images at various depths. Although this process allows us to reconstruct detailed 3D images of the entire sample, the major technical challenge with RIMS involves identifying an appropriate solvent for index matching (Dijksman et al. 2012). Furthermore, while RIMS-based methods are relatively straightforward for visualisation tasks involving only a few fluid-solid interfaces, they become considerably more complex as the number of interfaces increases significantly (Wiederseiner et al. 2011). In addition, introducing interstitial fluid can change the mixing pattern as the much-elevated viscosity of the index-matched fluid relative to air or water hinders the motion of the particles in the bed.

### 2.2.5 Positron emission particle tracking (PEPT)

Positron emission particle tracking (PEPT) is a nuclear imaging method widely used in various scientific fields such as physics, chemical engineering, mechanical engineering, nuclear engineering, and civil engineering (Windows-Yule et al. 2022). PEPT is a widely recognised tool for studying granular flow by precisely tracking the position and trajectory of individual particles with high spatial and temporal resolution, even in multiphase, large, dense and optically opaque environments (Pellico et al. 2024). This enables researchers to investigate granular mixing more accurately than most other techniques, revealing the behaviours affecting bulk flow.

In an experimental study aimed at investigating mixing kinematics using PEPT (Stewart et al. 2001), findings regarding the velocity field components, namely tangential, radial and axial velocities, are explained (see Figure 2.5). The results indicate that the particles exhibit circular motion near the base with minimal radial movement. In areas with higher piles of material, the particles flow toward the shaft or move away from it, depending on the height of the pile. The study also explains how the particles interact with the mixer blades: Most particles rise, recirculate, or fall over the blades, and this recirculation occurs without forming bulk cavities.

Although PEPT offers valuable insights into the kinematics of mixing processes, it also has limitations. Despite its high resolution and the capability to track the trajectory of a single

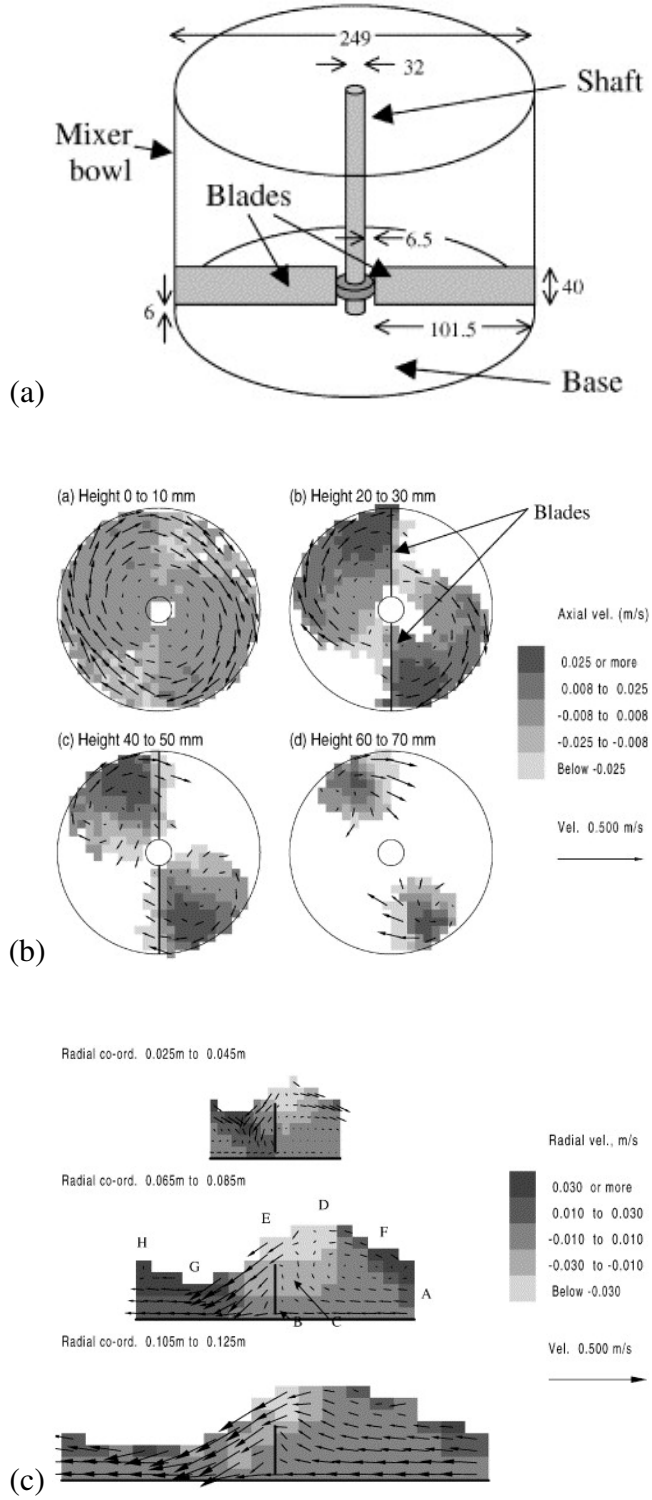


FIGURE 2.5: Study using PEPT (Stewart et al. 2001) showing a) the mixer diagram, b) Visualisations of the radial velocity on horizontal cross-sections (tangential and radial components), and c) cylindrical cross-sections (tangential and axial components).

positron emitting tracer, PEPT can be constrained by the necessity of radio-labelling particles (Windows-Yule et al. 2022). In addition, the behaviour of tracer particles may not perfectly represent the bulk material, particularly if there are significant differences in size, density, or interaction with the surrounding medium.

## 2.3 Discrete element method (DEM)

High-performance computing has made DEM a powerful tool for studying the dynamics of granular mixing. DEM allows for a detailed representation of the particle trajectories and measurement of important variables that govern the mixing process at the microscopic scale (Liu et al. 2017, Zhou 2002). For simulations using the soft-sphere DEM model (also known as time-stepping simulations), Newton's equations of motion are numerically integrated over time for each particle, starting from an initial system configuration. Assuming a sufficiently small time step for integration, a particle's state is only influenced by contacts with its neighbours and the gravitational force. Therefore, at any given time step, the DEM considers only pairwise interactions of neighbouring particles or between a particle and a boundary as

$$m_i \frac{dv_i}{dt} = \sum_j \left(F_{ij}^N + F_{ij}^T\right) + m_i g, \tag{2.1}$$

$$I_i \frac{d\omega_i}{dt} = \sum_j (R_i \times F_{ij}^T) + \tau_{rij}, \tag{2.2}$$

where, $m_i$, $v_i$, $I_i$, $\omega_i$, and $R_i$ represent the mass, linear velocity, moment of inertia, angular velocity, and radius of particle $i$, respectively. The gravitational acceleration is denoted by $g$. The normal and tangential forces that arise from the interaction between particles $i$ and $j$ are represented by $F_{ij}^N$ and $F_{ij}^T$, respectively. Furthermore, the term $\tau_{rij}$ accounts for the influence of rolling friction, indicated by $\mu_r$ (Ai et al. 2011).

DEM was used to simulate glass beads in a vertical mixer with a rotating blade, with results compared to experimental data gathered via PEPT (Stewart et al. 2001), showing a strong correlation and confirming the predictive capabilities of the simulation. A study on the effect of the number of impeller blades on the granular flow dynamics in bladed mixers provided vital insight into optimising the design to achieve better mixing efficiency and particle uniformity (Boonkanokwong et al. 2016). Furthermore, research using cohesionless spherical

glass beads in a cylindrical vessel with a four-blade impeller examined the impact of blade pitch and particle friction on granular flow (Remy et al. 2009), finding that an obtuse pitch significantly improved vertical and radial mixing by forming a robust 3D recirculation zone.

Another study on particle flow dynamics at varied bed heights (Zhou 2002) revealed height-dependent behaviours (see Figure 2.6). In the bed's lower section, particles mainly moved circular, with peak velocities at blade fronts, tapering off further away, while near blade rears, velocities were high but less directionally constrained. The midbed particle flow mirrored the bottom but with high velocities at the flow front due to the descending of particles along the heap's surface. At the top, the particles flowed downward, driven by the motion below, while wall interactions prompted an inward radial flow.

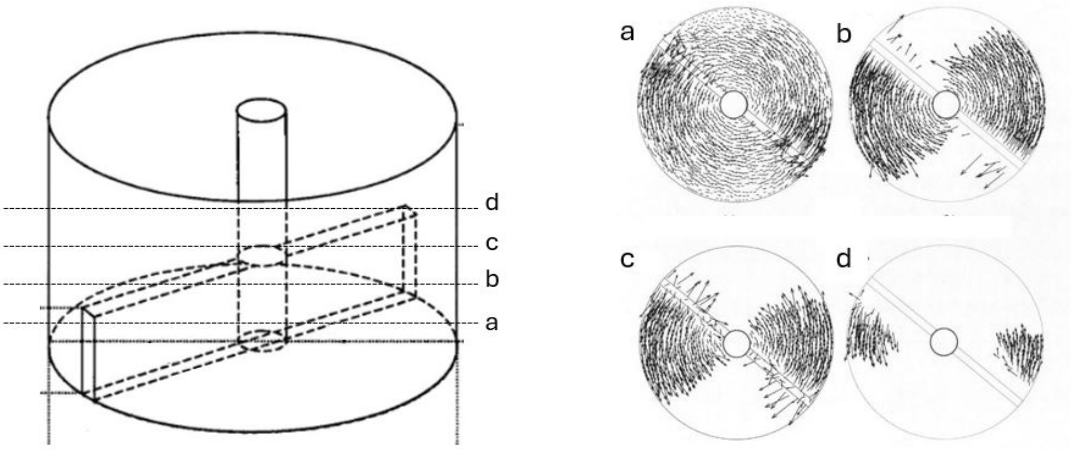


FIGURE 2.6: Study using DEM (Zhou 2002) showing a) the mixer diagram, b) Radial velocities of particles projected on horizontal cross-sections at different height: a) h = 10 mm; b) h = 30 mm; c) h = 45 mm; d) h = 65 mm

Several studies explored how particle characteristics, such as Young's modulus (Alizadeh et al. 2014) and static friction coefficient (Stewart et al. 2001, Zhou et al. 2004, Zhou et al. 2003), impact dynamics in rotating drums, identifying them as vital to velocity profiles and mixing kinematics. PIV and DEM showed that the increase in roughness on the surface of the particles led to nonuniform flows (Remy et al. 2010b). DEM modelling of the mixing of spherical glass particles in a vertical mixer with two flat blades demonstrated a significant influence of rotation speed on the dynamics of granular flow (Havlica et al. 2015). The study of rotational speed and the effect of fill level on particle circulation showed a direct correlation

between speed and circulation and an inverse relationship between fill level (Tahvildarian et al. 2013). The large-scale DEM compared spherical and polyhedral particles (Govender et al. 2018), noting faster mixing rates with spherical particles. Another investigation revealed particle velocities scaled with mixer size and blade speed above a threshold (Remy et al. 2010a).

DEM simulations have deepened our understanding of mixing kinematics, offering detailed insights into particle-level interactions. However, their practicality is limited by the high computational costs associated with large systems and the reliance on simplified contact models that may not fully capture the complexities of real granular flows. Beyond the modelling of spherical particles in air, the accuracy of DEM models is hindered. Finally, it should be remembered that DEM can only offer a (very useful) model of what is happening within granular mixers, which, at any rate, require validation against experiments.

## 2.4 Addressing the gap

X-ray imaging has surpassed traditional techniques and offers significant advantages in studying granular systems. Specifically, X-ray computed tomography (CT) enables three-dimensional cross-sectional visualisations, making it useful to understand granular materials (Mathews et al. 2017; Kou et al. 2017; Hall et al. 2010; Saadatfar et al. 2012; Athanassiadis et al. 2014; Taillandier-Thomas et al. 2016). X-ray CT is effective for static analyses but has limitations for our dynamic research. Enhancing high-resolution, non-invasive imaging for dynamic studies could greatly improve our insight into granular mixing in dense systems.

CT scans often take seconds or minutes to capture complete image sets. In contrast, high-speed radiography can provide a solution by capturing rapid sequences of radiographic images to track fast movements. Recent technological advances have achieved frame rates suitable for continuous-flow studies, which are applicable to Newtonian fluids (Lee and Kim 2003; Lee et al. 2014) and granular flows (Guillard et al. 2017). This highlights the capability of high-speed radiography to capture dynamic behaviours.

Although X-ray CT offers detailed 3D visualisations, it typically requires radiographs from more than three angles for a full reconstruction. This limitation can be addressed by using high-speed radiography from just three orthogonal projections to recover the three-dimensional internal velocity fields, a method known as X-ray rheography (Baker et al. 2018). These

advanced techniques are essential for studying granular flows, where the acquisition of 3D information is necessary but is challenging with traditional methods.

### 2.4.1 Deep velocimetry and X-ray rheography

X-ray radiographs provide depth-integrated projections of a sample, offering a different perspective than planar imaging (see Figure 2.7). Although these two-dimensional images do not convey explicit depth details, they can reveal velocity variations that occur perpendicular to the imaging direction. This is particularly useful for systems experiencing significant out-of-plane changes.

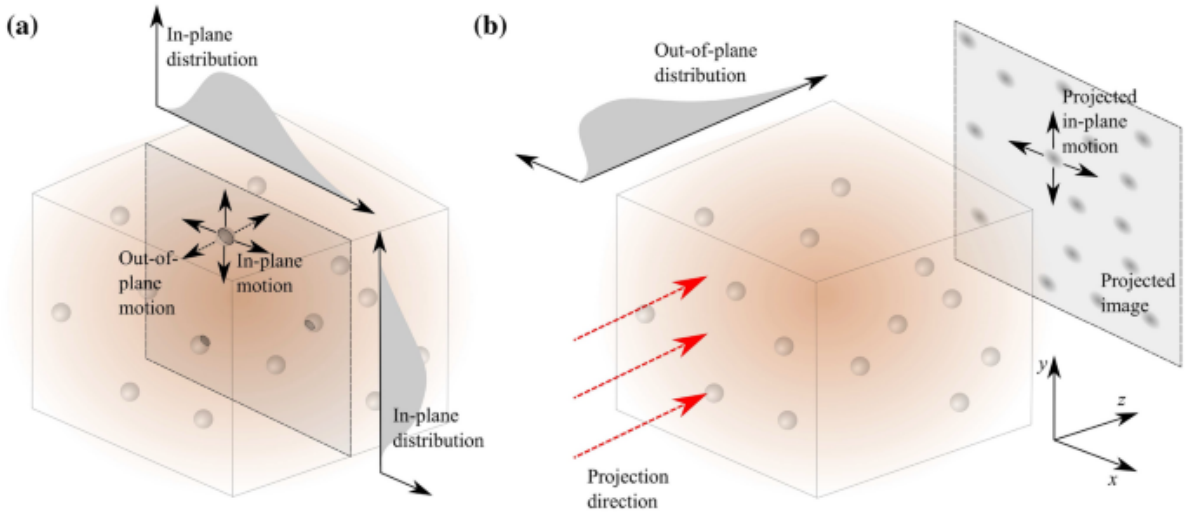


FIGURE 2.7: Imaging systems showing differences between regular particle image velocimetry (PIV) and X-ray imaging: a) In a typical PIV setup, a single slice of a 3D volume records the movement of material in two in-plane directions. Out-of-plane motion causes material to move in and out of the field of view. The variation along the two in-plane directions results in in-plane distributions; and b) X-ray imaging system captures the material from the entire out-of-plane path of the projection, where variations along the out-of-plane direction result in out-of-plane distributions (Baker and Einav 2021).

Deep velocimetry (Baker and Einav 2021) reconstructs velocity distributions (see Figure 2.8 a) from sequential projections, accounting for out-of-plane variations captured in successive X-ray images. Initially, radiographs are divided into windows for image correlation, enabling the derivation of displacement probability density functions (PDF) through deconvolution. Similarly to representative volume elements in continuum mechanics, material properties

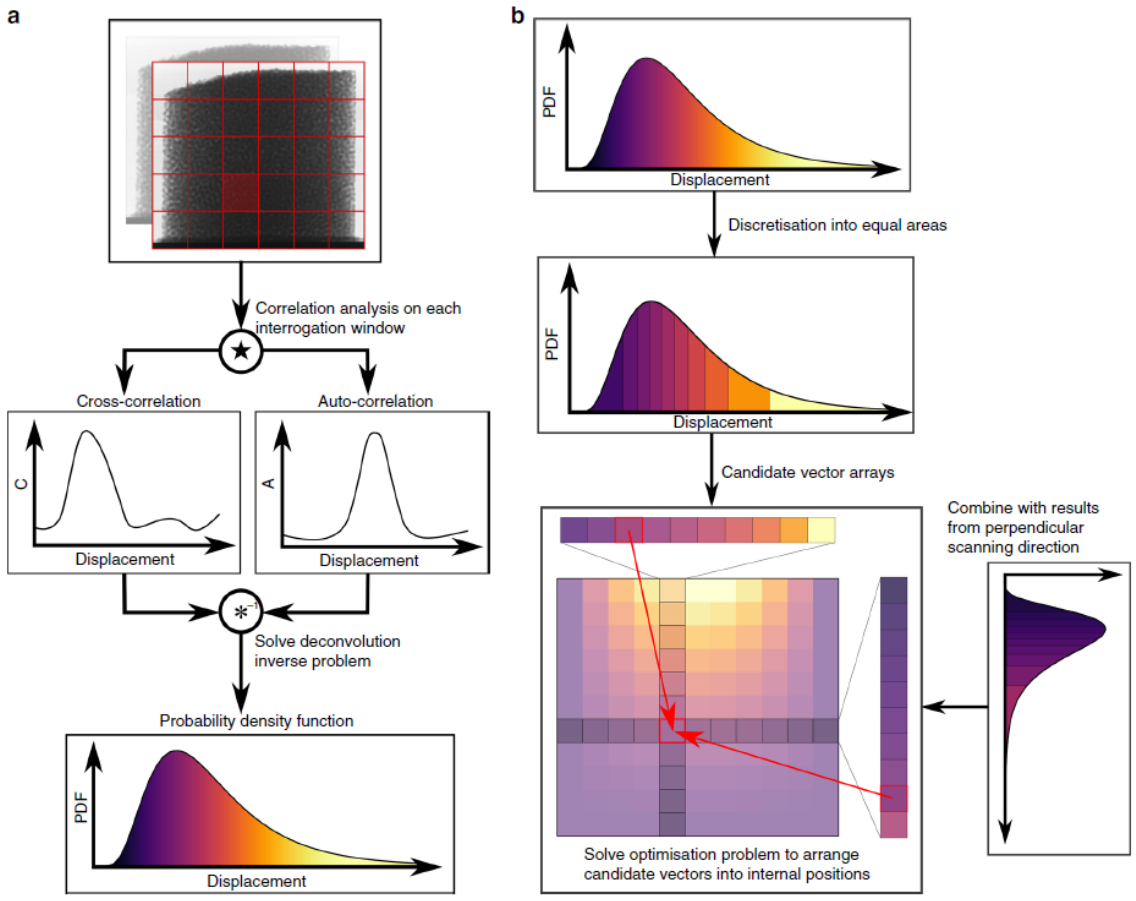


FIGURE 2.8: Process of velocity reconstruction. a) The initial pair of radiographs (top) is segmented into interrogation windows (red grid), followed by conducting image correlation analysis on each window (middle) to derive the probability density function (PDF) of displacements within it (bottom). b) The displacement PDFs are discretised into potential vectors, and the outcomes are combined with orthogonal directions to fit potential arrays into the internal grid positions. (Baker et al. 2018)

within each interrogation window are assumed to be uniform. When analysing projected images, the window $W$ must be selected such that the velocity profile does not exhibit strong spatial variations in the plane and the density profile remains approximately constant at different positions within the limits defining the window.

The velocity distributions obtained through deep velocimetry facilitate the measurements of internal granular flow (see Figure 2.8 b) using X-ray rheography (Baker et al. 2018). Displacement PDFs are discretised into vectors and compared across discretised vectors from

perpendicular directions to identify matching pairs through optimisation, akin to solving a Sudoku puzzle. However, significant errors can often occur during the deconvolution and matching stages. Several key factors must be considered to improve the precision of granular flow measurements by rheography, including the number of images collected for the PDF displacement derivation and the size of the analysis window. Increasing the number of images can reduce errors but also elevate computational demands. Larger windows improve accuracy, and using a fine mesh helps keep discretisation errors low. The optimisation process aims to minimise matching errors in observations, with more iterations contributing to reduced errors.

### 2.4.2 Fabric study

Understanding fabric orientation is essential for studying mixing kinematics in both industrial and natural environments. The various shapes of particles in granular materials lead to complex dynamic alignments (Guillard et al. 2017) that require advanced experimental and numerical techniques for accurate analysis. Different DEM approaches can model non-spherical particles, but come with computational challenges. For example, the multisphere (MS) technique represents complex shapes using overlapping spheres to accommodate various geometries (Abbaspour-Fard 2000; Kremmer and Favier 2001), but this significantly increases computational costs. The polyhedral particle approach uses polygonal shapes to improve shape precision; however, it complicates the calculation of contact forces (Cundall 1988).

In scenarios where shape accuracy and computational efficiency are required, the superquadric particle (Barr 1981) model implemented in LIGGGHTS (Kloss et al. 2012, Podlozhnyuk et al. 2017) offers smooth surfaces for non-spherical particles. This model ensures computational efficiency and allows for better control of the shape parameters, effectively balancing realism with computational demands. Despite these advances, numerical simulations still require experimental validation to confirm reliability.

X-ray radiography can play a crucial role in validating DEM results by minimising the boundary effects near the container walls, which proves essential for studying granular flow. Dynamic X-ray radiography combined with Fourier transformation (see Figure 2.9) provides insights into fabric orientation, emphasising how shape anisotropy influences the development of granular fabric (Guillard et al. 2017). This method could be invaluable for validating

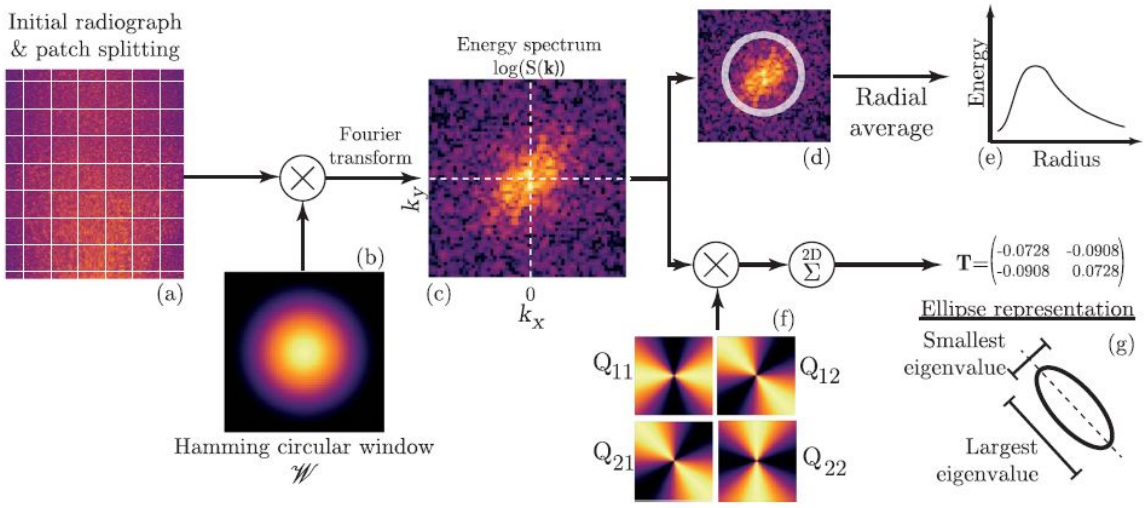


FIGURE 2.9: Steps for the fabric determination technique (Guillard et al. 2017). From left to right: (a) Extraction of patches from a radiograph. (b) Application of a circular Hamming window to the patches. (c) Computation of the two-dimensional Fourier transform, yielding the power spectrum. Two parallel processing approaches follow: Top row: (d) Summation of the spectrum over circular shells to obtain (e) the energy distribution function as a function of radius. Bottom row: (f) Multiplication of the spectrum by the orientation matrix, followed by summation over all wavevectors, yielding a symmetric matrix, which (g) can be visualised as an ellipse defined by its eigenvalues (shape) and eigenvectors (orientation).

DEM models and enhancing our understanding of fabric orientation. However, it is limited to information in the projected depth.

## 2.5 Summary

This chapter briefly reviews experimental tools for studying granular mixing kinematics, with a focus on conventional photography, particle image velocimetry (PIV), positron emission particle tracking (PEPT), magnetic resonance imaging (MRI), and X-ray computed tomography (X-ray CT). The benefits and limitations of each technique are assessed. In addition, we discuss recent advances in X-ray imaging with the X-ray rheography technique employing deep velocimetry, emphasising their potential as innovative approaches for investigating granular mixing kinematics. We also investigated the application of X-ray radiography for examining fabric orientation.

CHAPTER 3

# Exploring anti-symmetric granular flows with X-ray rheography

---

Using the X-ray rheography technique, we can derive internal velocities to study the kinematics of granular flow. This chapter demonstrates that the effectiveness of this technique in the study of antisymmetric granular flow depends on the alignment of the X-ray equipment that captures the flow properties in radiographs. In antisymmetrical granular flows, the flow patterns mirror across a defined axis, resulting in opposing flow phenomena on either side. In such cases, it is demonstrated that aligning the X-ray source and detector along the line of antisymmetry fails to reconstruct the velocity field using the image analysis method of X-ray rheography. This underscores the importance of X-ray orientation in capturing unique flow characteristics. To address the challenge posed by antisymmetric granular flows, we suggest using an alternative scanning alignment approach that enhances the internal velocity reconstruction. Specifically, it is shown that by aligning the X-rays 45° to the flow's antisymmetry directions, X-ray rheography can be used with greater precision to investigate flow behaviour in scenarios involving antisymmetrical flows, such as the granular mixing cases studied throughout this thesis.

## 3.1 Overview

For steady-state granular flow, X-ray rheography (Baker et al. 2018) technique uses radiographs from two orthogonal angles to reconstruct velocities perpendicular to both X-ray planes, allowing the full 3D velocity field to be determined with only three orthogonal X-ray radiographs. The reconstruction process involves analysing multiple sets of X-ray images to calculate the probability density function (PDF) of the displacements (see Figure 2.8). This is achieved through image correlation and deconvolution analysis (Baker and Einav 2021). The PDF is discretised into velocity vectors, and the resulting vector is paired with the corresponding vector

in a perpendicular direction (Baker et al. 2018). The precision of this rheography method has been thoroughly investigated (Baker and Einav 2021, Baker et al. 2018), resulting in a series of guidelines on the size of the interrogation window, the number of interrogation windows, and the number of iterations in the matching process for reliable measurements of granular flow.

In two-bladed granular mixing, the velocity vectors exhibit an antisymmetric pattern along the axis of a blade, as shown in the two-blade mixer (see Figure 3.1). When the X-ray source and detector are aligned with this axis, the radiographs capture overlapping flow regions that have opposite displacements. This overlap makes it difficult to discern precise details of the internal velocity. This Chapter discusses how anti-symmetric flows can be studied by adjusting the X-ray projection orientation to avoid the effects of antisymmetry.

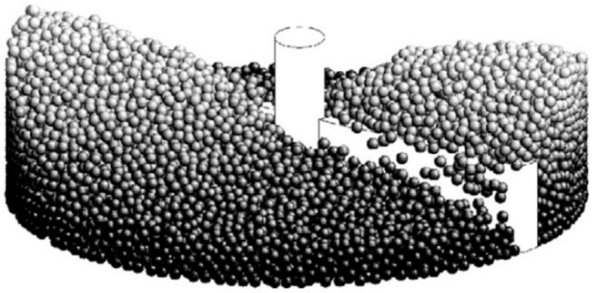

FIGURE 3.1: Anti-symmetric flow while mixing of granular material using a two-bladed mixer (Bai et al. 2017).

We investigated the PDFs of vertical displacements from synthetic radiographs of artificially antisymmetric vertical flows. When projections align with this axis, radiographs yield similar flow statistics, which lack sufficient contrast for precise internal velocity reconstruction. By rotating the projection 45 degrees, antisymmetry is disrupted, enhancing contrast and greatly improving velocity field recovery, highlighting the critical role of projection alignment in capturing the dynamics of antisymmetric granular flow.

## 3.2 Methods

We simulate artificially constructed antisymmetrical vertical flow to assess how the X-ray orientation affects the recovery of the velocity fields of antisymmetric granular flows.

### 3.2.1 Simulation set-up

We model a hypothetical vertically directed antisymmetric granular flow within a cylindrical container with a height H = 100 mm and a radius R = 50 mm. Figure 3.2 shows the exact velocity distribution in the cylinder cross-section.

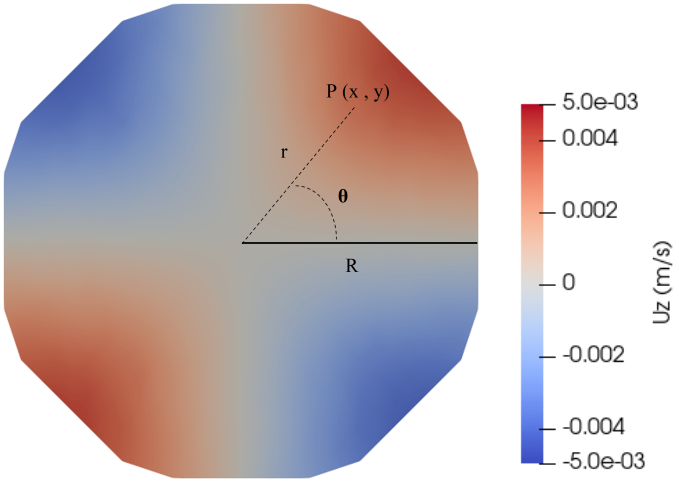


FIGURE 3.2: An analytic representation of the artificially imposed vertical velocity distribution within a cylinder's cross-section containing spherical particles, demonstrating controlled antisymmetric granular flow in the vertical direction. Red areas indicate upward motion, whereas blue ones indicate downward displacement.

The cylinder contains 5000 monodispersed particles, each 4 mm in diameter, inserted using a Monte Carlo approach. The velocity profile $U_z(x, y)$ of each particle grows linearly along the radius and radially as

$$U_z(r, \theta) = U_z^{max} \left(\frac{r}{R}\right) \sin(2\theta), \tag{3.1}$$

where $r = \sqrt{x^2 + y^2}$ represents the distance from the centre to the point $P(x, y)$, $R$ is the radius of the cylinder, and $U_z^{max}$ is the maximum amplitude of the velocity. The angular component $\sin(2\theta)$ exhibits an antisymmetric profile, reaching a peak at the intercardinal angles and reaching a zero at the cardinal angles. Consequently, the resulting analytically assumed velocity profile can be rewritten as

$$U_z(x, y) = U_z^{max} \left(\frac{\sqrt{x^2 + y^2}}{R}\right) \sin\left(2 \tan^{-1}\left(\frac{y}{x}\right)\right), \tag{3.2}$$

where $\theta = \tan^{-1}\left(\frac{y}{x}\right)$ represents the angle between the positive x-axis and the line connecting the origin to the point $(x, y)$.

The particles are displaced at each time step to establish a continuous vertical antisymmetric flow within the cylinder. Periodic boundary conditions are applied to reintroduce particles that exit the system. The discrete positions of particles in continuous flow are recorded at regular time intervals, which are used in creating virtual X-ray radiographs in this study.

### 3.2.2 Radiographic acquisition

Capturing pairs of radiographs from two orthogonal directions is crucial to evaluate the internal velocities perpendicular to the plane formed by the X-ray pair. In the example illustrated in Figure 3.3, the granular material flows vertically along the Z-axis within the cylinder.

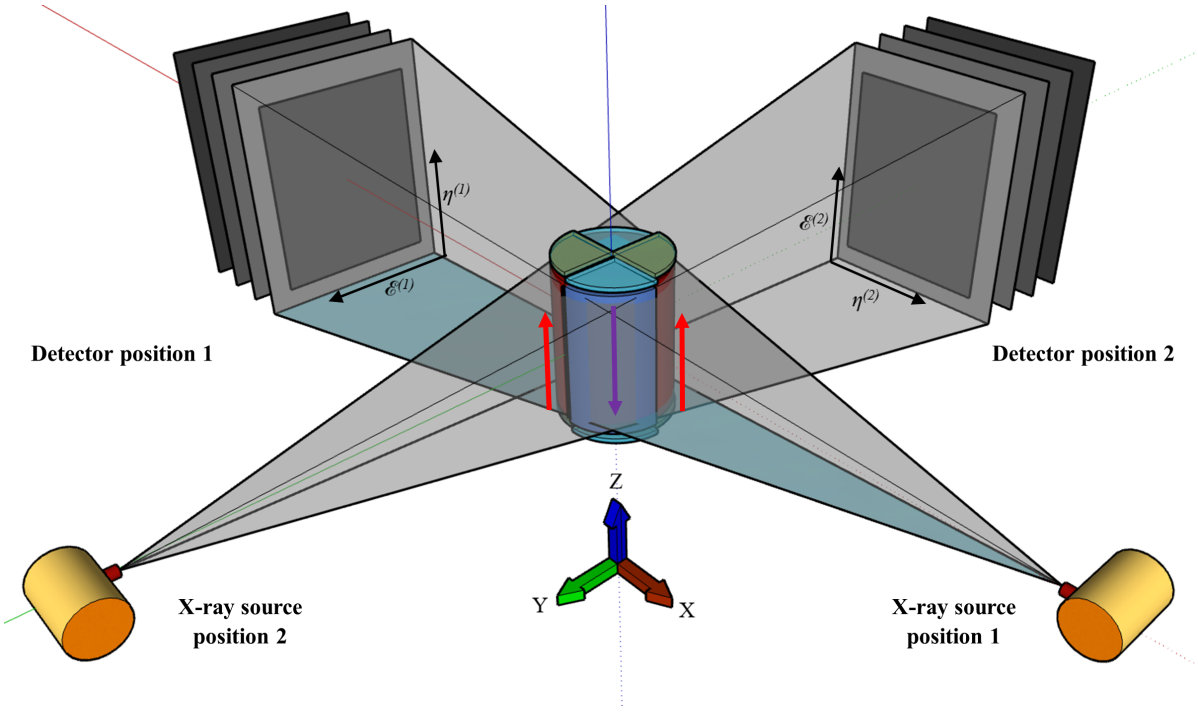


FIGURE 3.3: The diagram depicts a virtual X-ray setup with granular material in a cylinder filled with spherical particles. The particles in opposite quadrants move upwards (indicated in red) and downwards (in blue). Yellow cylinders indicate the positions of the X-ray sources, while the grayscale images display radiographic data at the corresponding detectors. Also shown are the global $(X, Y, Z)$ and local imaging coordinates $(\xi, \eta)$. Two X-ray orientation are aligned along the line of antisymmetry

In each setup, a virtual X-ray source projects parallel rays through the material, and a virtual detector creates X-ray radiographs. Although variations in material attenuation coefficients, sample depth, and packing density significantly affect radiograph intensity (Gallas et al. 2004, Jackson and Hawkes 1981), our main goal is to produce conceptual radiographs sufficient to recover flow properties.

If $\rho(x, y, z)$ represents the density distribution at a particular spatial position and time, the material depth $D(x, z)$ along the $Y$-axis projection is defined as

$$D(x, z) = \int_{y_{\text{min}}}^{y_{\text{max}}} \rho(x, y, z) dy, \tag{3.3}$$

where $y_{\text{min}}$ and $y_{\text{max}}$ denote the boundaries of the material domain. The radiograph intensity $I(x, z)$ obtained from the Beer-Lambert attenuation law (Kerur et al. 1991) is given by

$$I(x, z) = I_0 \exp\left( - \int_{y_{\text{min}}}^{y_{\text{max}}} \mu(x, y, z) dy \right), \tag{3.4}$$

where $\mu$ represents the spatially varying linear attenuation coefficient and $I_0$ represents the initial intensity of the artificial X-ray source. We assumed uniform density across all materials, and the void spaces had negligible attenuation coefficients compared to the solid regions. Hence, we define a constant spatial mass coefficient $\mu_m = \mu/\rho$. Using this mass coefficient, Equation 3.4 can be simplified to

$$I(x, z) = I_0 \exp\left( -\mu_m \int_{y_{\text{min}}}^{y_{\text{max}}} \rho(x, y, z) dy \right). \tag{3.5}$$

Solving Equations 3.3 and 3.5, we obtain the intensity of the artificial radiograph as

$$I(x, z) = I_0 \exp\left( -\mu_m D(x, z) \right). \tag{3.6}$$

We use Equation 3.6 using an attenuation coefficient of $\mu_m = 0.015$ pixels$^{-1}$ and an initial intensity $I_0 = 1$. In a simple case involving one monodisperse particle (see Figure 3.4), the final intensity of the radiograph depends on the particle's attenuation coefficient and the depth of X-ray penetration along that particle.

This concept can be extended to include all particles within the depth of the material. We generate artificial radiographic images along the $XZ$ planes (see Figure 3.5 a) and $YZ$. This

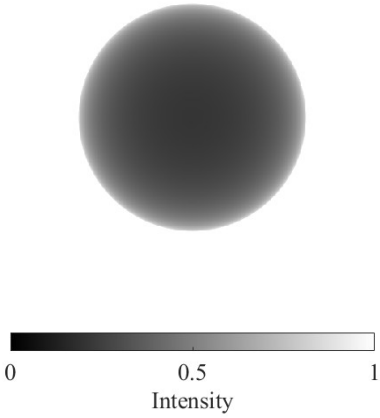


FIGURE 3.4: Theoretical radiograph of a sphere

process involves generating a series of projections that are intended to capture the motion of the particles over time.

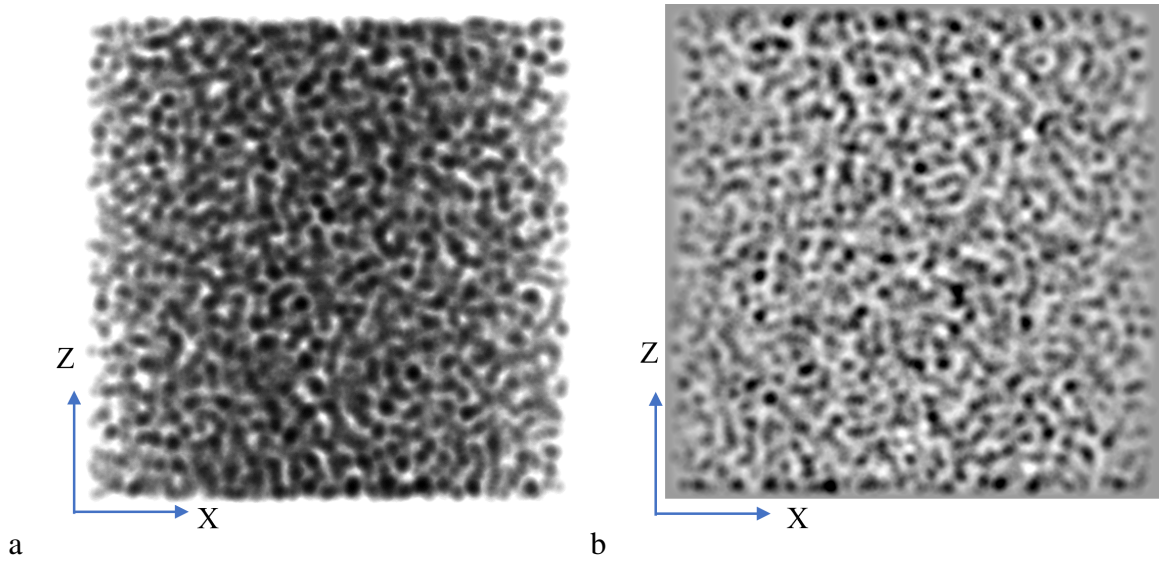


FIGURE 3.5: Projected theoretical X-rays: a) Intensity ; b) Logarithm of the normalised intensity

At each time step, the movement of particles causes a change in the projected attenuation, which affects the intensity. Therefore, we normalise the images by dividing the 1000 radiographs obtained by their mean intensity throughout the flow process. Upon examining Equation 3.6, we observe that the intensity is an exponential function of the depth of the material. This implies that taking the logarithm of normalised intensity ($\hat{I}$) results in an equation that is a simple linear transformation of depth (Baker and Einav 2021). Thus, for the next step, we use

the logarithm of the normalised intensity (see Figure 3.5 b) as

$$L(x,z) = \log(\hat{I}(x,z)) = \log(I_0) - \mu_m D(x,z). \tag{3.7}$$

### 3.2.3 Extracting kinematics from radiographs

We use the deep velocimetry method (Baker and Einav 2021) to find the velocities along the $Z$ direction in each internal grid. With this theory, the 2D projected images provide valuable insight into the out-of-plane velocity distribution. This method quantifies the position variances between images taken at specific time intervals through image correlation analysis to determine the PDF of the displacements.

We begin by dividing the normalised radiographs into 21x21 windows. Given that each radiograph spans 1500x1500 pixels$^2$, this division results in grids of approximately 70x70 pixels$^2$ (see Figure 3.6 a). To achieve a better balance between the number and size of grid cells for efficiency and improved resolution, we refer to the work of Baker et al. 2018, which cautions that overly large windows may compromise accuracy. In contrast, excessively small windows lack the spatial resolution to track particle velocities. Here, a larger grid size of 180x180 pixels$^2$ is later shown to be more optimal, with approximately nine particles per cell, ensuring a balance between spatial resolution and statistical accuracy during reconstruction. Although selecting a larger window here causes adjacent grids to overlap (see Figure 3.6 b), this will help to improve the accuracy at each query point.

For each successive pair of pre-processed images represented as $L_1$ and $L_2$ respectively, the 1D auto-correlation $(A)$ and cross-correlation $(C)$ functions within each interrogation window are computed as

$$A(m) = \sum_p \frac{\left(L_1(m+p) - \bar{L}_1\right)\left(L_1(p) - \bar{L}_1\right)}{\sigma_1^2}, \tag{3.8}$$

$$C(m) = \sum_p \frac{\left(L_1(m+p) - \bar{L}_1\right)\left(L_2(p) - \bar{L}_2\right)}{\sigma_1 \sigma_2}, \tag{3.9}$$

where $m$ represents discrete pixel displacement, and $p$ denotes pixel position, while $\bar{L}_1$, $\bar{L}_2$, $\sigma_1$, and $\sigma_2$ denote the mean and standard deviation of the log of the intensities taken over each window. Understanding how the measured correlation functions relate to the actual displacements of the material is necessary. This is given by convolution equation (Dubsky et al.

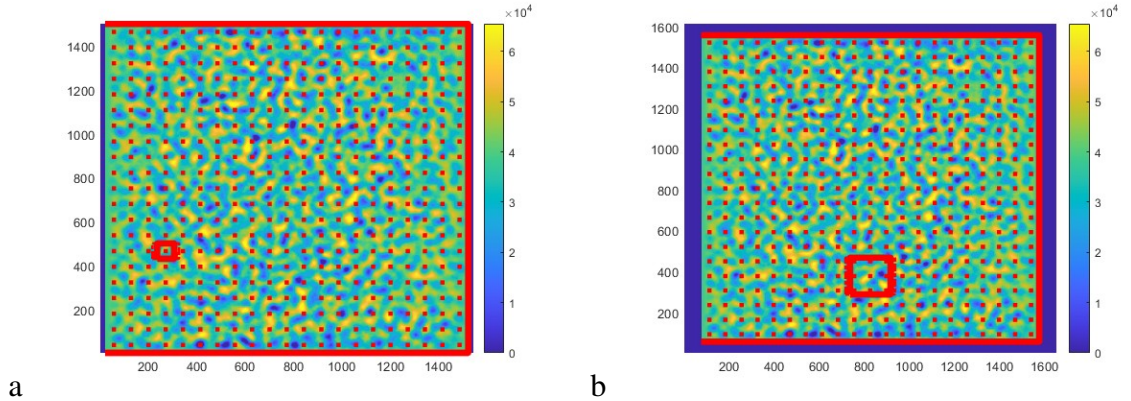


FIGURE 3.6: Architecture of the interrogation window illustrating image size (as indicated by the axes) and discretisation cell size: (a) A 70 × 70 pixel$^2$ window with limited spatial resolution; (b) A 180 × 180 pixel$^2$ window used in this study. The colour represents radiograph density.

2010) as

$$C = A * f, \tag{3.10}$$

where $f$ represents the PDFs of displacements within the window. The discrete convolution operator, denoted by $*$, is defined as

$$C(m) = \sum_i A(m-i)f(i). \tag{3.11}$$

Since C and A are measurable, the PDFs $f$ of displacements within each window can be determined using the equation 3.10. If the relationship is precise, this can be easily achieved through a basic division in the Fourier domain. However, after correlation averaging, some noise remains and gets amplified during Fourier division, indicating mathematical ill-posedness. We use a Tikhonov-type scheme (Baker et al. 2018) by choosing $f$ to minimise a non-linear function as

$$T(f) = \sum_m \left(C(m) - (A * f)(m)\right)^2 + \alpha \sum_m \left(f(m) - f(m+1)\right)^p, \tag{3.12}$$

where the PDF constraints are $f \geq 0$ and $\int f = 1$ in the discrete space. The regularisation parameters are $\alpha$ = 0.01 and $p$ = 2. Equation 3.12 is solved using the Matlab fmincon function. This process involves using 20 sets of average auto- and cross-correlation functions in each window, taken from different moments in time to reduce noise. The final function, $f$, is obtained

by averaging these deconvolutions (Baker et al. 2018). For interrogation windows $N^2$ in one scanning direction, each linked with two distributions of velocity components in the plane, the result is two $N \times N$ arrays of PDFs per scanning direction.

Our global coordinate system uses three perpendicular directions $(X, Y, Z)$ as shown in Figure 3.3. For simplicity, local imaging coordinates $(\xi, \eta)$ are used to refer to the two in-plane directions in each image, which are related to the global axes as

$$\begin{aligned} (\xi^{(1)}, \eta^{(1)}) &\rightarrow (Y, Z) \\ (\xi^{(2)}, \eta^{(2)}) &\rightarrow (Z, X). \end{aligned} \tag{3.13}$$

In the local imaging coordinates, $\eta^{(1)}$ and $\xi^{(2)}$ now correspond to the $Z$ directions. When scanning in a single direction, $N^2$ interrogation windows are associated with a distribution of vertical velocity components in the plane. The analysis involves determining $2N^2$ PDFs for vertical displacement from two scanning directions, providing information about the $\eta^{(1)}$ and $\xi^{(2)}$ directions. Each of these $2N^2$ PDFs represents the depth of the material and needs to be further divided into specific internal grids. Thus, the PDF $f$ obtained from image correlation and convolution analysis is then discretised into $N$ equally spaced percentiles $U_1$, $U_2$, ... $U_N$, where each displacement $U_i$ satisfies

$$\int_{U_{\text{min}}}^{U_i} f(U)\,\mathrm{d}U = \frac{i}{N+1}, \tag{3.14}$$

where $i = 1, 2...N$, and $U_{\text{min}}$ represents the minimum displacement, set as minus one-half of the interrogation window size (Baker et al. 2018). This method generates 3D candidate arrays of size $N^3$ for each scanning orientation. For each window, $N$ data are collected on in-plane displacement perpendicular to the beam's direction. However, these data do not specify the relative position of each component in the out-of-plane. An orthogonal scanning angle helps to obtain missing out-of-plane information, providing insight into the exact position and velocity component. Thus, the discretisation process yields $2N^3$ data points for one velocity component to reconstruct the $N^3$ unknowns.

The next step is to calculate the velocity vector $U_{ij}$ in a specific vertical position $z$ for each internal position $(x, y)$, identifying the correct pair and their respective locations. We have two matrices $U^{(1)}_{i,k}$ and $U^{(2)}_{j,l}$ obtained from the discretisation of PDFs along the $\eta^{(1)}$ and $\xi^{(2)}$

directions. Here, $i$ and $j$ represent the positions along $x$ and $y$, and $k$ and $l$ are the discretisation indices. The challenge is to choose the indices $k(i,j)$ and $l(i,j)$ for each unique vector to be placed in each row and column $U^{(1)}_{i,k}$ and $U^{(2)}_{j,l}$. This challenge can be overcome by solving a process similar to a Sudoku-style puzzle (Baker et al. 2018). However, unlike Sudoku, the two observations may not align perfectly. Therefore, our objective is to minimise the overall matching error, which can be denoted as

$$E = \sum_{i,j} \varepsilon_{ij}, \tag{3.15}$$

where

$$\varepsilon_{ij} = |U^{(2)}_{ik} - U^{(1)}_{jl}|. \tag{3.16}$$

The matching error at the internal position $(i,j)$ in the $(X,Y)$ plane is a key consideration. Direct optimisation of this process is computationally intensive, with a complexity of $O(N!^{2N})$. Instead, we use a more efficient approach (Baker et al. 2018) with a complexity of $O(N^4)$. We begin by selecting an arbitrary internal cell $(i,j)$ and identifying two sets of candidate velocities. Next, we choose the closest matching pair to minimise $\varepsilon_{ij}$. This process is similar to solving a Sudoku puzzle and helps to narrow down the potential velocities. The velocity in each cell $(i,j)$ is then determined as the average of the candidate vectors chosen as:

$$U_{ij} = \frac{1}{2}(U^{(2)}_{ik} + U^{(1)}_{jl}). \tag{3.17}$$

Subsequent cells are handled similarly. The procedure's outcome may vary depending on the order of cell computation, which can result in different solutions and matching errors. We evaluated 5,000 random paths and averaged the 50 lowest matching error values to find the final solution. This helps to address the nonuniqueness concerns (Baker et al. 2018). The same method is used to reconstruct the vertical velocity component at other vertical positions.

## 3.3 Results

In our study of anti-symmetrical flows, we investigated how the orientation of X-ray detection affects the analysis of captured flow patterns. We positioned the X-ray detection system at

angles of 0° and 45° (see Figure 3.7). At 0°, aligning X-rays along the antisymmetry line typically produces nearly uniform PDFs (see Figure 3.8).

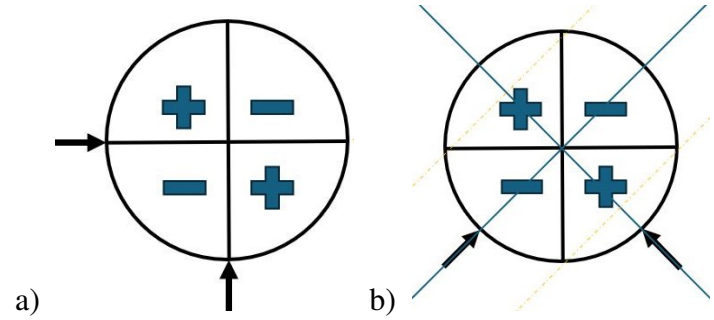


FIGURE 3.7: Projection angle made with the line of antisymmetry: a) 0° having equally likely configurations when viewed perpendicularly, where the axis of antisymmetry separates the quadrants; b) 45° with Configuration unlikely to catch similar flow characteristics. The "+" quadrants indicate upward granular material flow, while "" denotes downward flow, with directional arrows representing the X-ray projection.

The PDF obtained from the deconvolution at d = 0.75R is compared to the PDF calculated from the exact velocity field in Equation 3.2 at the same locations (see Figure 3.8 b). Both PDFs exhibit a similar likelihood of opposite movements in the exact (green crosses) and reconstructed (blue circles) results. This observation is further supported by analysing the mean displacement in the PDFs across additional windows, indicating a near-homogeneity of vertical displacements (see Figure 3.8 c).

However, significant differences in standard deviation are observed between the exact and reconstructed distributions. Despite these variations in standard deviation, the deep velocimetry of the artificial radiographic images effectively captures the mean and displacement range associated with non-zero probabilities. In the setup illustrated in Figure 3.3, it is noted that some transverse detail is lost. Consequently, when these PDFs are discretised, they yield multiple similar displacement vectors, complicating the selection of unique velocities. This situation increases the likelihood of mismatched pairings, which can lead to significantly different outcomes compared to the precise solution.

Moreover, this underscores the importance of transverse details affected by X-ray orientation for the accurate analysis of antisymmetric granular flows. If bypassing the antisymmetry line could benefit the rheography, the study requires the identification of the appropriate angle that

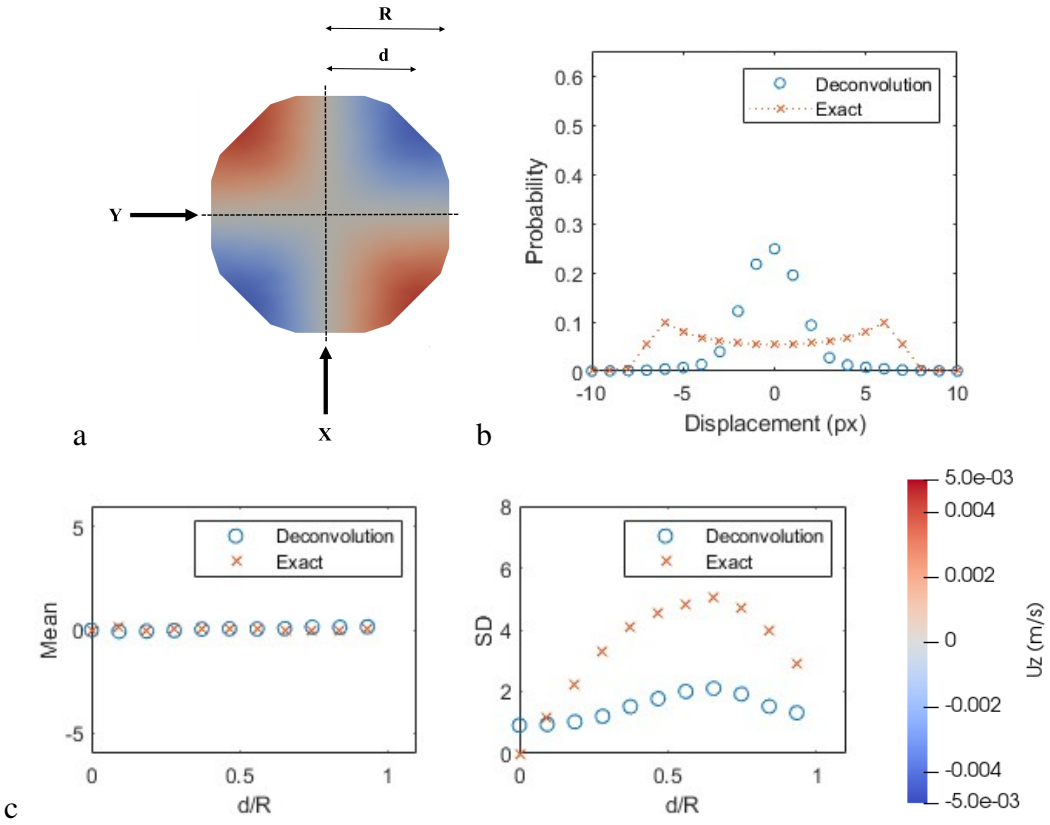


FIGURE 3.8: Deconvolution results in the case of X-ray orientation aligned along the line of anti-symmetry in vertically anti-symmetric granular flow: a) Representation of exact velocity contour profile in the cylinder cross-section filled with spherical particles, showing upward motion in red and downward displacement in blue; R is the radius of the cylinder and d is the distance of the interrogation windows locations from the centre. b) Comparison between exact and deconvolution PDFs at interrogation windows located d=0.75R c) Comparison between the mean and standard deviation of exact and deconvolution PDFs for multiple interrogation windows and the distance to the centre of the window position is normalised by radius; Only half of the section is shown in the result as the result on the other half is symmetrical.

enhances spatial separation. In such a case, any shift in the projection angle away from the antisymmetry line that could yield an optimal solution is preferred. Therefore, an optimal configuration of the virtual X-ray is introduced, as shown in Figure 3.9, where the X-ray orientation pairs are misaligned at 45° with respect to the line of antisymmetry.

When the X-ray orientations are misaligned and bypass the line of antisymmetry, the flow characteristics can be described as follows. At the position where $d = 0.75R$, both deconvolution and exact PDF predict downward displacements (see Figure 3.10 b). Analysing

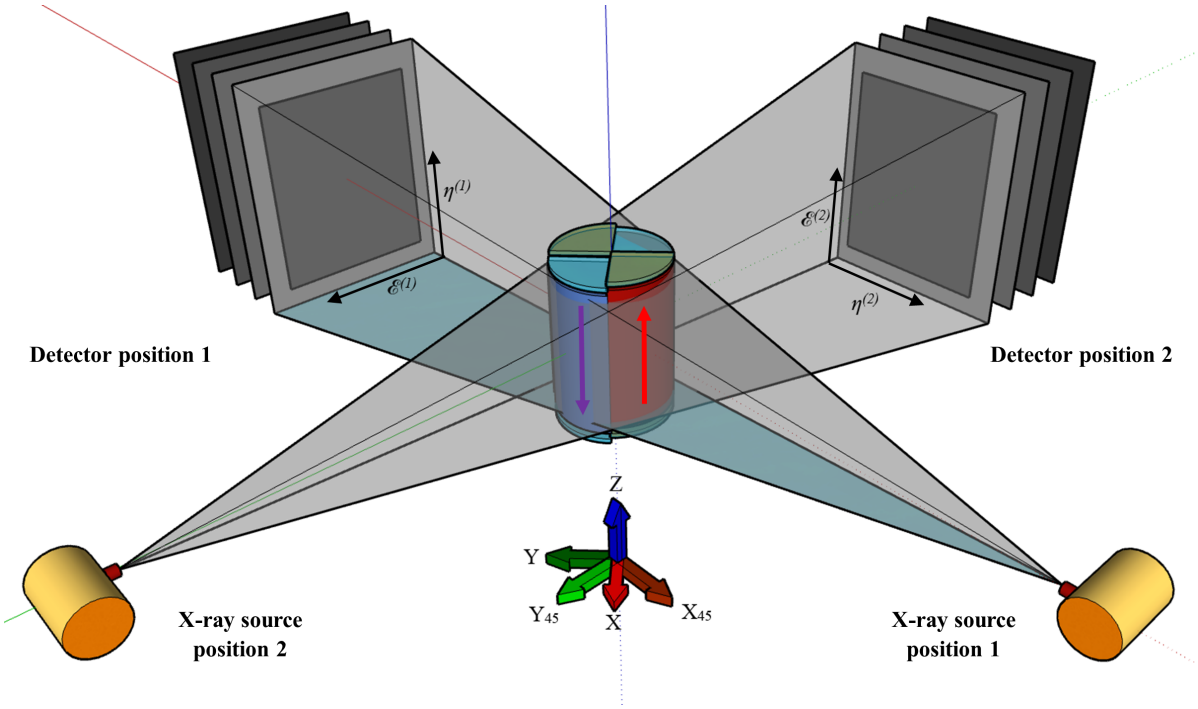


FIGURE 3.9: Configuration where two X-ray orientation are misaligned along the line of antisymmetry

the mean displacement at additional locations (see Figure 3.10 c), both the exact and the reconstructed PDFs indicate that the non-homogeneous PDFs of vertical displacements are better represented in this orientation. Furthermore, significant variations in the standard deviation decrease in this case, unlike in the previous situation, due to the similar motion observed within the window.

## 3.4 Discussion

The internal velocity reconstruction process using the rheography technique involves two stages. The first is the deconvolution stage, which extracts the PDF of displacement utilising deep velocimetry. The second step is achieving the accurate placement of internal velocity by arranging the discretised velocity vectors obtained from the deconvolution steps. The deconvolution results are post-processed for internal velocity reconstruction, and the results are studied for both cases: one from X-ray orientations aligned with the antisymmetry line and the other diverging from it to break the effects of the antisymmetry (see Figure 3.11).

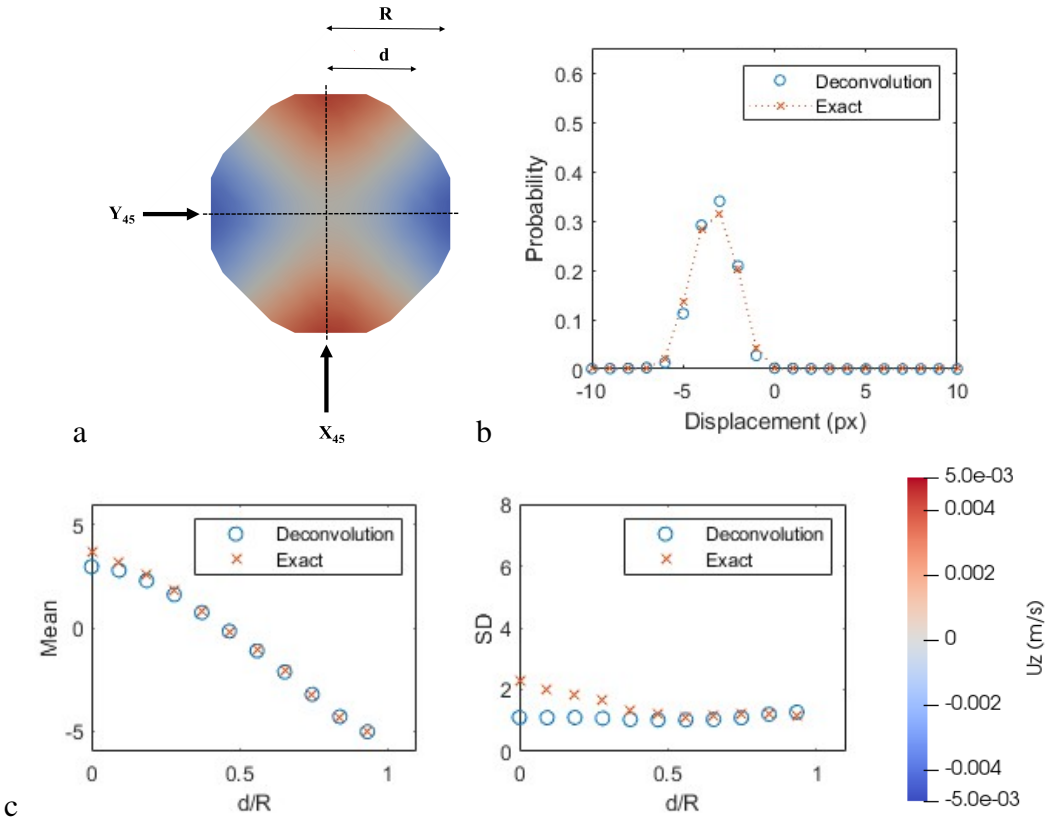


FIGURE 3.10: Deconvolution results in the case of X-ray orientation misaligned (rotated by $45°$) along the line of anti-symmetry in vertically anti-symmetric granular flow.

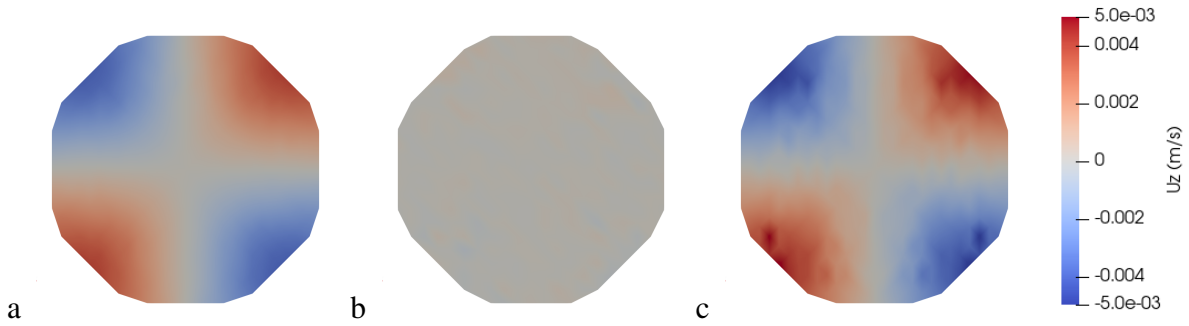


FIGURE 3.11: Vertical velocity ($U_z$) contours in vertically antisymmetrical granular flow at the cross-section of a cylinder, with red indicating upward flow and blue indicating downward flow: a) exact solution, b) reconstructed solution along X-ray orientation aligned along the line of antisymmetry, c) reconstructed solution along X-ray orientation misaligned to bypass the line of antisymmetry.

Since, orienting the X-rays to avoid the antisymmetry line generates nonuniform PDFs, this approach results in distinct displacement vectors upon discretisation with which, we can achieve more accurate results by selecting velocities from this varied set of candidate vectors (see Figure 3.11 c), which reaffirms our hypothesis about the critical role of X-ray orientation in deep velocimetry and rheography techniques.

Since this method is based on image analysis and optimisation, and it could introduce errors at various stages of the reconstruction process, such as errors in the correlation, discretisation, and matching process, we will deal with each stage individually. Evaluating errors involves mainly deconvolution and matching process errors. To determine their relative impacts, we begin with deconvolution PDFs and then reconstruct the velocity. Figures 3.12 a and 3.12 b show combined errors from two orthogonal X-ray orientations: one on the antisymmetry line and the other when bypassing the antisymmetry line. Interestingly, we can see the antisymmetry line when bypassing, and although misalignment reduces error, some inaccuracies in the matching process persist. The exact PDF from Equation 3.2 helps assess matching and antisymmetry bypass errors when reconstructing the velocity field. The error in Figure 3.12 c arises solely from the matching using exact PDFs. There are minor differences between deconvolution errors and exact PDFs. Thus, bypassing antisymmetry significantly improves the solutions, confirming that this concept can be used to study antisymmetrical granular flow using a rheography technique.

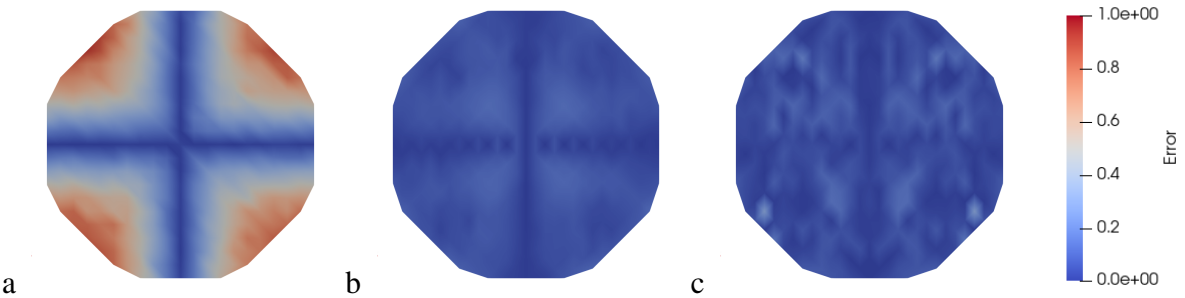


FIGURE 3.12: Absolute error contours for reconstructed velocity at a cylindrical cross-section obtained utilising (a) reconstructed PDFs along the X-ray orientation aligned with the antisymmetry line, (b) reconstructed PDFs along an X-ray orientation misaligned to bypass the antisymmetry line, and (c) exact PDFs. Errors in (a) and (b) include both deconvolution and matching errors, while (c) accounts only for matching errors, as it uses exact PDFs.

## 3.5 Summary

This chapter explores the application of X-ray rheography to investigate granular flow dynamics in antisymmetrical scenarios. The chapter motivates us to consider the scanning alignment approach to enhance the reconstruction of internal velocities, especially by bypassing antisymmetry issues with X-ray orientation. The findings indicate that bypassing antisymmetry in the flow reduces significant errors in velocity reconstruction and enables a realistic investigation of antisymmetrical granular flow kinematics using the rheography technique. In the following chapter, the focus shifts to exploring mixing kinematics by implementing this subtle technical point to bypass the issues with antisymmetric flows in experimental research of mixing kinematics.

CHAPTER 4

# Mixing kinematics in spherical granular materials

---

Granular mixing plays a crucial role in various industrial processes; however, intricate interactions between particles present significant theoretical difficulties in understanding flow behaviour. This chapter develops an experimental apparatus and a framework to enhance our understanding of granular mixing dynamics through X-ray rheography. We constructed a dynamic mixer for our study that helps us to effectively capture flow patterns on radiographs. Our focus has been on overcoming technical challenges, such as obtaining clear radiographs from three orthogonal angles despite interference from a motorised central impeller blade and the use of well-aligned X-ray orientation to bypass the issue of antisymmetry for better execution of the rheography techniques, as described in Chapter 3. These considerations have facilitated a detailed investigation into the internal mixing dynamics and an assessment of the effectiveness of X-ray radiography in studying granular mixing. We align our experimental results with predictions generated by the additional development of a discrete element method (DEM) model that aims to simulate similar granular mixing conditions. The framework established here provides a basis for analysing flow behaviour across various particle sizes and shapes for further research discussed in Chapter 5 of this thesis.

## 4.1 Overview

Understanding the mixing kinematics of granular materials is essential for various industries, such as construction, pharmaceutical production, and the preparation of culinary ingredients (Bridgwater 2003, Shinbrot et al. 2006, Muzzio et al. 2003, Havlica et al. 2015). These industries often use cylindrical mixers with impeller blades for particle mixing (Litster et al. 2002, Mateo-Ortiz and Méndez 2015). However, tracking the movement of individual particles within these mixers presents significant challenges due to obstructions from other particles,

the container, and the impeller blades. Thus, much of the experimental research has utilised conventional camera images and corresponding particle image velocimetry (PIV), which mainly examine the surface and boundaries of the setup, often through transparent walls (Conway et al. 2005, Lekhal et al. 2006). Although camera image analysis can provide insight into particle movements at the surface, it cannot capture the internal dynamics due to the medium's opacity, especially away from the walls and within the bulk material. Studies show that granular materials often exhibit different behaviours near boundaries due to the formation of boundary layers (Rognon et al. 2015, Miller et al. 2013). This makes the experimental understanding of granular mixing more challenging than that of transparent fluids, given challenges such as the opacity of the grains and their interaction with fluids.

As discussed in the review of the literature (Chapter 2), several advanced techniques have been developed to study internal kinematics. Positron emission particle tracking (Windows-Yule et al. 2014) offers high precision in monitoring the motion of discrete particles in three dimensions, but requires radioactive tracers, limiting its practicality. Magnetic resonance imaging (Stannarius 2017, Penn et al. 2017) produces detailed images but has limited spatial resolution and requires expensive specialised equipment. Refractive index-matching scanning (Dijksman et al. 2012) enables high-resolution imaging of transparent samples, offering clear insights into particle dynamics. However, this technique requires the addition of viscous fluids, which can affect the overall kinematics. Each method offers distinct advantages and drawbacks that highlight the need to use complementary techniques to investigate granular mixing kinematics experimentally.

To study granular flow on opaque granular materials, X-ray computed tomography ( X-ray CT) (Kou et al. 2017, Hall et al. 2010, Saadatfar et al. 2012, Athanassiadis et al. 2014) is generally preferred to reconstruct detailed internal density fields without disturbing the sample (Taillandier-Thomas et al. 2016). However, studying dynamic granular problems using X-ray CT requires rotating the X-ray source or sample, leading to longer processing times and potentially less accurate results due to material movement. Recent technological advances in high-speed radiography have allowed continuous time-scale imaging of granular flows (Guillard et al. 2017). By combining high-speed radiography with X-ray rheography (Baker et al. 2018), it is now possible to reconstruct 3D internal velocities in granular materials using X-rays from

three orthogonal directions. This integration provides a novel alternative to examine the internal behaviour of granular mixing. However, analysing granular mixing is intricate and presents challenges regarding experimental design. For example, previous studies have shown that two-blade mixers generate antisymmetric flows (Bai et al. 2017). This characteristic necessitates precise X-ray orientation to capture non-homogeneous flow. To address this challenge, we orient the X-rays to avoid the antisymmetry line, allowing us to reveal the internal velocity fields, as discussed in Chapter 3. In addition, we rotated the cylindrical boundary instead of the blade to ensure a consistent radiograph geometry. This setup (see Figure 4.1), designed carefully, allows us to effectively capture velocity fields and explore the capabilities of X-ray rheography in granular mixing. This chapter then assesses the effectiveness of rheography in analysing mixing kinematics of spherical glass beads, by comparing velocity field data from X-ray rheography with DEM simulations under similar mixing conditions.

## 4.2 Design and construction of a granular mixer

Before designing the granular mixer, it is essential to consider several key factors to ensure the accurate capture of flow information through radiographic imaging. The mixer should be designed in such a way that X-ray rheography can be used, a technique used to reconstruct the 3D internal velocity field of granular flows through three orthogonal X-ray projections: a downward projection along the axial direction and two lateral projections, as illustrated in Figure 4.1. To achieve better imaging quality, the design must ensure complete visibility and accessibility of the flow region for the X-ray system, minimising obstructions by incorporating materials with low X-ray attenuation for critical structural components. Moreover, the mixer should enable controlled and reproducible flow conditions to capture dynamic behaviours in different operating scenarios consistently.

It is crucial to note that if the impeller blade is rotated during mixing, an axial X-ray projection leads to radiographs that show different geometries; specifically, the impeller blade geometry exhibits an angular shift in each consecutive radiograph. Therefore, the experimental setup should be designed so that each radiograph displays a consistent geometry. To achieve this, an approach was used in which the cylindrical boundary was rotated using an external motor while the blade remained stationary. To implement this solution, various mechanical

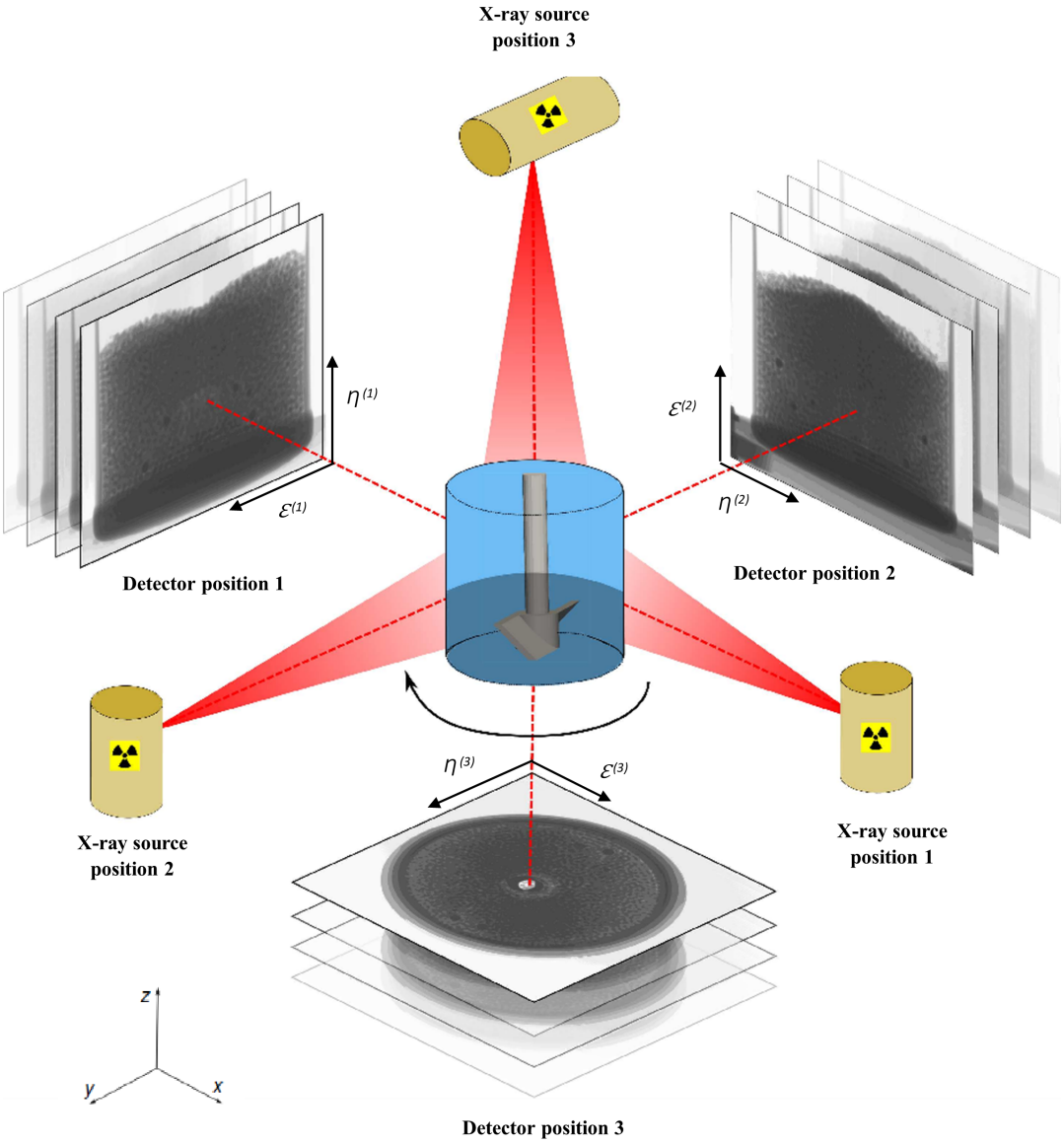


FIGURE 4.1: Schematic of the experimental setup: Granular material is confined within the blue cylinder, which rotates while the blade remains stationary, ensuring consistent blade geometry in successive radiographs. Yellow cylinders indicate the three X-ray source positions, while red outlines represent the beam extent. Grayscale images show radiographic projections at the corresponding detectors. Global coordinates (x, y, z) and local imaging coordinates $(\xi, \eta)$ are provided for reference.

components, including a hollow turntable (see Figure 4.2) and gear mechanisms, were used. The hollow central region of the turntable allows X-rays to pass through the mixer and reach the detector beneath it without interference. This turntable is connected to the gear set (see Figure

4.3), allowing the rotation of the pinion of the gear linked to the external motor to drive the ring and the turntable synchronously. This setup ensured that consecutive radiographs captured consistent geometries, reflecting similar flow characteristics during steady-state mixing.

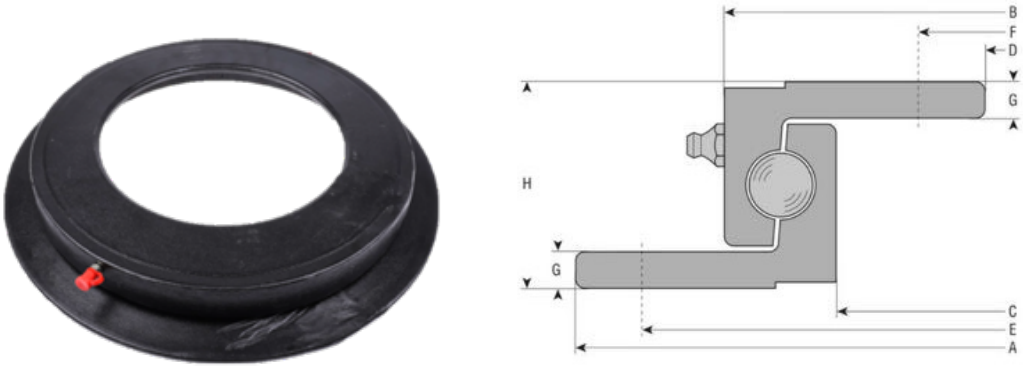


| A | B | C | D | E | F | G | H |
|---|---|---|---|---|---|---|---|
| 500 mm | 442 mm | 392 mm | 330 mm | 475 mm | 360 mm | 8 mm | 45 mm |

FIGURE 4.2: Detailed view of the turntable with a hollow centre, used to support the rotation of the cylindrical boundary of the mixer while allowing unobstructed X-ray passage in the axial direction for consistent radiograph geometry (dimensions provided in the table).

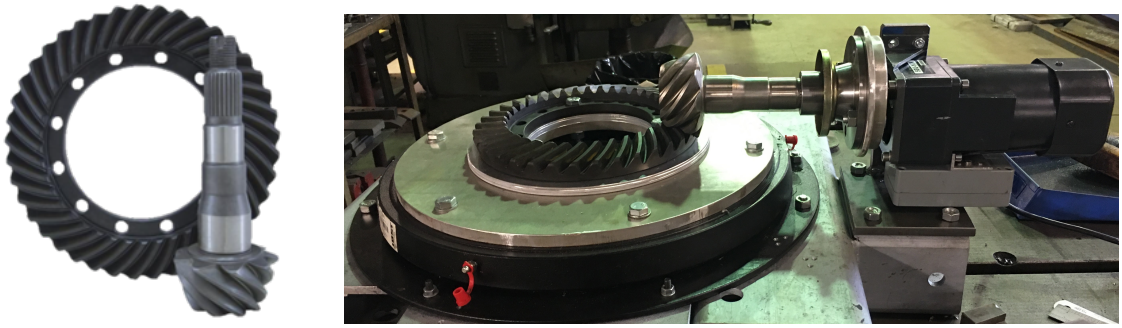

FIGURE 4.3: Configuration of the ring and pinion gear set, integrated with the motor.

After considering the axial direction, the focus now shifts to ensuring an unobstructed lateral view. A hollow cylinder (Figure 4.4 a) was designed and attached to the gear ring to achieve this, positioning the mixer above the motor and safety casings (Figure 4.4 b). The upper frame was installed with the design ensuring unobstructed radiographs from all three directions. Using a plastic bolt and nut, the blade was securely mounted on a 380 mm aluminium rod (10

mm diameter). Two layers of polycarbonate were used to enhance blade stability. Materials (aluminium, plastic bolts and nuts, and polycarbonate sheets) with low attenuation coefficients were carefully selected to minimise interference along the X-ray path during assembly.

a  b 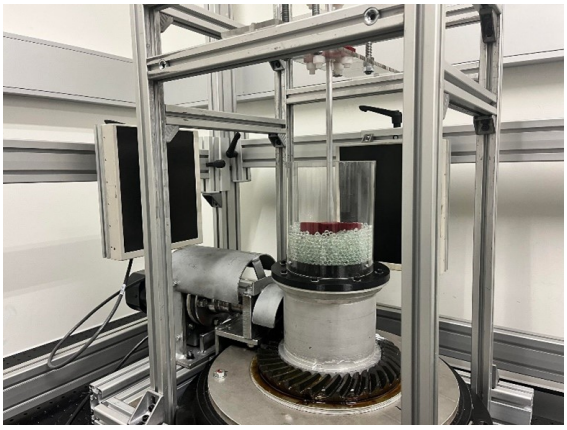

FIGURE 4.4: Granular mixing apparatus for experimental study of mixing kinematics using X-ray rheography: a) Cylinder elevated to a specific height to ensure an unobstructed horizontal X-ray path, with safety casings included; and b) Experimental setup with a blade attached to the aluminium frame.

## 4.3 Method

Table 4.1 presents the dimensions of the materials used in the initial experiments, all of which were approximately spherical. In each experiment, we used the same mass of material in a random loose package. We conducted the experiments using a vertical blade 10 cm long, 2 cm high and 3 mm wide, positioned 2 cm above the base of the cylinder, with a blade angle of $90^{\circ}$ (see Figure 4.5). The rotation period is 58.3 seconds in all experiments.

TABLE 4.1: Size of grains used in the experimental investigation.

| Material | Smallest Dimension (mm) | Largest Dimension (mm) |
|---|---|---|
| Glass beads (6 mm) | 5.94 | 5.94 |
| Glass beads (3 mm) | 2.81 | 2.83 |
| Glass beads (1 mm) | 1.00 | 1.10 |

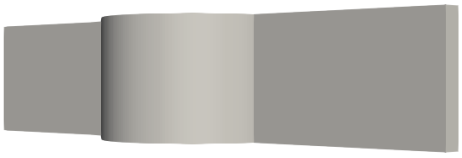

FIGURE 4.5: Blade configurations utilised in the study

### 4.3.1 X-ray imaging

To eliminate the issues associated with antisymmetric flow in a two-blade impeller, the X axis is orientated at a 45° angle clockwise to the blade axis, the Y axis is at a 45° angle counterclockwise to the blade axis, and the Z axis points vertically upward (see Figure 4.1). To minimise the conical effect of X-rays, we keep the source and detector as far apart as practical. Thus, the source-detector distance is 2 metres horizontally and 1.5 metres vertically. The source is set to emit radiation at 180 keV and 4 mA in horizontal directions and 170 keV and 3.5 mA in vertical direction. Radiographic images (see Figure 4.6) are recorded at 1920 × 1536 pixels (16-bit) at 10 frames per second.

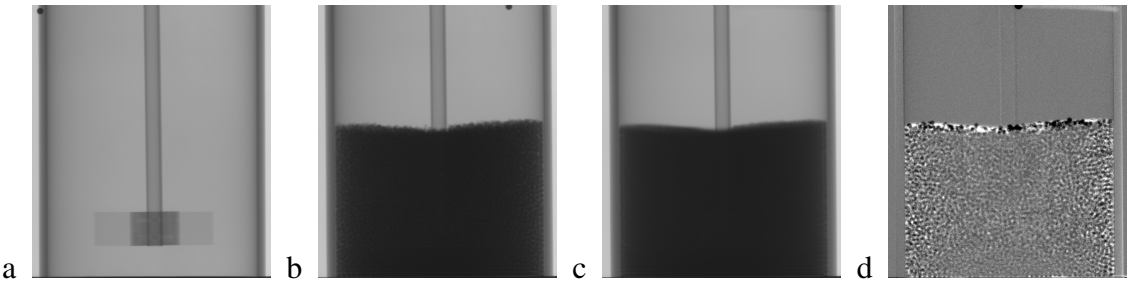


FIGURE 4.6: Experimental radiograph for 3 mm glass beads along normal to X-axis illustrating: a) Measured X-ray intensity $I_e$ of the empty container; b) Measured X-ray intensity $I_f$ of the container with 3 mm glass beads; c) Mean intensity avg$(I_f)$; and d) normalised intensity $\log\left(\frac{I_f}{\text{avg}(I_f)}\right)$ utilised for deconvolution.

The measured intensity $I$ on a given pixel at location $x$ of the detector is approximated by (Krinitzsky 1970)

$$I(x) = I_0 \exp\left(\int_l -\mu_m \rho_b(l) dl\right), \tag{4.1}$$

TABLE 4.2: Parameters considered for sensitivity analysis.

| Variable | Value |
|---|---|
| Young's modulus, $E$ | 5 Mpa |
| Poisson ratio, $\nu$ | 0.3 |
| Density, $\rho$ | 2500 kg/m$^3$ |
| Coefficient of restitution, $e$ | 0.25, 0.5, 0.75 |
| Coefficient of sliding friction, $\mu_s$ | 0.25, 0.5, 0.75 |
| Coefficient of rolling friction, $\mu_r$ | 0, 0.05, 0.1 |

where $I_0$ represents the initial intensity of the X-ray source, $l$ the X-ray path inside the medium, and $\rho_b$ the bulk density at each location in the material. The mass attenuation coefficient can be expressed as $\mu_m = \mu/\rho$ with $\mu$ as the constant attenuation coefficient and $\rho$ as the density of the material. The intensity obtained for the empty container $I_e$ and the container filled with granular material $I_f$ by this X-ray setup along the X-axis are shown in Figures 4.6 a and 4.6 b, respectively. During each time step, the movement of the particles causes a change in projected attenuation, affecting the intensity. Thus, we normalise the images by dividing them by the mean intensity avg$(I_f)$ of 1000 radiographs (see Figure 4.6 c) obtained from a consistent scanning direction during the flow process. This also helps to remove the effect of a rotating cylinder. In Chapter 3, we mentioned that the measured intensity is an exponential function of the material depth. Taking the logarithm of normalised intensity $\log\left(\frac{I_f}{\text{avg}(I_f)}\right)$ (see Figure 4.6 d) results in a simple linear transformation of depth. Therefore, for the next step, we will use the logarithm of the normalised intensity (see Figure 4.6 d) for the deconvolution.

### 4.3.2 Discrete element method

Replicating the entire experimental system is inherently complex because several factors must be considered, including surface roughness, variability in particle shape, and heterogeneity in particle distribution. In this conceptual study, we directly adopted the particle size distribution obtained from vernier calliper measurements. To improve computational efficiency, we employed a numerically softened Young's modulus. Taking advantage of the flexibility of the DEM, we conducted a sensitivity analysis on contact and boundary parameters. We varied the restitution coefficient ($e$), sliding friction coefficient ($\mu_s$), and rolling friction coefficient ($\mu_r$) across a range of plausible values (see Table 4.2). This approach allowed us to evaluate how changes in contact parameters influence the macroscopic behaviour of the system.

The DEM mixing model comprises a cylinder and a blade with the same geometric properties as the experiments, with the particles randomly introduced into the cylinder from an insertion plane placed above (see Figure 4.7 a). The particles then descend under the influence of gravity. Once the required volume of material has been introduced, the mixer is allowed to settle (see Figure 4.7 b) before the cylinder rotates for two revolutions, each lasting 58.3 seconds to mimic the exact conditions of the experiments. In the initial phase of the mixing process, a noticeable increase in the volume of the particles is observed relative to the initial volume packed (see Figure 4.7 c). This phenomenon occurs due to the reorganisation of the particles, which results in a decrease in packing density (Cleary 2000). Data collected from the final revolution are coarse-grained to determine the velocity field corresponding to a fully developed mixing state.

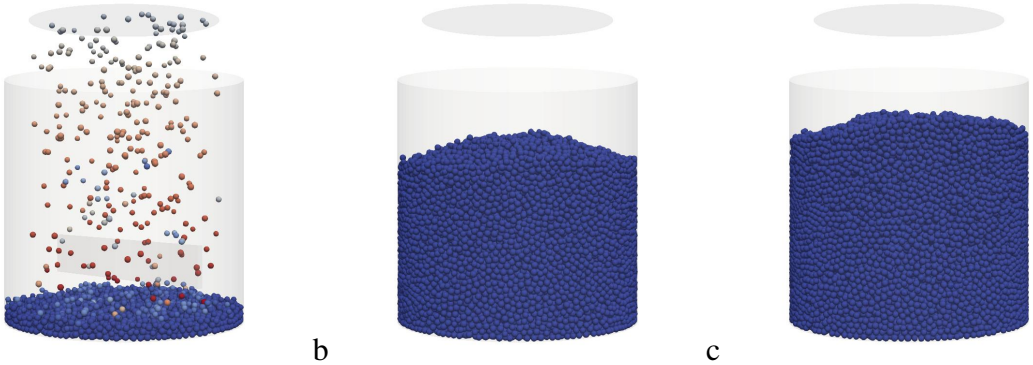


FIGURE 4.7: DEM mixer setup stages for 3 mm glass beads. a) Particle insertion, b) Particle settling, and c) Mixing phase.

Our sensitivity test of contact and boundary parameters in such a simulation setup showed that the sliding friction coefficient relatively impacts the metrics (Figure 4.8a) compared to the restitution and rolling friction coefficients (Figures 4.8b and 4.8c). We chose coefficients that qualitatively align well with the experimental outcomes for further comparison and simulations. It's also essential to remember that, regardless of the DEM model employed, these representations are just numerical methods.

The velocity field from such DEM simulations can be achieved through interpolation procedures such as coarse graining (Goldhirsch 2010; Weinhart et al. 2012). In this approach, the velocity, $v'(r)$ at any point $r$ is defined as a weighted average of the neighbouring grain

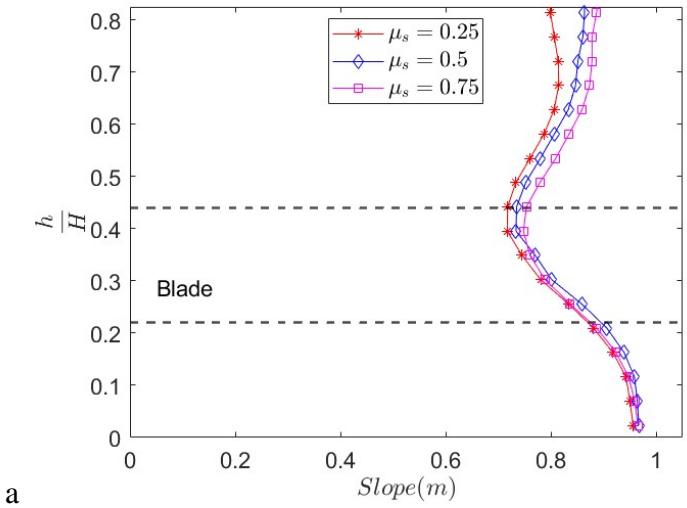


a

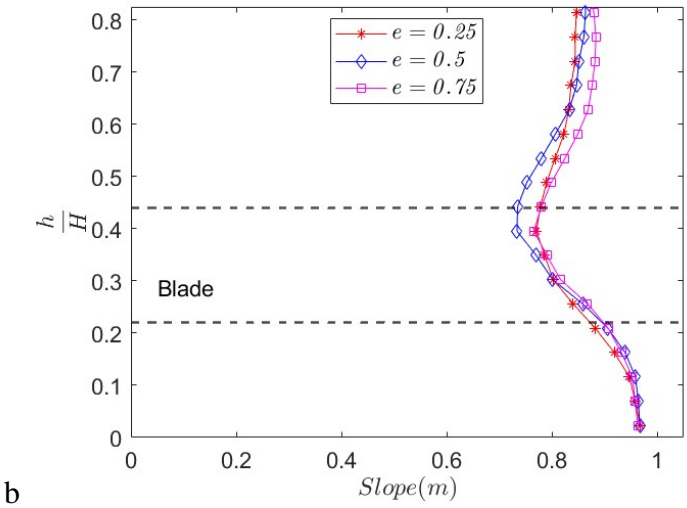


b

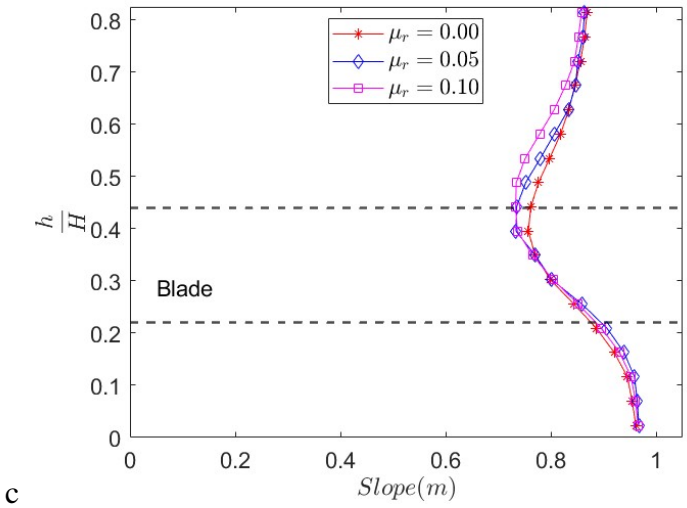


c

FIGURE 4.8: Variation of slope of the best-fit line for circumstantially averaged tangential velocity from coarse-grained DEM simulation, normalised by maximum RBM velocity along the cylindrical mixer radius to study: a) coefficient of sliding friction; b) coefficient of restitution; c) coefficient of rolling friction.

velocities as

$$v'(r) = \frac{\sum_i^N v_i' w(r - r_i)}{\sum_i^N w(r - r_i)}, \tag{4.2}$$

where $w$ is a weighting function with a unit volume integral, peaking at $|\mathbf{r}^*| = |\mathbf{r} - \mathbf{r}_i| = 0$ and decaying of $|\mathbf{r}^*| > 0$ with a typical decay distance $l$. The coarse graining is performed using the Lucy function with a typical length of $l = 2d$, where $d$ represents the diameter of the grains. For three-dimensional systems, the Lucy function (Lucy 1977) takes the following form (for $|\mathbf{r}^*| < l$ )

$$w(r) = \frac{105}{16\pi l^3}\left(-3(\frac{|r^*|}{l})^4 + 8(\frac{|r^*|}{l})^3 + 6(\frac{|r^*|}{l})^2 + 1\right), \tag{4.3}$$

while for $|\mathbf{r}^*| >= l$, the functions used in the following analyses is as

$$w(r) = 0. \tag{4.4}$$

### 4.3.3 Virtual imaging

In addition to coarse graining, we utilise the discrete particle data to generate artificial radiographs using a forward projection method, similar to the one described in Chapter 3, since the rheography of these artificial radiographs can be used to compare with the corresponding rheographic results using experimental radiographs to get a better idea of how well the rheography methods reconstruct the internal velocity in real and simulated cases. The artificial X-ray intensity $I_f$, the mean intensity $\text{avg}(I_f)$, and the logarithm of the normalised intensity $\log\left(\frac{I_f}{\text{avg}(I_f)}\right)$ from the virtual X-ray setup along the X-axis are shown in Figures 4.9 a, 4.9 b and 4.9 c, respectively. The artificial radiographs obtained from three orthogonal directions during mixing are normalised, as shown in Figure 4.10.

a 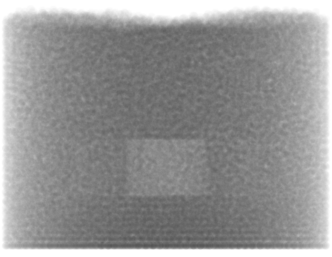 b  c 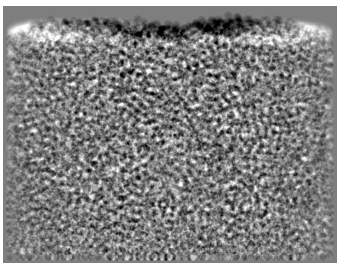

FIGURE 4.9: Artificial radiograph for 3 mm glass beads along the normal to X-axis showing: a) Measured X-ray intensity $I_f$ of the container; b) Mean intensity $\text{avg}(I_f)$; c) Normalised intensity $\log\left(\frac{I_f}{\text{avg}(I_f)}\right)$ used for deconvolution.

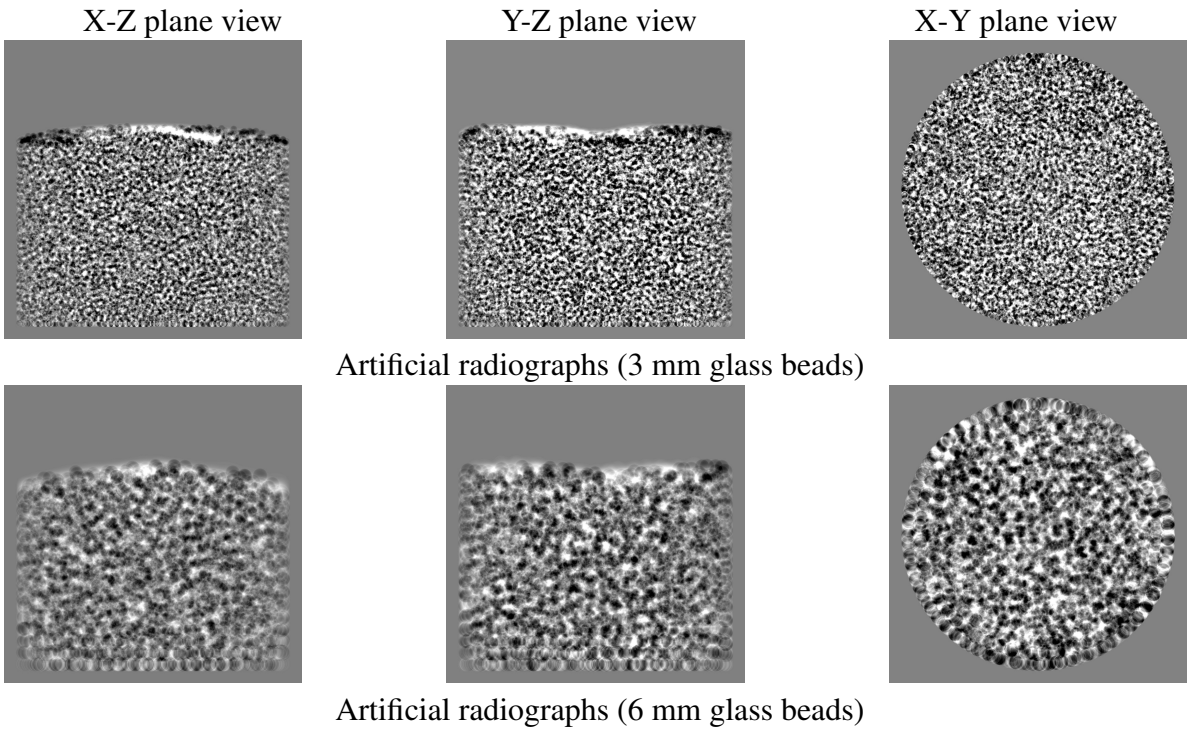


FIGURE 4.10: Normalised artificial radiographs while mixing 3 mm and 6 mm spherical glass beads used in the study.

Both virtual radiographs created using forward projection techniques (see Figure 4.10) and experimental radiographs (see Figure 4.11) and exhibit similar features of particle organisation, such as the layering of grains, particularly in 6 mm glass beads. The artificial images appear to be more exposed than the real radiographs, indicating that adjusting the attenuation coefficient could yield more realistic results. These artificial radiographs are used primarily to compare the rheographic results (from the artificial images) with the experimental one. As such, achieving perfect image contrast and brightness alignment with the experimental radiographs is not essential.

### 4.3.4 Internal velocity reconstruction

Our global coordinate system uses three perpendicular directions $(X, Y, Z)$. For simplicity, local imaging coordinates $(\xi, \eta)$ are used to refer to the two in-plane directions in each image,

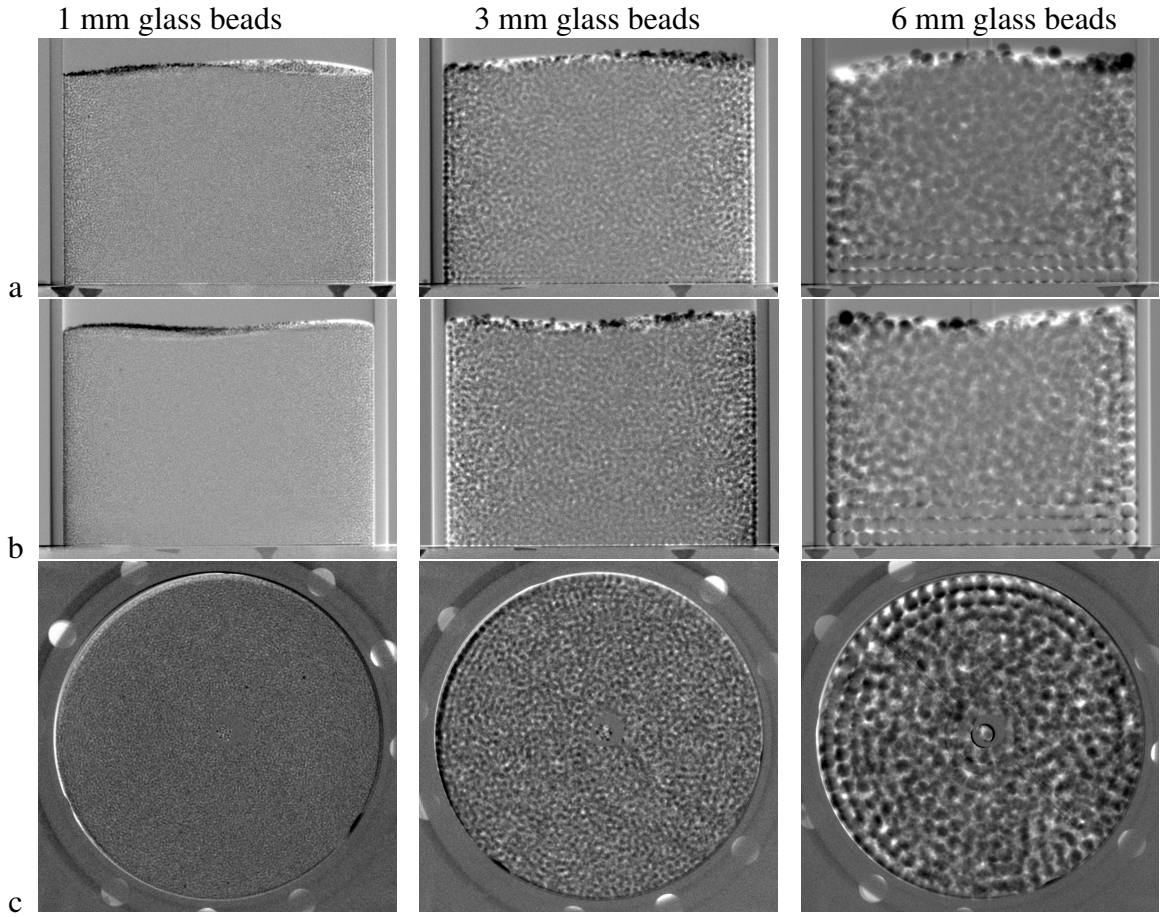


FIGURE 4.11: Normalised experimental radiographs of 1 mm, 3 mm, and 6 mm spherical glass beads used in the study showing three orthogonal viewing directions: a) normal to X-axis, b) normal to Y-axis, and c) normal to Z-axis.

which are related to the global axes as

$$\begin{aligned}(\xi^{(1)}, \eta^{(1)}) &\rightarrow (Y, Z),\\ (\xi^{(2)}, \eta^{(2)}) &\rightarrow (Z, X),\\ (\xi^{(3)}, \eta^{(3)}) &\rightarrow (X, Y),\end{aligned} \tag{4.5}$$

as shown in Figure 4.1. Image correlation and convolution analysis are performed within the interrogation windows for each successive pair of preprocessed logarithmic images represented as $L_1$ and $L_2$, respectively. The difference is that, unlike in Chapter 3, where we only extract information on vertical displacements from each image, we now extract information on two in-plane displacements from a single image. For example, from the projection along the $X$ direction, we extract information about the displacement in the plane along the $Y$ and $Z$

directions simultaneously. Thus 2D auto-correlation $(A)$ and cross-correlation $(C)$ functions within each interrogation window are computed as

$$A(m,n) = \sum_{p} \frac{\left(L_1(m+p, n+q) - \bar{L}_1\right)\left(L_1(p,q) - \bar{L}_1\right)}{\sigma_1^2}, \tag{4.6}$$

$$C(m,n) = \sum_{p} \frac{\left(L_1(m+p, n+q) - \bar{L}_1\right)\left(L_2(p,q) - \bar{L}_2\right)}{\sigma_1 \sigma_2}, \tag{4.7}$$

where $m$ and $n$ represent discrete pixel displacement and $p$ and $q$ denote pixel position, while $\bar{L}_1$, $\bar{L}_2$, $\sigma_1$, and $\sigma_2$ denote the mean and standard deviation of the log of the intensities taken over each window. Subsequently, the actual displacement PDF of the material is determined through the convolution equation (Dubsky et al. 2010) as

$$C = A * f, \tag{4.8}$$

where $'*'$ is discrete convolution operator, and $f$ represents the PDFs of displacements within the window. The methods are the same as those explained in Chapter 3. We use 2D PDFs to calculate discrete displacement vectors to reconstruct internal velocities. These vectors are compared with data from the orthogonal direction to find the pair with the lowest matching error (Baker et al. 2018). The velocity is then reconstructed using the mean of the matching pair. This process is applied consistently in all global directions and positions, using radiographs from three orthogonal directions.

## 4.4 Results and Discussion

Reconstructed velocities $u$, $v$, and $w$ represent the velocity components along the axes $X$, $Y$, and $Z$, respectively. These components are compared across three approaches: X-ray-based rheography, coarse-grained velocity fields from a DEM mixer, and rheographic analyses of artificial radiographs generated from DEM simulation data (see Figure 4.12). Both the rheographic and DEM results exhibit significant similarities in the overall flow behaviour; however, the rheographic findings display more noise, likely due to the finite resolution of the radiographs, in contrast to the smoother flow patterns predicted by the coarse graining of DEM. Furthermore, variations in material properties, such as friction coefficients and

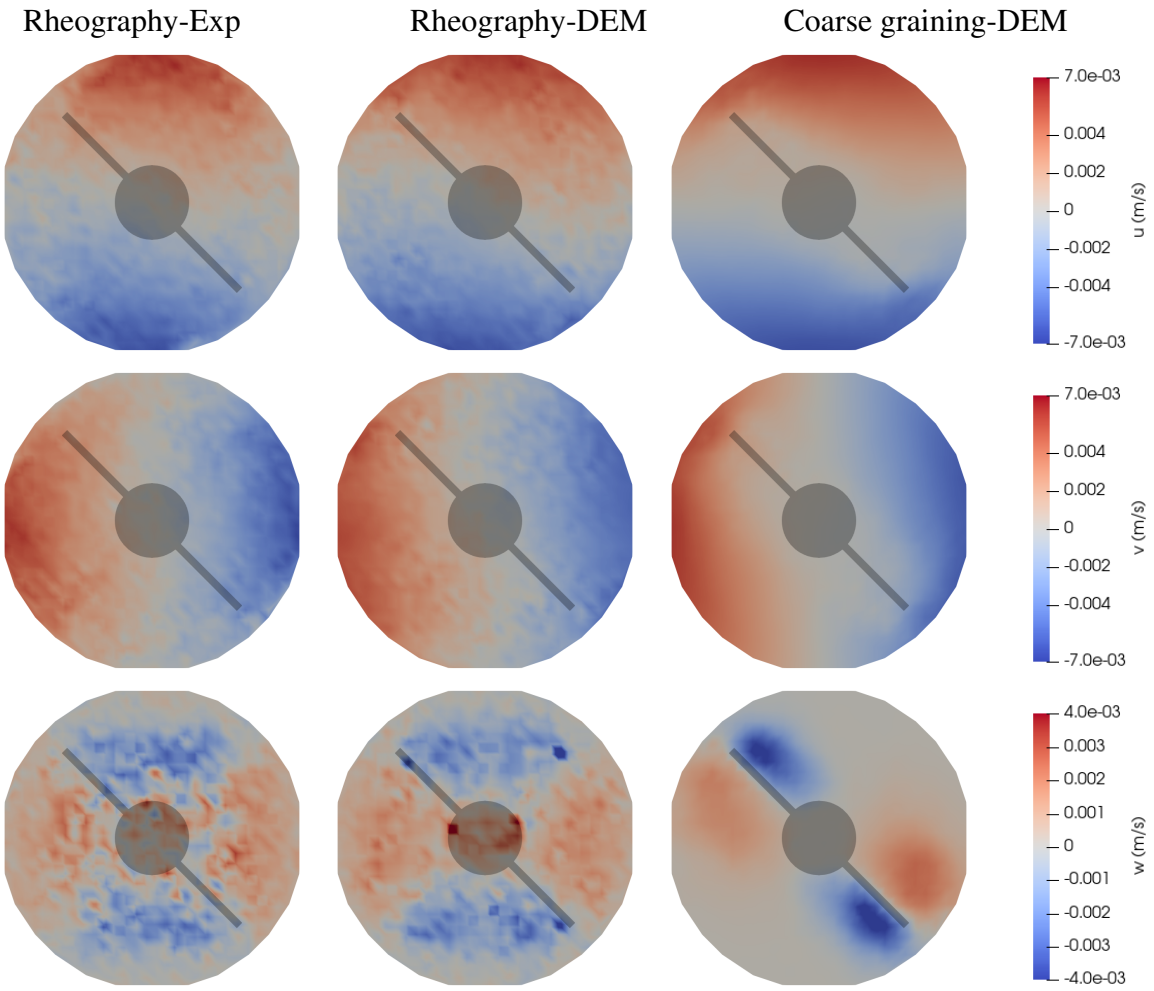


FIGURE 4.12: Comparison of velocity contour obtained from rheographic results based on experimental real x-ray radiographs, rheographic results based on DEM artificial radiographs, and coarse-graining DEM results at the top level of the impeller blade (z2, see notation in Figure 4.13) during the mixing of 3 mm glass beads.

restitution, between experiments and simulations may influence the comparison. Despite these discrepancies, the rheographic study effectively captures key flow motions, underscoring its value as an experimental technique. This consistency across the rheographic results underscores the reliability of the forward projection method, which is based on Beer-Lambert's attenuation law, for analysing granular flow in virtual studies.

The experimental results align more closely with the rheographic analysis of artificial DEM radiographs than with predictions from coarse-grained DEM models. However, we observe some differences in the axial velocity patterns predicted by coarse-grained DEM and

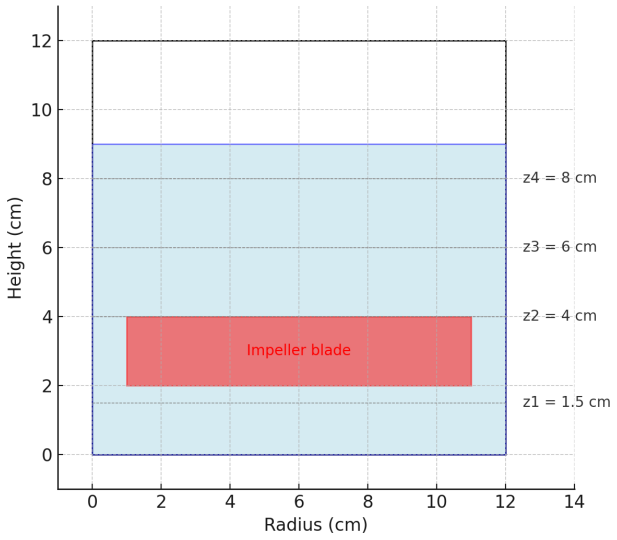


FIGURE 4.13: Schematic of the cylinder with impeller blade showing different vertical positions used in subsequent analysis.

the rheographic method. As demonstrated in Chapter 3, rheography effectively reconstructs velocity in anti-symmetric flow by projecting the X-ray axis at 45 degrees when there are equal quadrants of opposing flow. However, the assumption of equal quadrants of opposite flow may not hold in cases of mixing, which could explain these differences.

For a more detailed quantitative comparison, we convert cartesian coordinates $(X, Y, Z)$ into cylindrical coordinates, which consist of radial $v_r$, tangential $v_\theta$, and axial $v_z$ components as:

$$v_r = u\cos(\theta) + v\sin(\theta), \tag{4.9}$$

$$v_\theta = -u\sin(\theta) + v\cos(\theta), \tag{4.10}$$

$$v_z = w, \tag{4.11}$$

where $\theta$ is the azimuthal angle around the Z-axis, measured from the X-axis. We will focus on the tangential velocity components responsible for circular motion during mixing and quantitatively examine them at various mixer heights and discuss the results.

The tangential velocity component reconstructed from rheographic analysis due to the action of the X-ray, and subsequently circumferentially averaged for radial analysis, is compared with the corresponding velocity component obtained through coarse-graining at the same heights (see Figure 4.14). This comparison is quantitatively assessed by normalising $v_\theta$ against

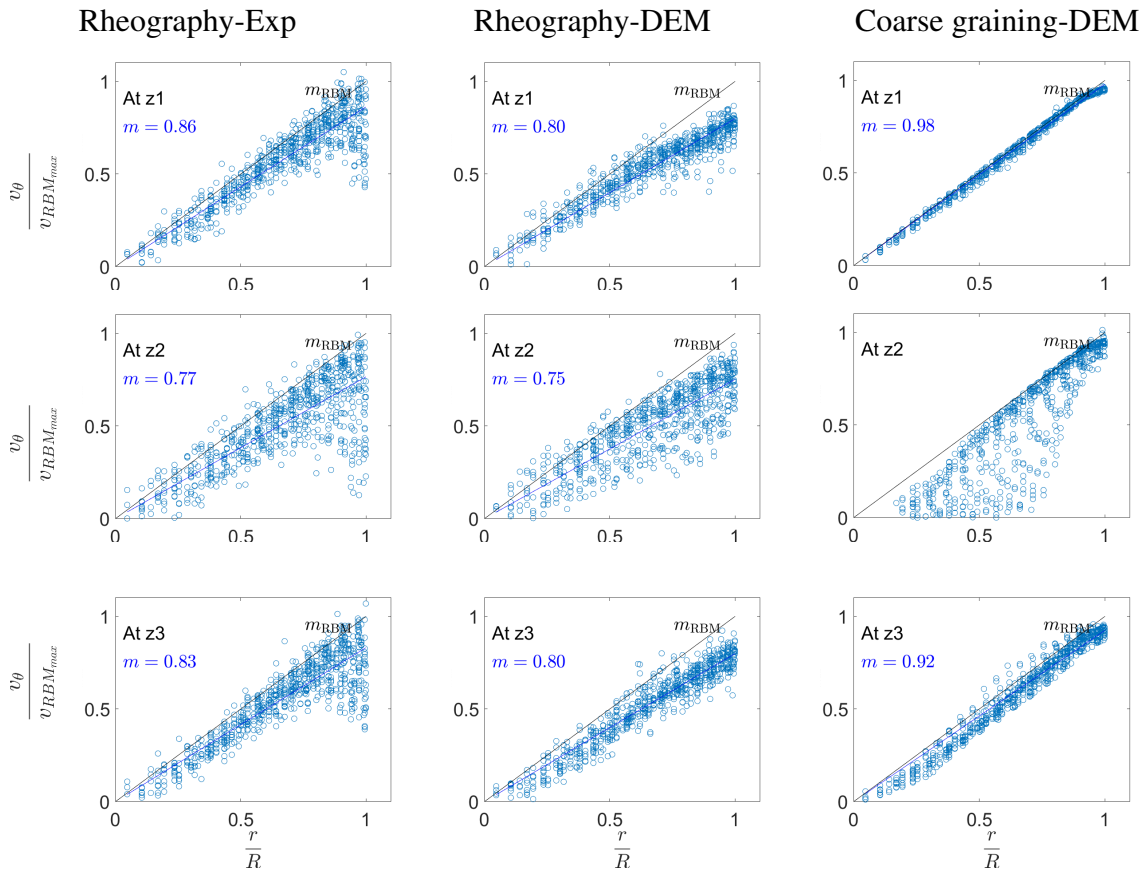


FIGURE 4.14: Comparison of tangential velocity resulting from the action of X-ray in rheographic results using real X-ray radiographs and DEM artificial radiographs, with coarse-grained DEM predictions at positions z1, z2, and z3, while mixing 3 mm glass beads. Here, $m$ represents the best-fit slope, $m_{RBM}$ denotes the RBM slope, and $r/R$ is the normalized radius (where $r$ is the radial distance and $R$ is the mixer radius.)

the maximum rigid body motion (RBM) velocity ($v_{RBMmax}$) along the radius. All analysis approaches indicate that the slope of the best-fit line ($m$) is below the rigid body rotation line ($m_{RBM}$). In addition, the slope values ($m$) are higher below the blade (z1, per Figure 4.13), indicating that the impeller blade has little effect in this region, leading to a mainly circular motion. The coarse-grain results show a clearer linear velocity plot that supports this observation, with the rheographic results aligning with the DEM findings with some noise.

Near the blade, the slope values decrease compared to the position below it. At height z2 (per Figure 4.13), the rheographic results slightly differ from the DEM predictions. The rheographic velocity results exhibit a linear relationship between the velocity component and the radial variations originating from the centre of the mixer. In contrast, the coarse-grained

DEM results show a minor shift. This difference arises because the coarse-graining algorithm in DEM treats the geometry of the blade and the central hub (the impeller part connecting the blades to the shaft) as a void (see Figure 4.14 at z2). In contrast, rheographic analysis incorporates the projected impeller blade, which introduces noise near the central hub. This difference may skew the interpretation of the velocity fields near the impeller.

At the height above the blade (z3), the rheographic and DEM coarse grain results realign, with the slope value increasing compared to that near the blade. This alignment indicates that, except near the central hub, rheography and DEM results generally match. The change in slope values at various heights within the cylinder shows some relationship between velocity and the distance from the impeller blade (see Figure 4.15). Near the blade, the slopes decrease before rising again at higher elevations, indicating reduced mixing velocity in that region. These findings are consistent with similar observations reported in the literature (Zhou 2002). While comparing the results from various methods used for the study, we observed that the rheographic method slightly underestimates the velocities compared to coarse-graining. This reduction in reconstructed velocity is more pronounced for 6 mm beads than for 3 mm ones, raising concerns about particle size sensitivity.

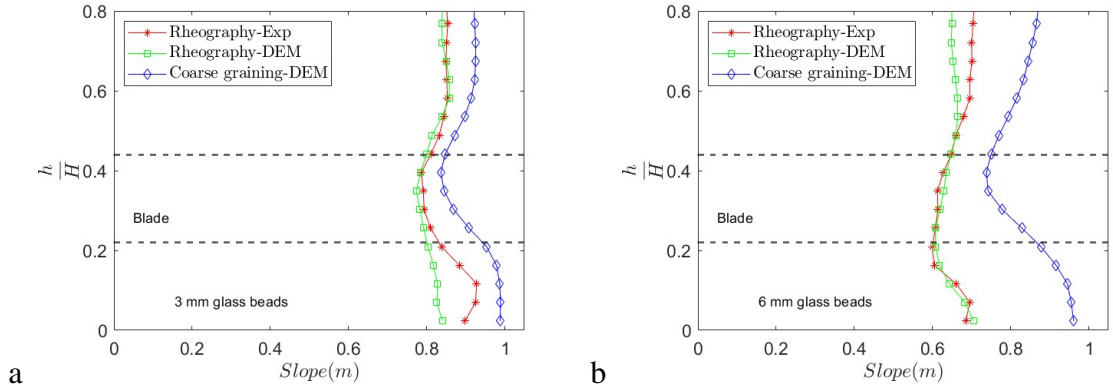


FIGURE 4.15: Variation of best-fit line slope (m, per Figure 4.14) along the mixer height from DEM simulations and rheography: a) 3 mm glass beads; b) 6 mm glass beads.

To assess whether the size of the interrogation window used for deconvolution influenced these results, we reconstructed the internal velocities for 3 mm beads using two window sizes: 180 × 180 pixels² (matching the size used for the 6 mm beads) and 90 × 90 pixels² (refer to Figure 4.16).

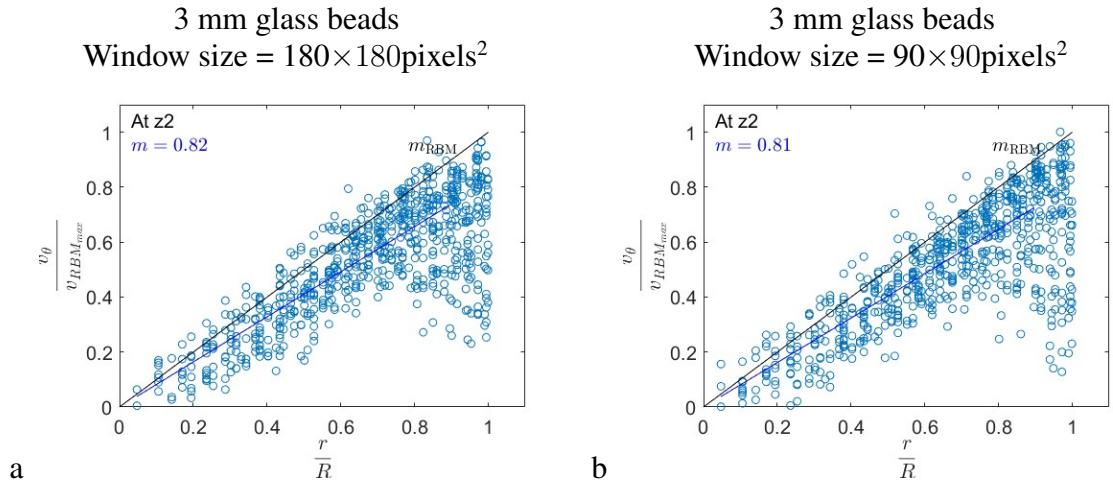


FIGURE 4.16: Variation showing the circumstantially and depth averaged tangential velocities normalised by the maximum Rigid Body Motion (RBM) velocity along the radius to study the effect of interrogation window size.

The findings did not show significant differences between the two window sizes. Consequently, the variations observed in Figure 4.15 for 6 mm grains likely reflect a pattern linked to boundary crystallisation. This phenomenon, characterised by the structural ordering of particles near the walls, leads to reduced local velocities and alters the overall mixing behaviour. A quantitative evaluation (see Figure 4.17) supports this observation, as the slope of the best-fit line for 3 mm glass beads (m = 0.77) exceeds that for 6 mm beads (m = 0.61).

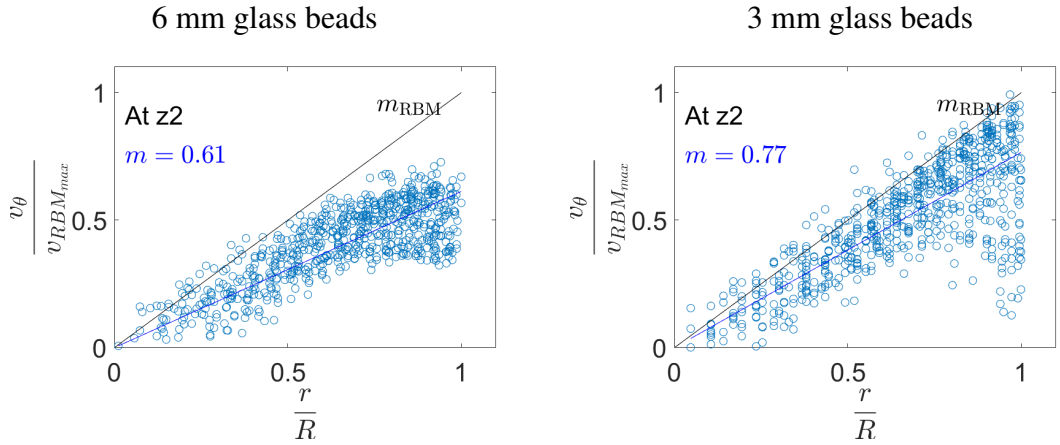


FIGURE 4.17: Rheographic results for tangential velocity, as previously discussed, demonstrate the impact of particle size at the top level of the impeller blade (z2, see notation in Figure 4.13) when mixing 6 mm and 3 mm glass beads.

Although both bead sizes initially exhibit a similar trend, deviations occur at the boundary as the radial distance increases, where layering occurs. Evidence of boundary layering was observed in both experimental and simulation radiographs. Interestingly, when boundary crystallisation is examined quantitatively, we observe that the number of layers exhibiting glass bead crystallisation in 6 mm experimental radiographs is three, while in corresponding artificial radiographs it is two. These differences in crystallisation patterns could stem from variations in simulation parameters rather than those present in the experiments. As reported in the literature (Boonkanokwong 2018), scaling up systems with cohesionless monodisperse spherical particles by increasing the mixer-to-particle diameter ratio has minimal impact on granular flow behaviours and mixing kinetics. Our coarse-graining results align with this observation, even though we varied the grain size while keeping the mixer dimensions constant, rather than scaling the system proportionally. However, the rheographic results significantly deviate, indicating that particle size and its distribution variability are critical factors for using the rheography technique. These findings highlight the need for further investigation into the interplay between particle size and rheographic accuracy. While further exploring the impact of particle size, including attempts to evaluate smaller glass beads (e.g. 1 mm), reconstructing the internal velocities for 1 mm grains presents experimental challenges (see Figure 4.18).

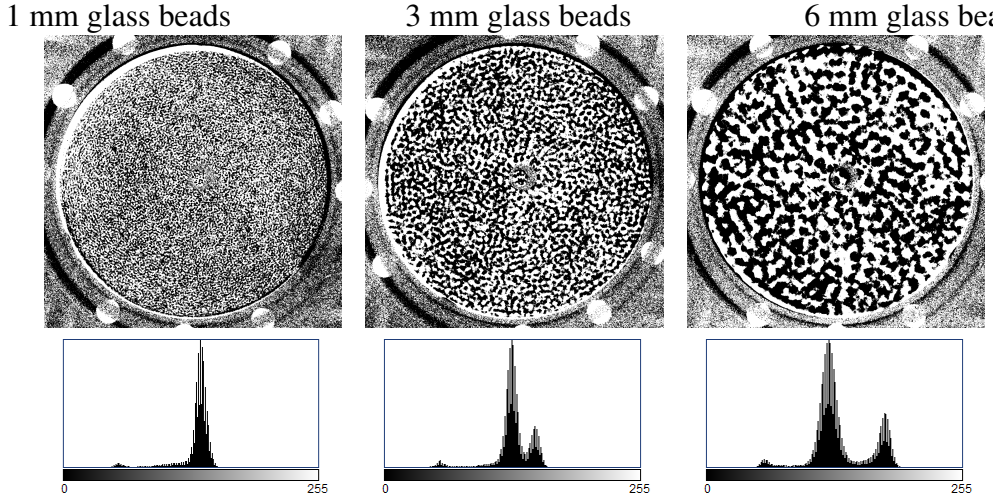


FIGURE 4.18: Analysis of radiographs for 1 mm, 3 mm, and 6 mm glass beads showing improved X-ray intensity and pixel value statistics distribution.

The reduced texture of the density field within the beam complicates the detection of essential density variations required for image correlation and meaningful results. Since

the resolution for 1 mm grains is suboptimal, the streamlines of the flow path do not yield meaningful results with such small grains (see Figure 4.19). Furthermore, the other two meaningfully extracted streamlines indicate that 3 mm glass beads exhibit higher flow velocities (more reddish in Figure 4.19) than those of 6 mm beads.

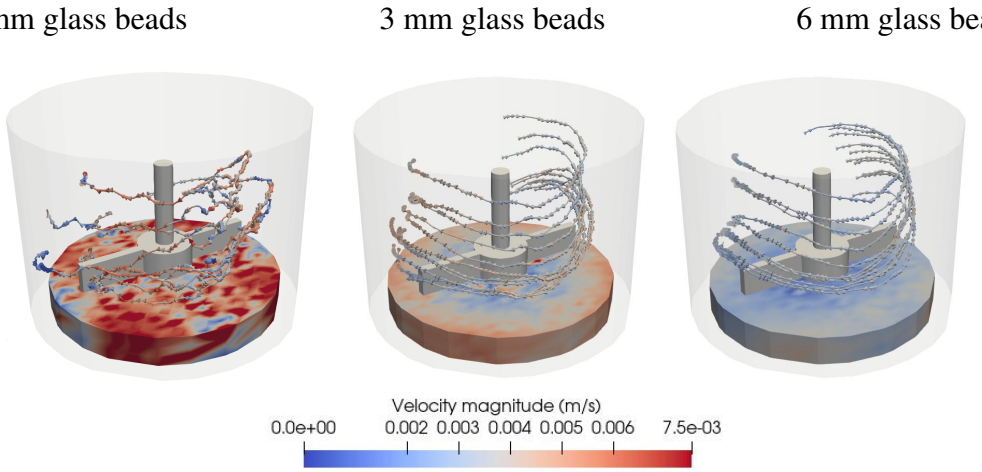


FIGURE 4.19: Rheographic results show the velocity streamlines around a blade with a cross-section of the 3-D contour of the velocity magnitude $|\mathbf{u}| = \sqrt{u^2 + v^2 + w^2}$ below the bottom level the blade from the experimental mixing of 1 mm, 3 mm, and 6 mm glass beads.

The precision of the rheographic technique depends on the data from the radiographs analysed and the deep velocimetry algorithm employed. Our study assumes steady-state conditions in the granular mixing, which is essential for accurate velocity assessment. We focused on quantitatively analysing the kinematic energy to assess mixing process stability. Although experimentally measuring the kinetic energy is difficult, DEM simulations offer a data set for quantitative analysis across different particle sizes. Figure 4.20 illustrates that smaller glass beads steadily reach a stable mixing state, while larger grains show increased variability with higher standard deviations. This variability creates uncertainty in conclusions from methods designed for ideal steady states, highlighting the impact of particle size on energy balance and the reliability of rheographic analysis.

X-ray rheography is a novel technique for studying granular mixing dynamics, but it has certain limitations. Its precision is affected by the variability of the particle size, which complicates analysis. However, it yields better results for particles around 3 mm. Despite slightly underestimating velocities, this consistency is validated by correlating coarse-graining

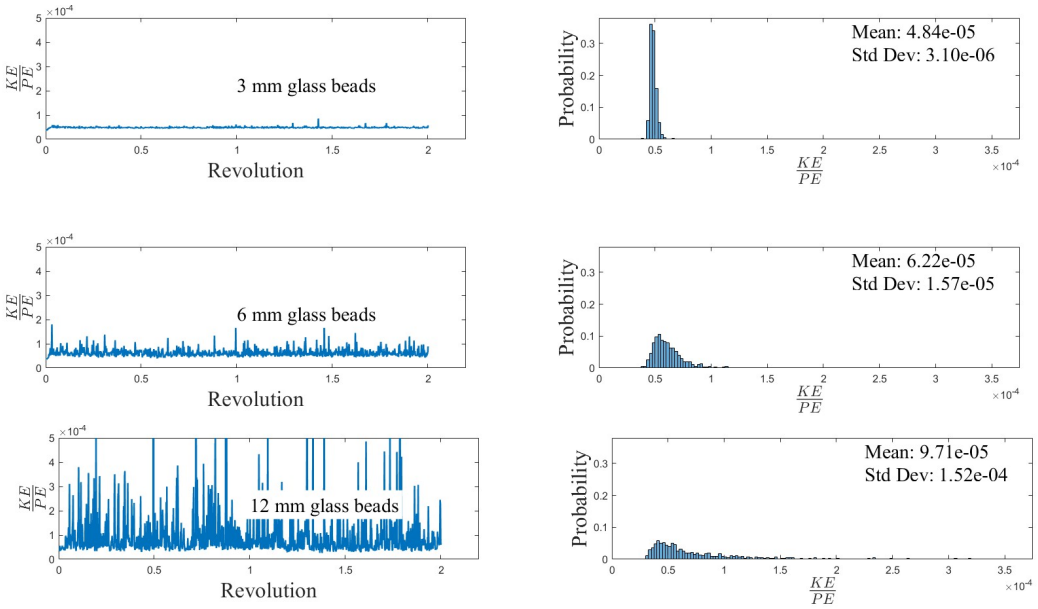


FIGURE 4.20: Variation of kinetic energy normalised by potential energy to examine the equilibrium of the mixing process

predictions in DEM simulations. Our method also accurately captures the reduced velocities near the boundaries where particle ordering occurs. These findings confirm that, despite some challenges, X-ray rheography is effective for granular mixing analysis when used with appropriately sized particles. Although conducted in small-scale lab settings with resolution constraints, these concepts can be applied to other systems. These insights will later aid in understanding the effects of particle shapes on mixing dynamics in this thesis.

## 4.5 Summary

This chapter evaluates the capacity of X-ray radiography to analyse granular mixing. An experimental mixer was designed to produce radiographs that capture granular mixing, allowing the extraction of mixing kinematics. These were compared with DEM simulations, which showed qualitative agreement and validated the technique. The findings highlight the potential of X-ray rheography for studying granular mixing. The next chapter examines the impact of particle shape and impeller blade design on mixing kinematics.

CHAPTER 5

# Effect of particle shape and impeller blade angle on mixing kinematics

The mixing kinematics in granular mixers is controlled by how the particles interact with other particles and the boundaries of the mixer, especially its impeller blades. However, despite great progress in the field, there is still a lack of complete understanding of this problem. This study aims to shed more light on the problem by using the X-ray method, a noninvasive observation technology that can be used for granular flow studies. This Chapter investigates the effects of the angles of the impeller blade on the bulk kinematics given three different shapes of grains: spherical glass beads, oblate barley, and prolate jasmine rice. We used deep velocimetry and novel X-ray rheography techniques to explain flow kinematics and a Fourier transformation technique to analyse fabric orientation. The 3D internal velocity field reconstructed using deep velocimetry and X-ray rheography indicates that the mixing kinematics of elongated particles is significantly affected by different angles of the impeller blade. Specifically, analysis of the fabric orientation field demonstrated that jasmine rice, which has the highest degree of elongation, exhibited the most pronounced orientation. At the same time, barley showed a comparatively weaker but similar trend. As anticipated, the spherical glass beads did not demonstrate meaningful alignment as they are not elongated. The findings of this study were cross-validated using the discrete element method (DEM) under similar mixing conditions, producing comparable results and thereby demonstrating the effectiveness of X-ray methods in visualising the internal kinematics and fabric orientation fields during the granular mixing of various particle shapes.

## 5.1 Overview

Industrial processes often use cylindrical mixers equipped with impeller blades (Litster et al. 2002; Mateo-Ortiz and Méndez 2015). These blades come in different geometries, such as

vertical and tilted designs, suited to various industry applications. Furthermore, the mixed particles can possess diverse shapes and sizes, ranging from rounded to elongated, significantly affecting the mixing behaviour. Understanding the interplay between impeller geometry and particle shape can be a useful knowledge input to optimise mixing efficiency and product uniformity. Thus extensive research has been conducted using the discrete element method (DEM) to recover information within the bulk of granular mixers (Metzger et al. 2011, Hare and Ghadiri 2013, Capece et al. 2015, Guo et al. 2017) to optimise granular mixing. DEM simulates granular materials by modelling them as collections of distinct particles interacting according to Newton's laws of motion (Cundall and Strack 1979). Although advances in computational power have increased the popularity of DEM simulations (Zhu et al. 2008), many still rely on spherical particles for simplicity and efficiency. However, this simplification often fails to capture the true behaviour of real materials, as the packing density and flowability differ significantly between spherical and nonspherical particles (Cleary 2010). For example, DEM simulations (Boonkanokwong et al. 2016) have been used to model the effects of impeller blades on spherical particles. However, these models depend on simplifying assumptions that may limit their accuracy, even in granular systems with a relatively small number of grains.

Various strategies have been developed to address the challenge of representing non-spherical particles in a more realistic way. One common approach is the multisphere (MS) method (Abbaspour-Fard 2000, Kremmer and Favier 2001), which approximates complex shapes by overlapping and gluing spheres to form agglomerated particles with arbitrary geometries. However, this method has significant computational costs. Research revealed that using 25 primary spheres to approximate ellipsoidal particles leads to a 17-fold increase in CPU time (Markauskas et al. 2010). Additionally, a drawback of the MS method is the presence of non-smooth surfaces and subsequently multiple contact points (Kruggel-Emden et al. 2008). Using this method for the approximation of convex particles (such as ellipsoids) with multiple primary spheres cannot be done without introducing artificial non-convex surface textures. Attempts to smoothen these surfaces using more subspherical particles yield a larger number of contacts between two agglomerated particles (Markauskas et al. 2010). An alternative option is the use of polyhedral particles, which models particle surfaces with polygons in 2D or triangles in 3D (Cundall 1988). Although this method provides considerable versatility, the complexity

of calculating contact forces introduces new computational challenges. Therefore, experimental methods are necessary to validate these models and ensure their applicability to real-world granular systems. In such scenarios requiring experimental solutions, X-ray radiography has emerged as a powerful technique, both for validating DEM studies and for accessing situations that remain beyond the computational reach of such numerical methods. This X-ray imaging technique offers several advantages, particularly in preserving the non-destructive nature of the analysis and minimising boundary layer effects near walls, which may otherwise influence interpretations when relying solely on direct measurements against visible walls.

A crucial aspect of understanding mixing kinematics is understanding the orientation of the fabric within the bulk of the material, providing a more refined representation of granular flow dynamics. Recent advances in high-speed X-ray radiography have significantly enhanced our ability to study these dynamics, allowing the visualisation of fabric field evolution over time and space (Guillard et al. 2017). Using this fabric determination technique based on the Fourier transformation, we conducted an experimental study investigating the connection between internal fabric evolution and velocity fields within a cylindrical mixer. Our experiments included spherical grains (glass beads) and anisotropic grains (barley and jasmine rice), enabling us to evaluate the effects of particle-shape anisotropy and impeller blade orientation on mixing behaviour. To validate our experimental findings, we used a DEM model that offers three key benefits. First, it facilitates the comparison of experimental kinematics results with those obtained by coarse-graining DEM velocity fields. Second, it provides discrete information on the position and orientation of each particle in time and space, allowing the development of simulated radiographs, where the Fourier transform method (Guillard et al. 2017) can be used to compare with the fabric orientation field obtained from experimental X-ray radiographs. Finally, while the initial focus is on depth-averaged fabric alignment, validating the DEM model using experiments allows for a more reliable investigation of fabric orientation in 3D using that same DEM.

## 5.2 Method

We mixed the same mass of materials of various shapes (initially poured into the vessel in a random loose packing) with a rotation period of 58.3 seconds. Figure 5.1 and Table 5.1 show


FIGURE 5.1: Shapes of grains used in the experimental investigation

TABLE 5.1: Sizes of grains used in the experimental investigation

| Material | Major axis (2a) (mm) | Intermediate axis (2b) (mm) | Minor axis (2c) (mm) | Aspect ratio ($\frac{a}{c}$) |
|---|---|---|---|---|
| Jasmine rice | 7.22 | 2.07 | 1.69 | 4.25 |
| Barley | 6.94 | 3.62 | 2.66 | 2.60 |
| Glass beads (3 mm) | 2.83 | | 2.81 | 1.01 |

the grain shape and sizes of the materials used in the experiments, respectively. We tested two different impeller blade configurations: one had a blade angle of $90°$ and the other inclined at $145°$, as shown in Figure 5.2. For simulations, we introduced one more variation by inspecting an additional angle between the two others used in the experiments to observe an intermediate scenario.

a b c

FIGURE 5.2: Blade configurations utilised in the study with blade angle: a) 90°; b) 117.5°; and b) 145°

Similar to Chapter 4, we acquire sequential radiographs from three orthogonal directions. In Figure 5.3 a, we see the experimental radiograph of an empty container from a side projection. The X-rays are orientated at a 45-degree angle to the blade axis, thereby reducing antisymmetry issues for rheographic analysis (as discussed in Chapter 3). Figure 5.3 b shows the intensity of the X-rays of the container. For velocity measurements, as discussed in previous chapters,

normalisation is performed with the average intensity (see Figure 5.3 c), followed by computing the logarithm of the normalised intensity (as shown in Figure 5.3 d). The logarithm of the normalised intensity (see Figure 5.4) is used in deconvolution to extract internal velocity information for various particles. We have discussed the rheographic method in detail for extracting these internal velocity vectors in Chapters 3 and 4.

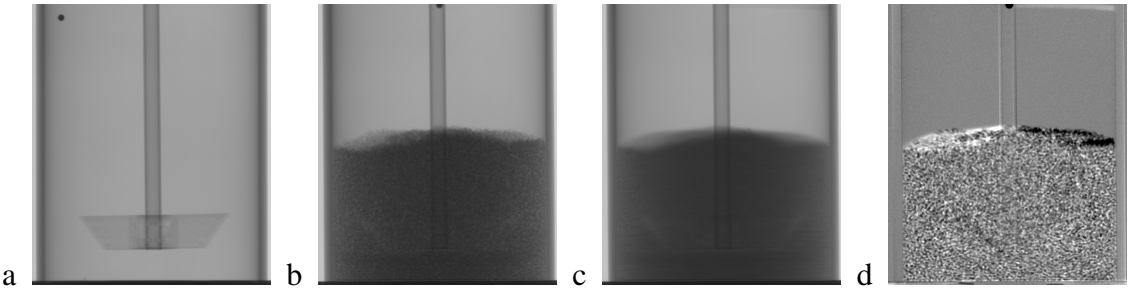


FIGURE 5.3: Experimental radiograph of a mixer filled with jasmine rice along X-axis illustrating: a) measured X-ray intensity $I_e$ of the empty container; b) measured X-ray intensity $I_f$ of the container with jasmine rice; c) mean intensity avg$(I_f)$; and d) normalised intensity $\log\left(\frac{I_f}{\text{avg}(I_f)}\right)$ utilised for deconvolution.

X-ray radiographs additionally enable the determination of fabric orientation, which affects the spatial wavelength and direction of density fluctuations shown in the images. Thus, the orientation field can be recovered by applying a two-dimensional Fourier transform to the measured intensity. In this Chapter, we focus more on technique to recover internal orientation fields in granular mixing from radiographic images to add new light to the findings regarding velocity measurement. Building on this approach, we employ a Fourier transformation technique to extract the fabric orientation field from radiographic images systematically.

### 5.2.1 Fabric orientation determination technique using X-ray radiographs

For the recovery of the fabric orientation field using the Fourier transformation approach (Guillard et al. 2017), each radiograph (see Figure 2.9) is subdivided into square patches with a width of $w = 48$ pixels and an overlap of 50% between adjacent patches. The intensity of each patch is normalised by its average intensity and the patch is scaled by a radial Hamming window, defined as

$$W(r) = \frac{\cos\left(\frac{2\pi r}{w}\right)}{2}, \tag{5.1}$$

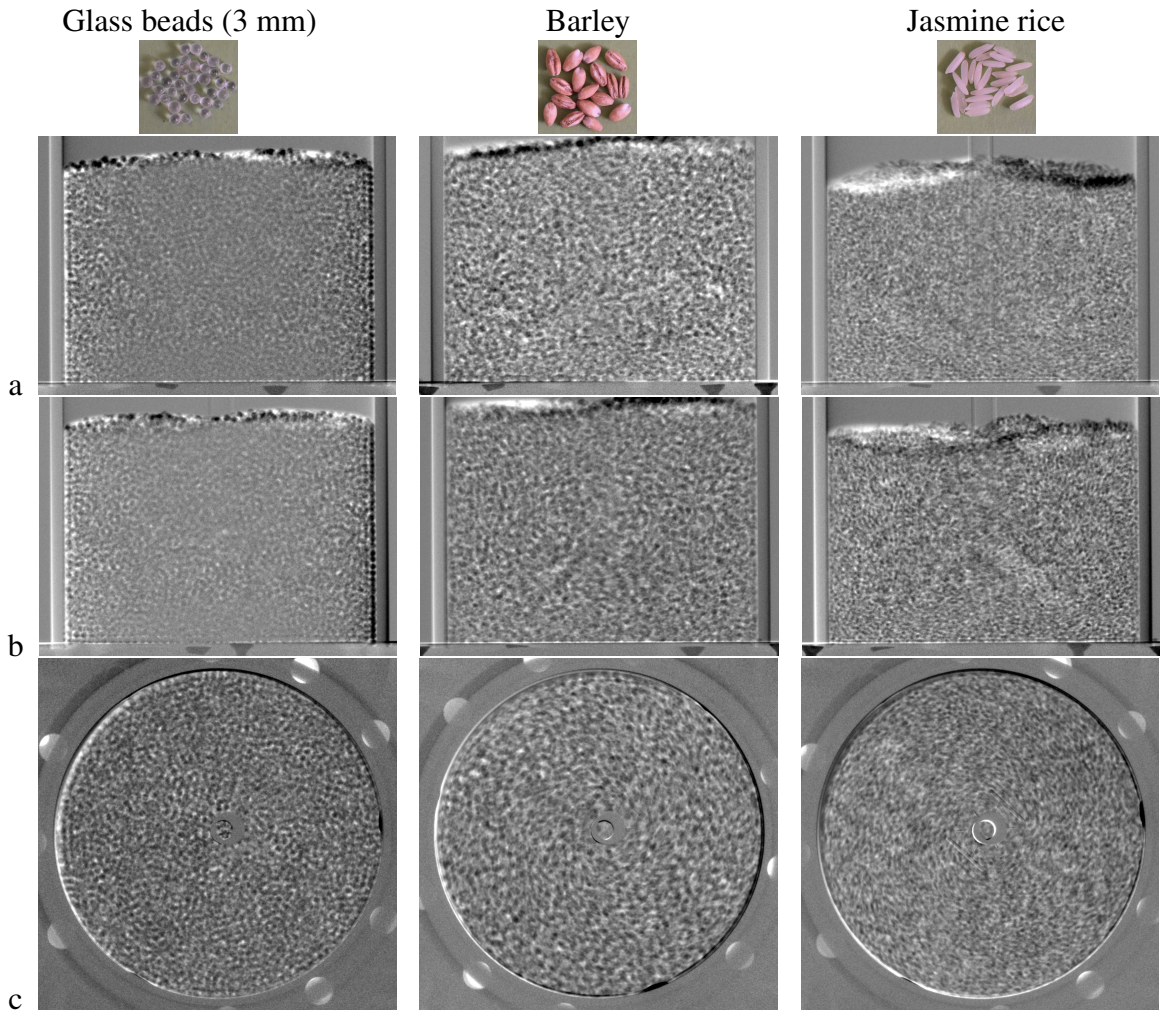


FIGURE 5.4: Normalised experimental radiographs of 3 mm spherical glass beads, barley, and jasmine rice used in the study showing three orthogonal viewing directions: a) normal to X-axis, b) normal to Y-axis, and c) normal to Z-axis.

where $r$ represents a pixel's distance from the patch's centre. The circular Hamming function reduces the impact of boundary effects during the Fourier transform. Specifically, by tapering the intensity values at the patch's edges according to the Hamming window, the function ensures smooth transitions between the patch and its surroundings. A two-dimensional Fourier transform (Guillard et al. 2017) is then applied to each patch, represented as

$$S(\overrightarrow{k}) = \left| \iint I(\overrightarrow{x}) \times W(r(\overrightarrow{x})) \exp(2i\pi \overrightarrow{k} \cdot \overrightarrow{x})\, d\overrightarrow{x} \right|^2, \tag{5.2}$$

which provides the power spectrum $S$ as a function of the wave vector $overrightarrowk$, where $I(overrightarrowx)$ represents the intensity at the pixel location $overrightarrowx$ within the patch. The power spectrum is used to analyse the distribution of density fluctuations within the image. By transforming the image data from the spatial domain to the frequency domain, the power spectrum is used to recover information about the orientation of the particles in the granular flow. The peak in the power spectrum corresponds to dominant spatial frequencies, which relate to the particle's preferred alignment.

The principal orientation of the particles is derived from the power spectrum by averaging the weighted nematic-order tensor. Assuming that all density fluctuations in a patch are aligned, the energy in the power spectrum is concentrated along a single line which is orthogonal to the direction of the density fluctuations. This enables the measurement of the orientation of the fabric through angular averaging (Pourdeyhimi et al. 1997), although this method may produce inaccurate results when fluctuations are only weakly orientated. Furthermore, this analysis does not convey information regarding the intensity of the orientation. To address this, we improve the treatment of the power spectrum by associating each component of the power spectrum with a structure tensor $\overrightarrow{Q}$ (Bigun 1987, Mottram and Newton 2014). The nematic order tensor can then be obtained by adding the weighted structure tensors ( Börzsönyi et al. 2016). Given the discrete spatial sampling, each component of the power spectrum in the wave vector $\overrightarrow{k} = (k_x, k_y)$ integrates the energy of density fluctuations over a range $[k_x \pm \Delta k_x/2, k_y \pm \Delta k_y/2]$. Each component of the power spectrum is then associated with a structure tensor $Q(\overrightarrow{k})$, which is given by

$$Q(\overrightarrow{k}) = \frac{1}{\Delta k_x \Delta k_y} \int_{k_x-\Delta k_x/2}^{k_x+\Delta k_x/2} \int_{k_y-\Delta k_y/2}^{k_y+\Delta k_y/2} \frac{\overrightarrow{k} * \overrightarrow{k}}{\left|\overrightarrow{k}\right|^2} d\overrightarrow{k}. \tag{5.3}$$

The norm of the tensor $\overrightarrow{Q}$ tends to be close to 1 for small wavelengths (large wave vectors, $(\overrightarrow{k} \gg \Delta k_x, \Delta k_y)$ and decreases for larger wavelengths, as the components of the power spectrum integrate energy in a wider range of directions (that is, $k_x \sim \Delta k_x$ and $k_y \sim \Delta k_y$). The orientation tensor is then weighted by the power spectrum components, leading to the two-dimensional nematic order tensor for the patch, defined as

$$\overrightarrow{T} = \sqrt{2}\left(\frac{\sum_k S(\overrightarrow{k})Q(\overrightarrow{k})}{\sum_k S(\overrightarrow{k})} - \frac{1}{2}\overrightarrow{I}\right), \tag{5.4}$$

where $\overrightarrow{I}$ is the identity tensor, the tensor $\overrightarrow{T}$ defined in this manner is traceless, and we define the ordering parameter (following Guillard et al. 2017) as $||\overrightarrow{T}|| = \sqrt{T_{ij}T_{ij}}$, with $||\overrightarrow{T}|| = 0$ for an isotropic power spectrum (no preferred orientation) and $||\overrightarrow{T}|| = 1$ for a power spectrum with all energy concentrated in a single direction. To reduce the noise in the power spectrum, we also average $\overrightarrow{T}$ over time to obtain $\overrightarrow{\overrightarrow{T}}$. The chosen time window is large enough to eliminate fluctuations in $\overrightarrow{T}$, but small enough to guarantee that $\overrightarrow{T}$ stays quasi-steady. This method is appropriate for the flows analysed in our study. The principal orientation of the power spectrum is determined by the eigenvector of $\overrightarrow{T}$ (or $\overrightarrow{\overrightarrow{T}}$) corresponding to its largest eigenvalue. In order to validate the experimental findings, this Chapter will adopt superquadric particles (Barr 1981) in DEM modelling of granular mixers filled with either 3 mm glass beads, ellipsoids similar to jasmine rice or ellipsoids akin to barley, as it balances shape versatility and computational demands.

### 5.2.2 Simulating elongated particle

This model expands the geometry of ellipsoids by adding blockiness parameters, enabling the representation of ellipsoids using a single mathematical formula. This model defines the geometry of particles with five shape parameters as

$$f(\overrightarrow{x}) \equiv \left(\left|\frac{x}{a}\right|^{n_2} + \left|\frac{y}{b}\right|^{n_2}\right)^{n_1/n_2} + \left|\frac{z}{c}\right|^{n_1} - 1 = 0, \tag{5.5}$$

where $\overrightarrow{x} = (x, y, z)^T$ and $a, b, c$ are the half-lengths of the particles along its principal axes, and $n_1$ and $n_2$ are blockiness parameters. Using these five parameters, the three different types of particles can be modelled as ellipsoids. Figure 5.5 illustrates the projected X-ray intensity of such particles using the forward projection method.

The information regarding the orientation of particles data can be tracked using quaternions (Hamilton 1844) as

$$\overrightarrow{q} = (q_0, q_1, q_2, q_3)^T. \tag{5.6}$$

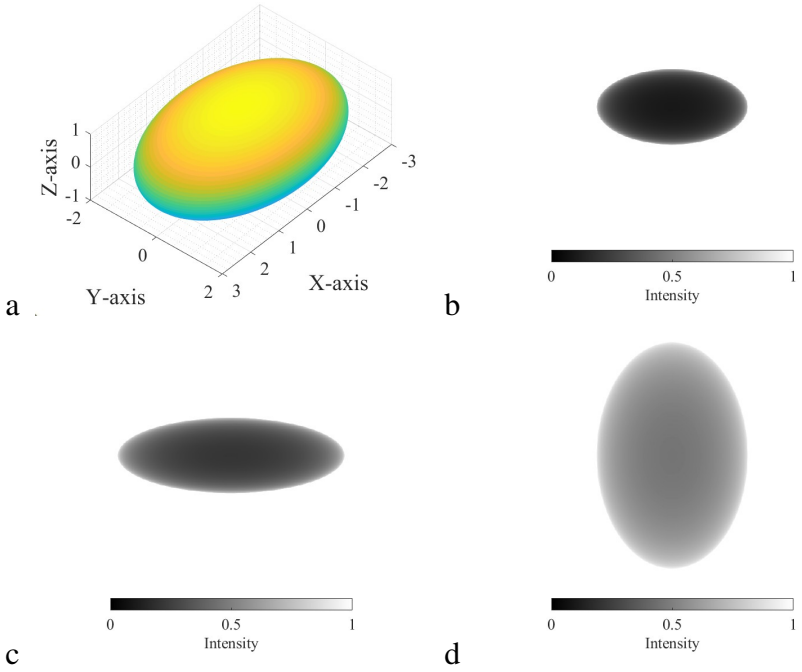


FIGURE 5.5: Ellipsoid projection ($a$ = 3, $b$ = 2, $c$ = 1; $n_1 = n_2 = 2$) with attenuation coefficient, $\mu = 0.005$: a) 3D view, b) normal to X-axis, c) normal to Y-axis, d) normal to Z-axis.

These four quaternions in the above vector vary as the angle of rotation of the superquadric particles around the axis changes. By tracking the quaternions and using them to construct the rotational matrix, one can represent superquadric particles in space using the rotation matrix ($A$) as

$$A = \begin{pmatrix} 1-2(q_2^2+q_3^2) & 2(q_1q_2-q_0q_3) & 2(q_1q_3+q_0q_2) \\ 2(q_1q_2+q_0q_3) & 1-2(q_1^2+q_3^2) & 2(q_2q_3-q_0q_1) \\ 2(q_1q_3-q_0q_2) & 2(q_2q_3+q_0q_1) & 1-2(q_1^2+q_2^2) \end{pmatrix}. \tag{5.7}$$

A typical representation of the superquadric particle (in Figure 5.5), is shown following a controlled rotation about the X-axis in Figure 5.6.

To simulate the mixing of non-spherical particles, we used the open-source DEM software LIGGGHTS (Podlozhnyuk et al. 2017). Non-spherical grains were modelled using the superquadric method (Barr 1981), which provides smooth and continuous particle surfaces while maintaining computational efficiency. This technique was chosen because it allows for precise

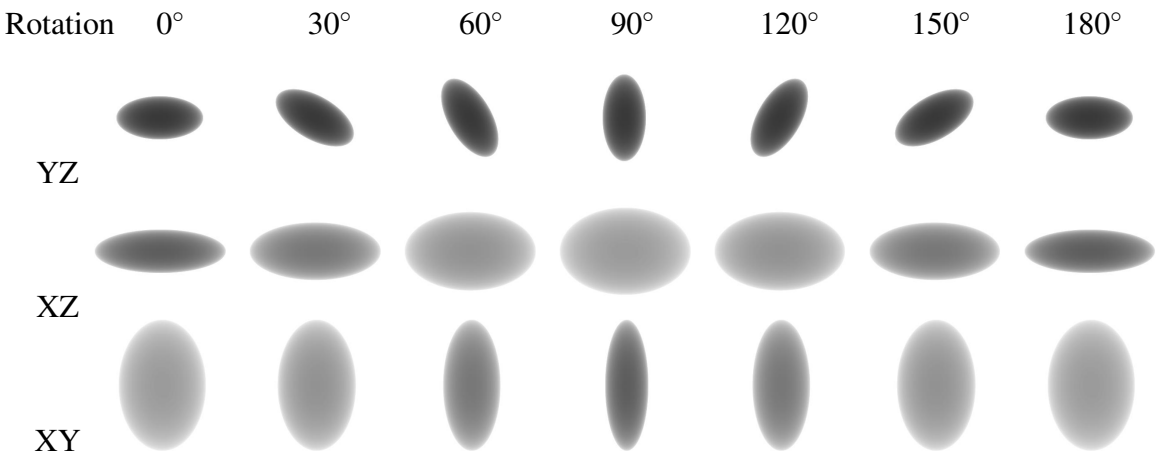


FIGURE 5.6: Ellipsoid projection ($a = 3$, $b = 2$, $c = 1$; $n1 = n2 = 2$) along the normal to X-axis, Y-axis, and Z-axis. (from Figure 5.5), with rotation about the X-axis.

control over particle geometry through shape parameters, enabling us to better represent the experimental grains without relying on faceted or clumped-sphere approximations.

In terms of computational performance observed, simulating a superquadric sphere required roughly five times more CPU time than simulating a simple spherical particle under the same mixing conditions. For non-spherical shapes, direct comparisons of computational costs are more complex; however, among the particle types studied, jasmine rice grains had the longest simulation times. It is also important to note that the number of particles varied across simulations to ensure equal total volumes. Despite the additional computational burden, the superquadric approach struck a balance between accuracy and efficiency, allowing us to capture key shape effects in the mixing process. Figure 5.7 illustrates the grain shapes of the materials used to represent the experimental materials.

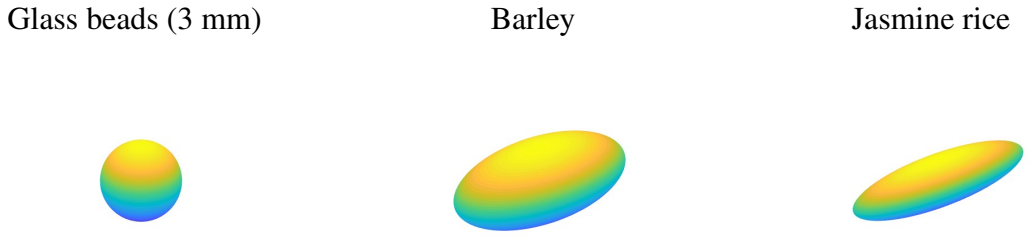


FIGURE 5.7: Shapes of grains used in the simulation

Using the forward projection method, these discrete positions and quaternions facilitate the generation of simulated radiographs (see Figure 5.8), from which the orientation fields can be obtained and compared with the experimental results for the alignment of the fabric in depth-projected scenarios. Once validated against the experiment, this discrete information from DEM further allows for a more reliable examination of the fabric alignment in 3D.

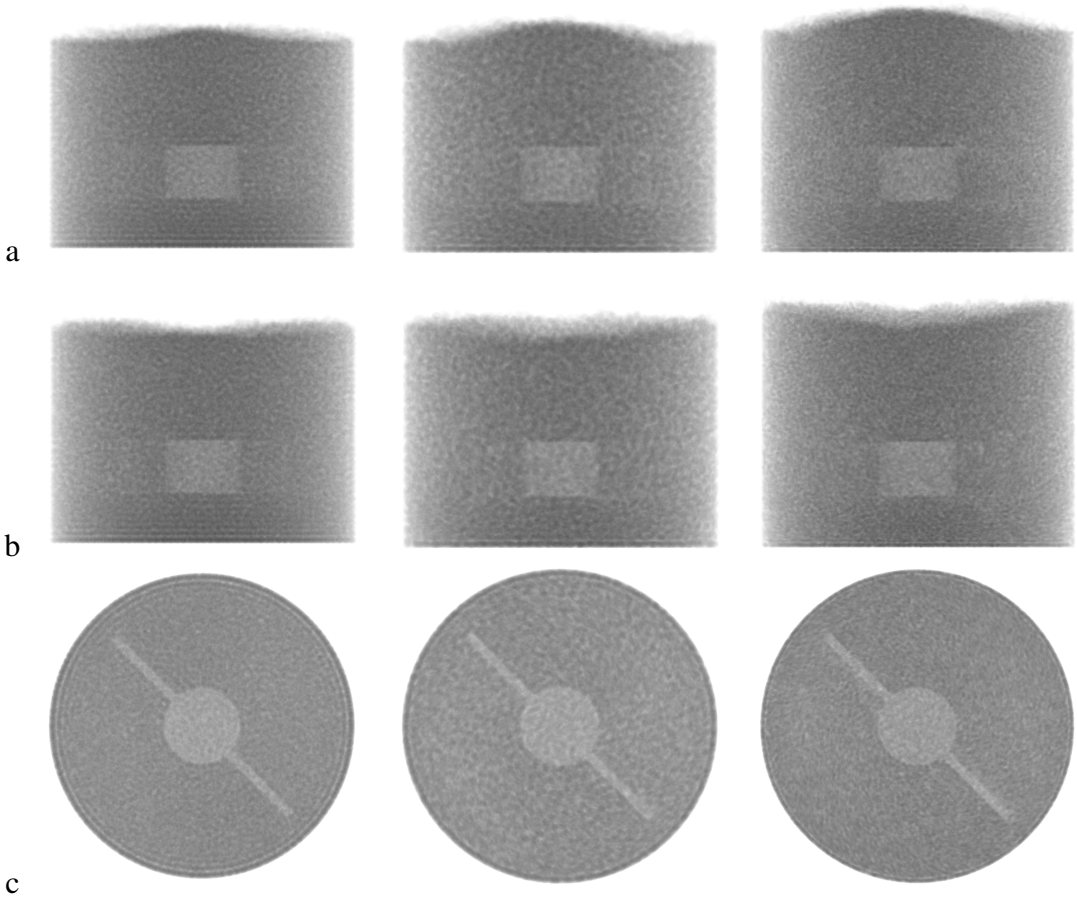


FIGURE 5.8: DEM simulated radiographs of 3 mm spherical glass beads, barley, and jasmine rice used in the study show three orthogonal viewing directions: a) normal to X-axis, b) normal to Y-axis, and c) normal to Z-axis.

## 5.3 Results and Discussion

In Figures 5.9 a and 5.10 a, with a 145° blade angle, streamlines for jasmine rice, barley, and glass beads resemble each other. However, at a 90° angle, with shearing direction changes,

jasmine rice (Figures 5.9 b and 5.10 c) shows different velocity streamlines due to the change in the angle of the blade, unlike glass beads, which remain nearly the same.

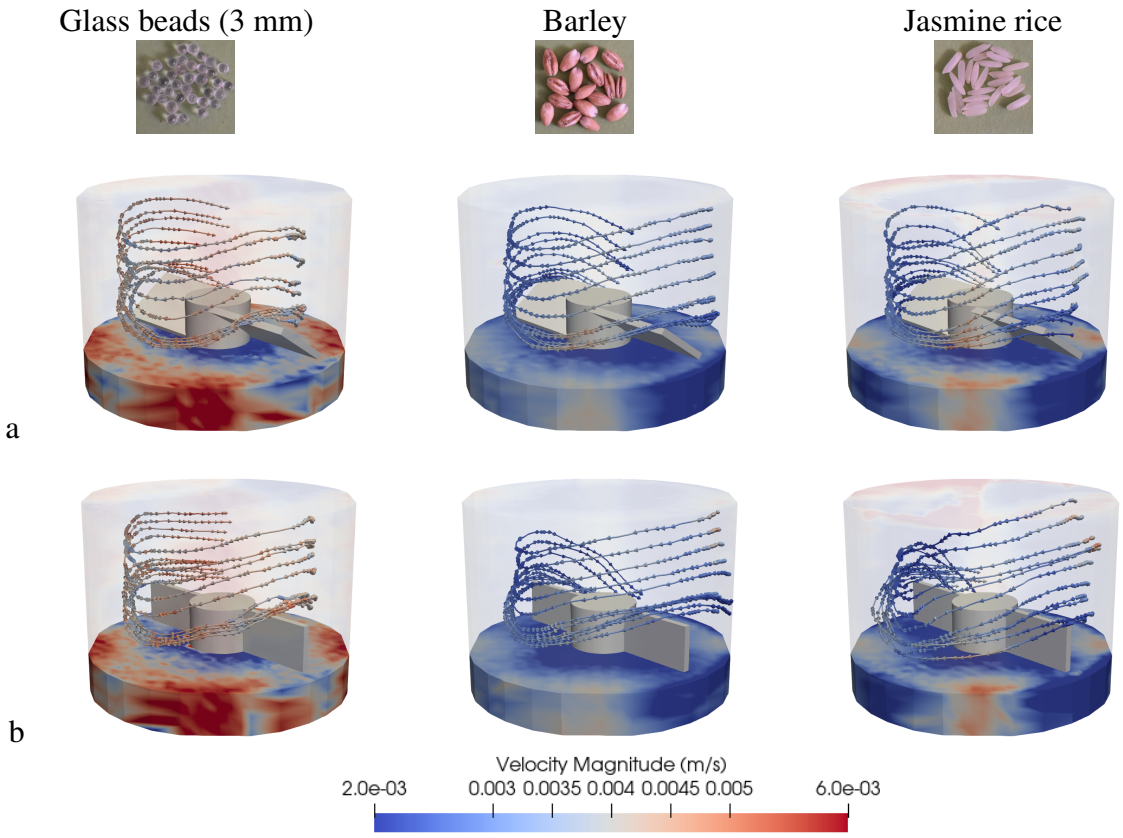


FIGURE 5.9: Rheographic velocities streamlines around a blade with a cross-section of the 3D contour of the velocity magnitude $|\mathbf{u}| = \sqrt{u^2 + v^2 + w^2}$ below the bottom level of the blade: a) blade angle = 145°; and b) blade angle = 90°.

An intermediate 117.5° angle blade in DEM (Figure 5.10 b) further demonstrates an intermediate effect between the two other blades on the jasmine rice mixer. Barley, which has an intermediate aspect ratio between jasmine rice and glass beads, shows an intermediate impact on variations in flow behaviour. In particular, the angle of the blade affects the flow of elongated grains because of their anisotropic nature, which changes due to the interactions with the blade. These findings require detailed quantitative studies to explore the impacts of shape and blade angle on granular mixing by analysing the axial and tangential velocity distributions under varying geometries.

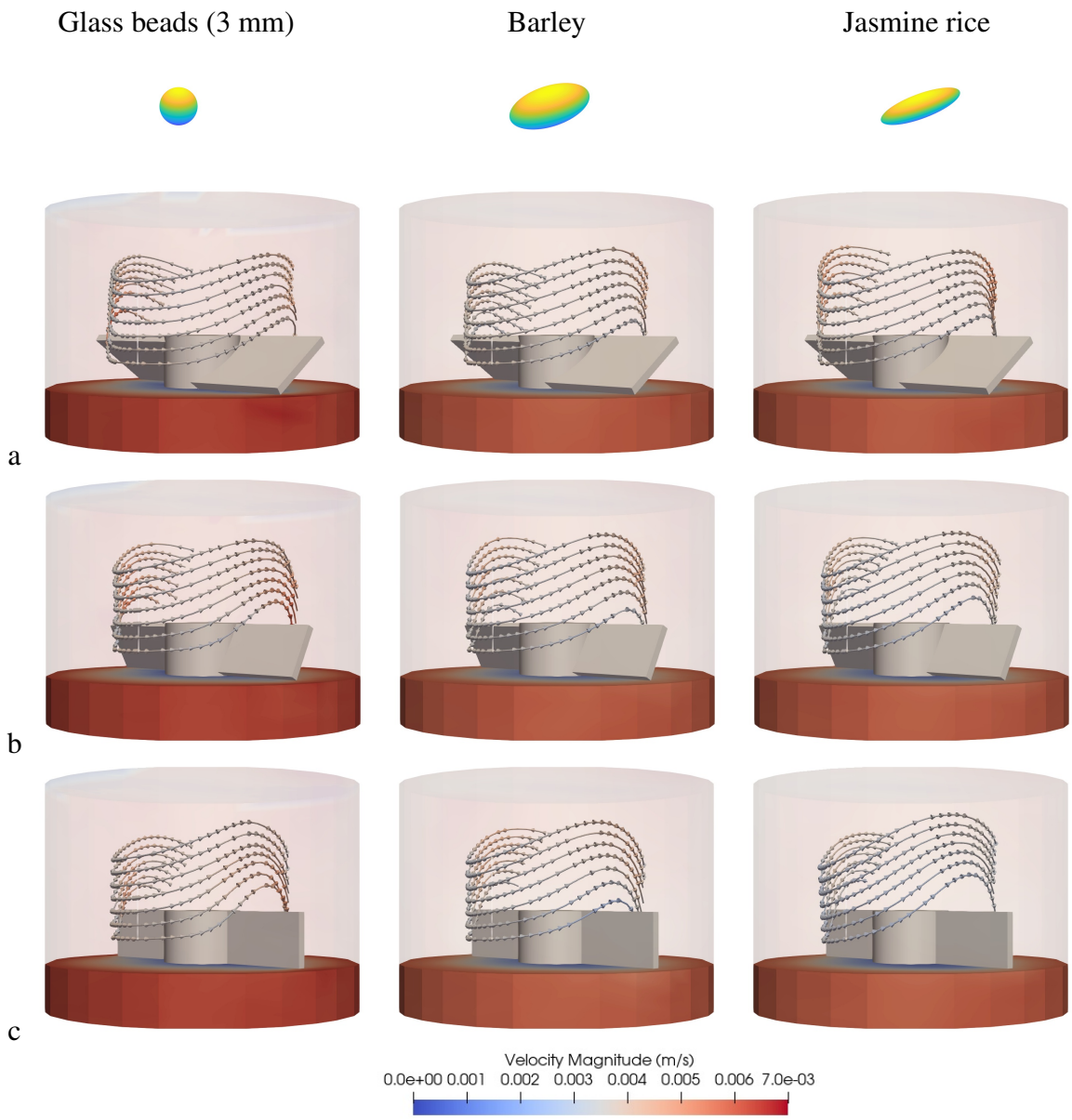


FIGURE 5.10: DEM velocity streamlines around a blade with a cross-section of the 3D contour of the velocity magnitude $|\mathbf{u}| = \sqrt{u^2 + v^2 + w^2}$ below the bottom level of the blade: a) blade angle = 145°; b) blade angle = 117.5°; and c) blade angle = 90°.

### 5.3.1 Axial velocity

The axial velocity fields obtained by the rheographic method in the experiments (see Figure 5.11) reveal that jasmine rice, barley, and glass beads exhibit comparable axial velocity contours in different blade geometries.

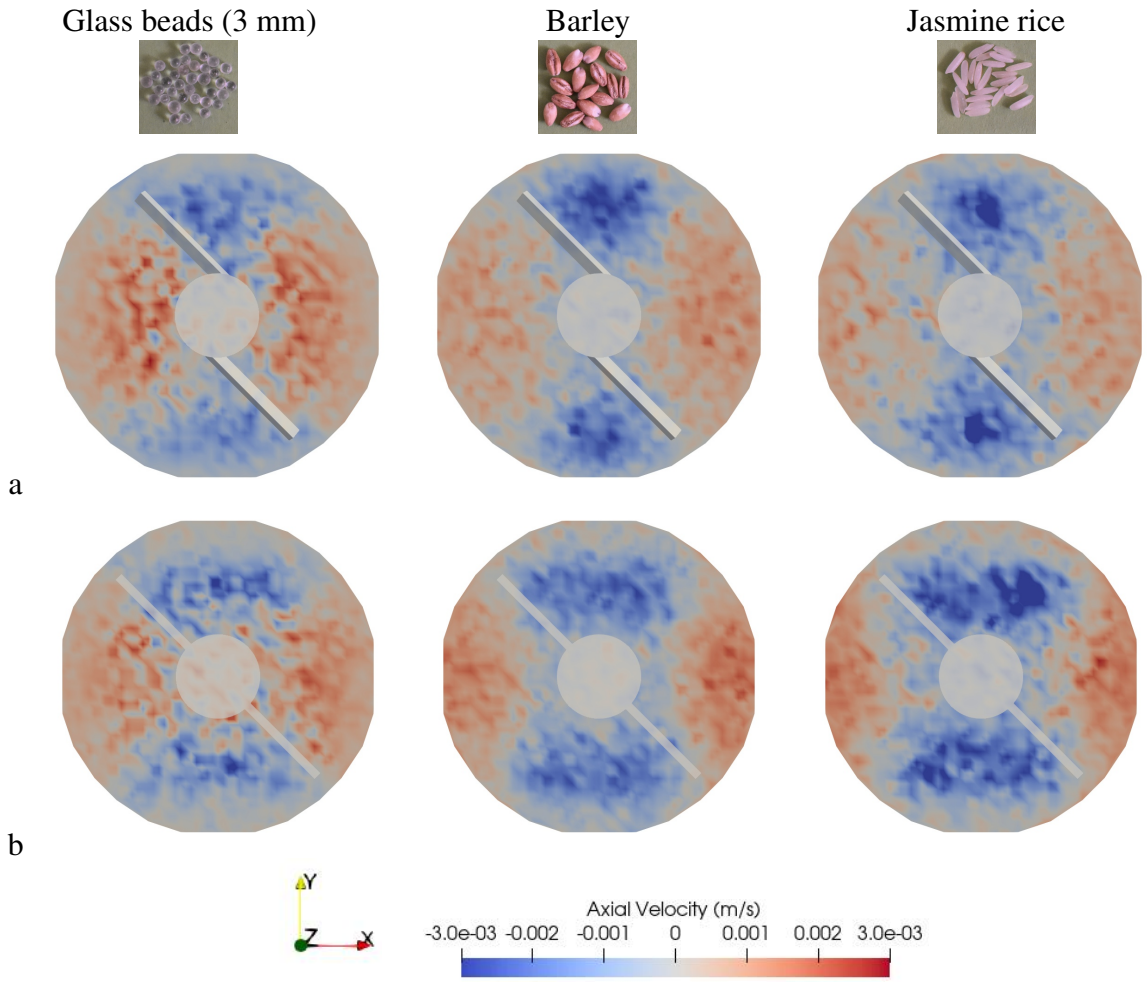


FIGURE 5.11: Rheographic results showing axial velocity contours at the top level of the impeller blade from experimental mixing various particle shapes with blade angles: a) 145°; b) 90°.

The flow pattern, affected by the impeller blade, causes particles near the blade to move upward (red regions) and those behind it to move downward (blue areas). In contrast to spherical glass beads, elongated particles such as jasmine rice and barley show discernible variations in axial velocity contours between vertical and inclined blade setups. This is quantitatively confirmed through statistical analysis (Figure 5.12).

First, statistical analysis reveals that the mean axial velocity values for all types of particles remain close to zero. This indicates that on average, the upward and downward motions balance out. Second, the analysis shows that the variability around this mean, captured by the standard deviation, differs depending on the particle's shape and the blade's angle. Specifically, jasmine rice (see Figures 5.12 e and f) shows a 31% higher standard deviation in axial velocities when

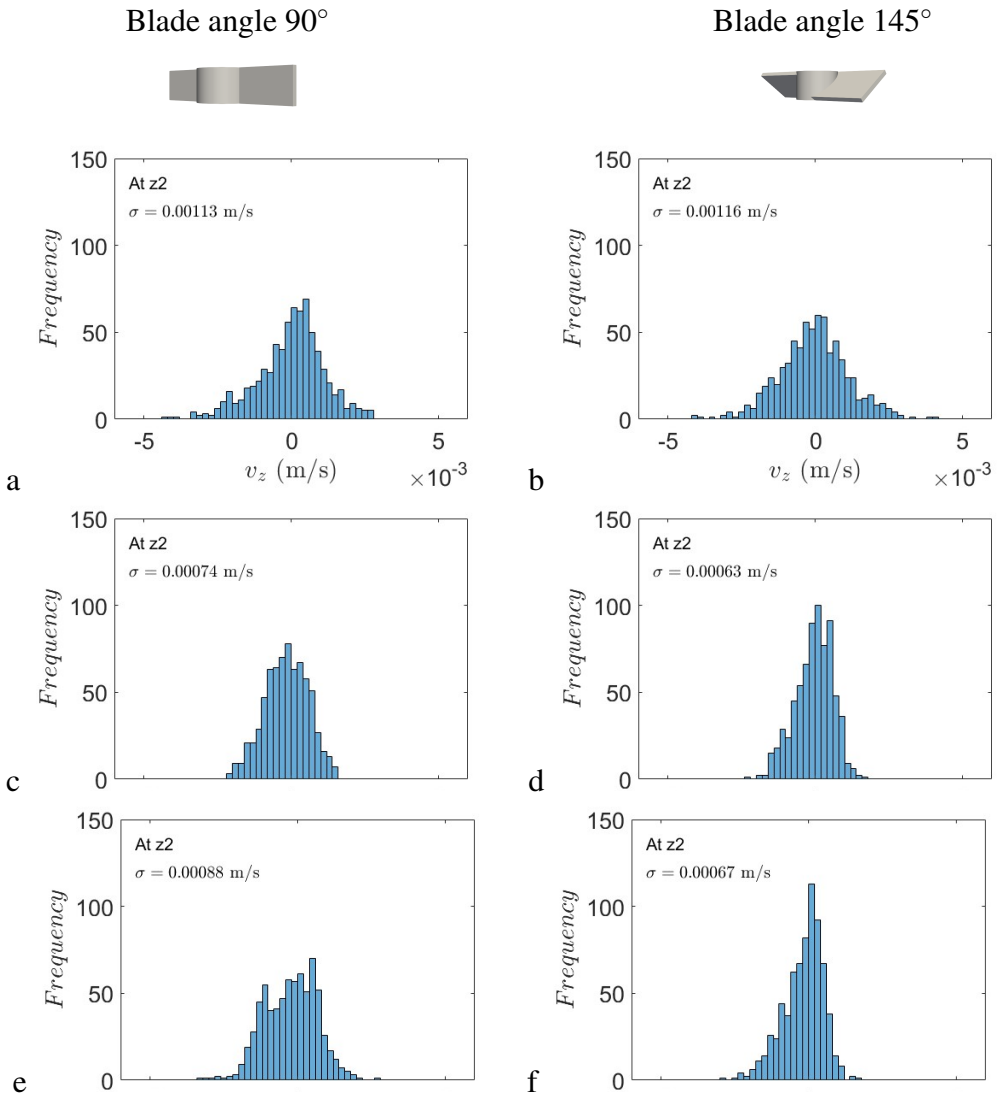


FIGURE 5.12: Histograms of axial velocities demonstrate the impact of the impeller blade angle on particle shape obtained through experimental rheography while mixing different materials: a,b) glass beads; c,d) barley; and e,f) jasmine rice. The notation $z2$ (refer to Figure 5.11) represents the top level of the impeller, as discussed in Chapter 4. At this height, the blade angle has the maximum effect.

using a vertical blade than an inclined one, while barley (see Figures 5.12 c and d) shows a 17% increase under the same conditions. These elevated standard deviations suggest that the fluctuations in axial velocity representing the extent of rising and falling motion are more pronounced in vertical blade configurations. In contrast, spherical particles (see Figures 5.12 a and b) show minimal variation, with only a 2% difference in standard deviation between

blade orientations. This indicates that the blade's angle influences the elongated grains' mixing dynamics but has little effect on the spherical grains.

### 5.3.2 Tangential velocity

To further clarify the role of the shape of the particles and the angle of the blade in influencing the variations in circular flow, the tangential velocity, normalised by the maximum rigid body motion, was plotted as a function of the radial distance (Figure 5.13).

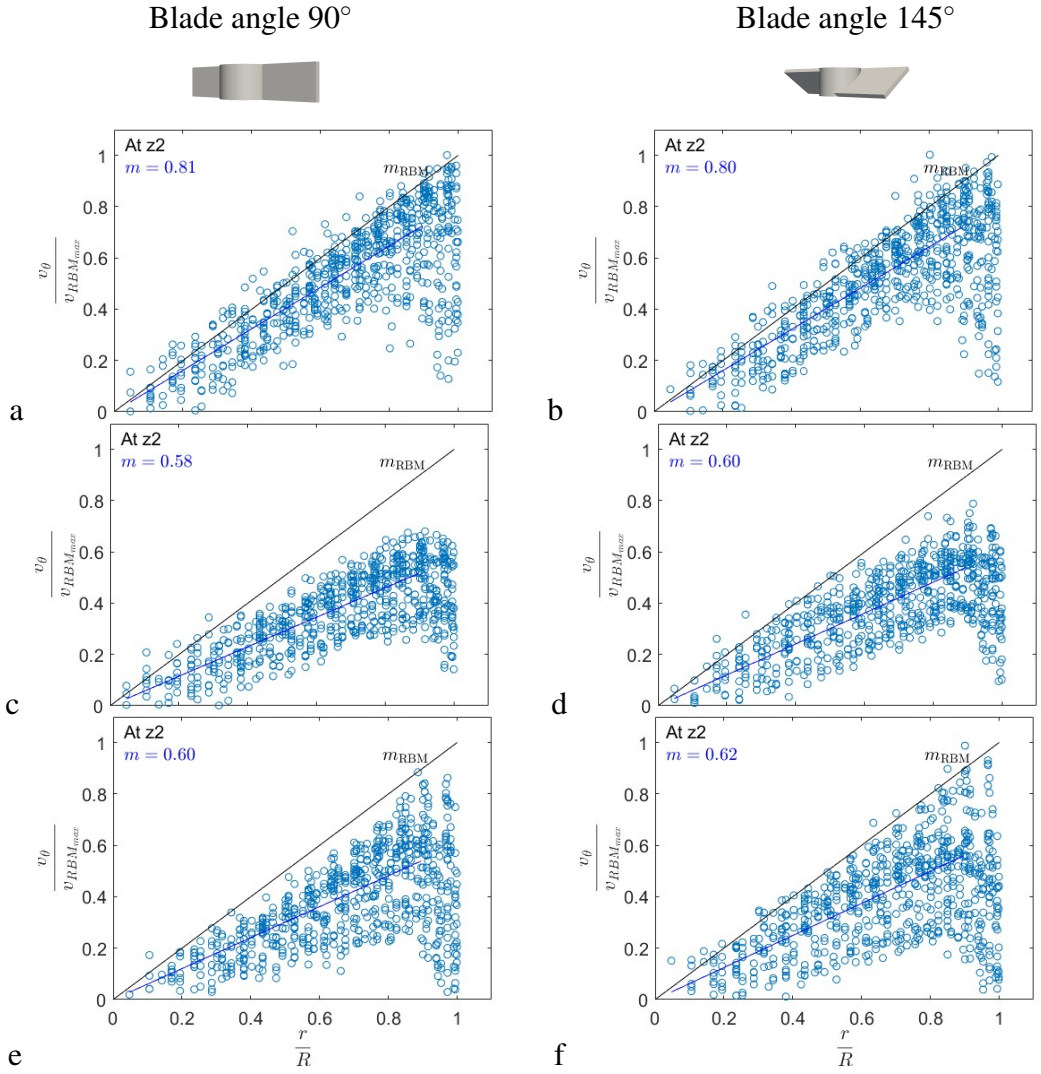


FIGURE 5.13: Normalised tangential velocity illustrates impeller blade angle effects obtained using the experimental rheography while mixing a,b) glass beads, c,d) barley, and e,f) jasmine rice. Here, $m$ is the slope of the best-fit line, $m_{RBM}$ is the slope of Rigid Body Motion (RBM) velocity, and $r/R$ is the normalised radius (with $r$ as radial distance and $R$ as the mixer radius).

This quantitative analysis assesses the impact of the impeller blade's angle by examining the best-fit lines representing the normalised tangential velocity distributions across the mixer radius. The best-fit lines are positioned below the rigid body motion reference lines in all the analysed cases. A comparison of the slopes reveals that for jasmine rice (see Figures 5.13 e and f), the best-fit line exhibits a slope of 0.62 for inclined blades and 0.60 for vertical blades. For barley (see Figures 5.13 c and d), the corresponding slopes are 0.60 and 0.58, respectively. The slopes for 3 mm glass beads (see Figures 5.13 a and b) are 0.80 for inclined blades and 0.81 for vertical blades. Specifically, for elongated particles such as jasmine rice and barley, the slope of the best-fit line is approximately 2-3% higher for inclined blades than vertical ones. This suggests that while the change is minimal, it does affect the tangential velocity for these types of particles compared to spherical particles.

This trend is further reinforced by an in-depth analysis of velocity variations along different heights within the mixer, as shown in Figure 5.14. These quantitative results indicate that the effect of the blade angle is more pronounced for elongated grains (see Figures 5.14 b and c) due to their directional alignment and anisotropic flow characteristics.

At the same time, spherical particles (see Figure 5.14 a), which lack preferential orientation, remain largely unaffected by the blade's angle. Quantitative analysis of velocity results provides evidence that the shape of the particles is potentially important in determining the flow response to blade configurations. This difference comes from the inherent directional characteristics of elongated particles (Nadler et al. 2018), which uniquely interact with the boundaries and the granular environment due to their orientation-dependent friction and resistance to rotation. Experimental and simulated radiographs (see Figures 5.4 and 5.8) reinforce this finding, indicating that jasmine rice and barley align along their major axis during mixing. The upcoming section also presents a detailed fabric orientation analysis to justify this initial observation.

### 5.3.3 Fabric analysis in 2D

As discussed in the subsection 5.2.1 section, the principal orientation of the fabric from the X-ray radiographs can be derived from density fluctuations using the Fourier transform technique. This method allows for the identification of the dominant orientation in the spatial arrangement

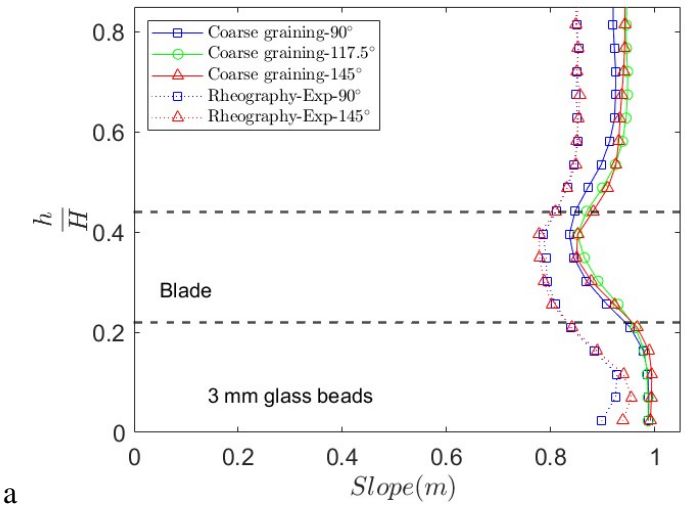


a

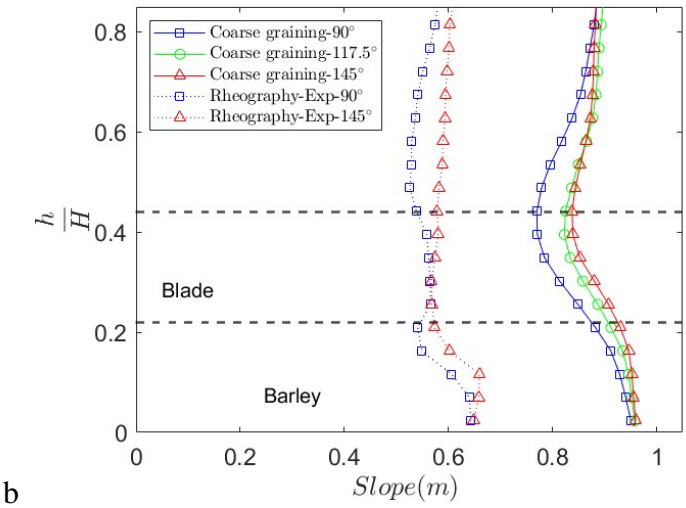


b

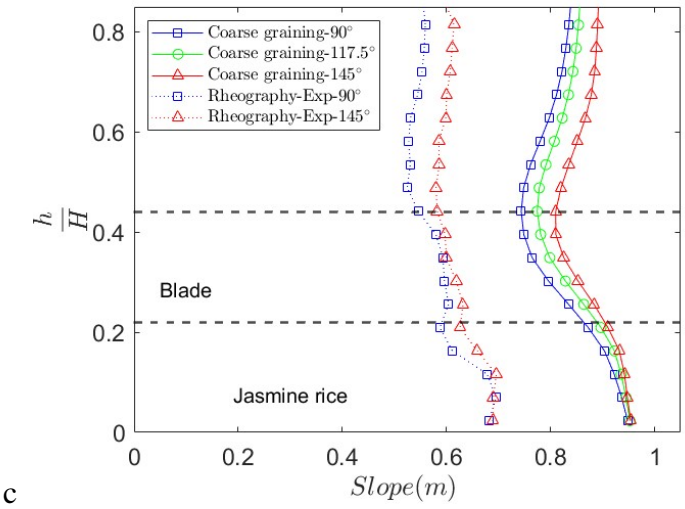


c

FIGURE 5.14: Fitted slope from Figure 5.13 along the height of mixer obtained from experiments and similar analysis from coarsed grained DEM velocity fields to compare the effects of particle shape on mixing with various impeller blade angles: a) spherical 3 mm glass beads; b) elongated barley; and c) elongated jasmine rice

of the particles, which reflects their preferred alignment. Figure 5.15 illustrates the principal particle orientation for three different materials, with the blade angle set at 90°, a condition where greater variations in velocity measurements were observed.

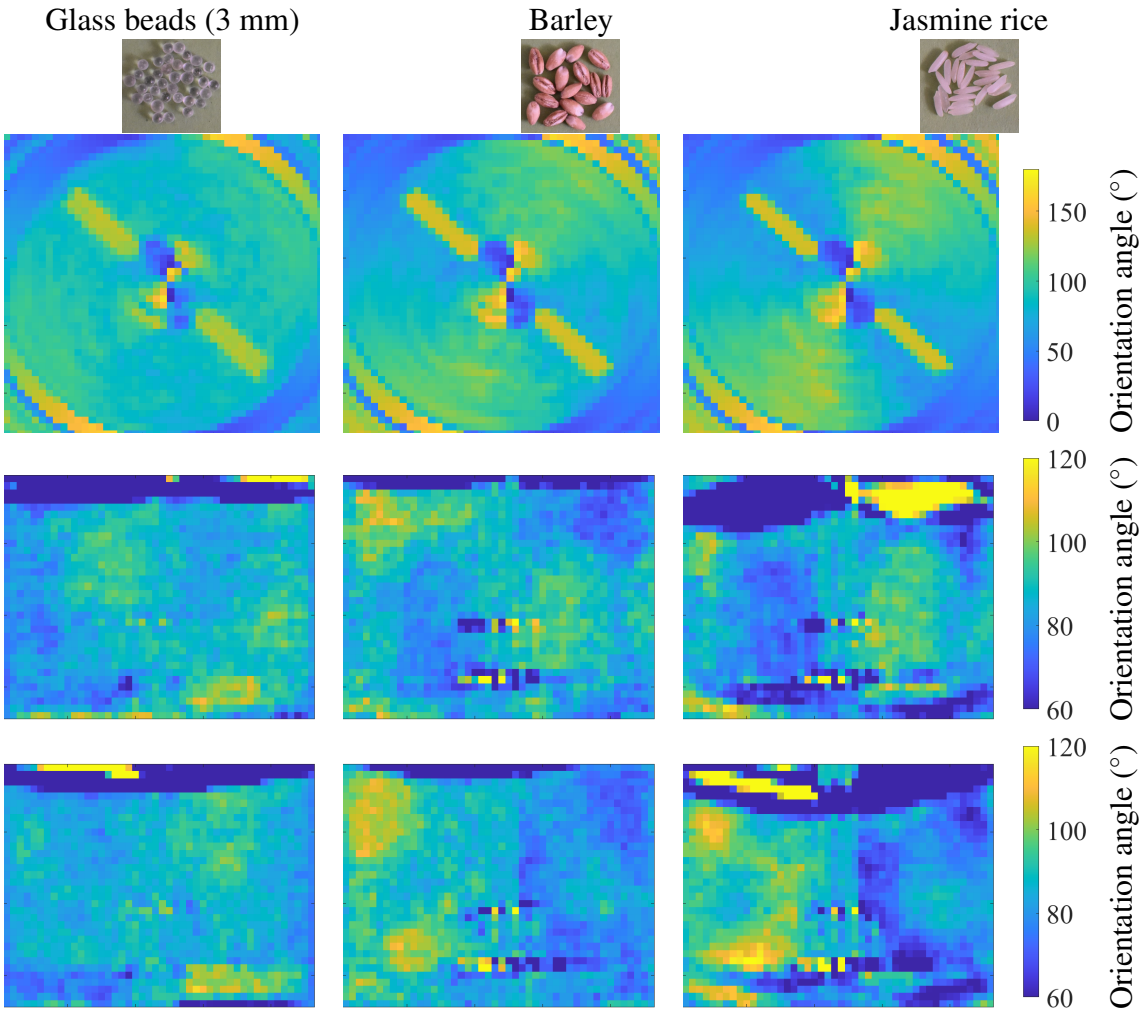


FIGURE 5.15: Depth averaged principal orientation angle fields of the particles in the experiments

A distinct preferred orientation is evident in the top-down view of jasmine rice, which contains the most elongated particles among the materials analysed. The particles show a well-defined alignment with four distinct regions (two blue and two yellow zones), suggesting that the principal fabric orientation of the particles varies depending on their proximity to the blade. This highlights the shift in fabric orientation as jasmine rice particles flow, providing evidence for a well-defined principal orientation angle throughout the bulk. In contrast, the results

with the glass beads do not exhibit any significant principal orientation during flow. This is anticipated because glass beads, being spherical, are isotropic and lack any inherent directional preference. As a result, the fabric orientation of this material remains largely unstructured, with no dominant alignment angle emerging during the flow. Barley show intermediate levels of preferred orientation, suggesting that, while some alignment occurs, it is not as evident as that in jasmine rice. This observation is consistent with the characteristics of barley, where the particles are elongated but to a lesser extent than jasmine rice, leading to a more subtle effect on the overall orientation of the fabric. These findings are supported by the fabric orientation analysis illustrated in Figure 5.16, which used simulated radiographs (from Figure 5.8).

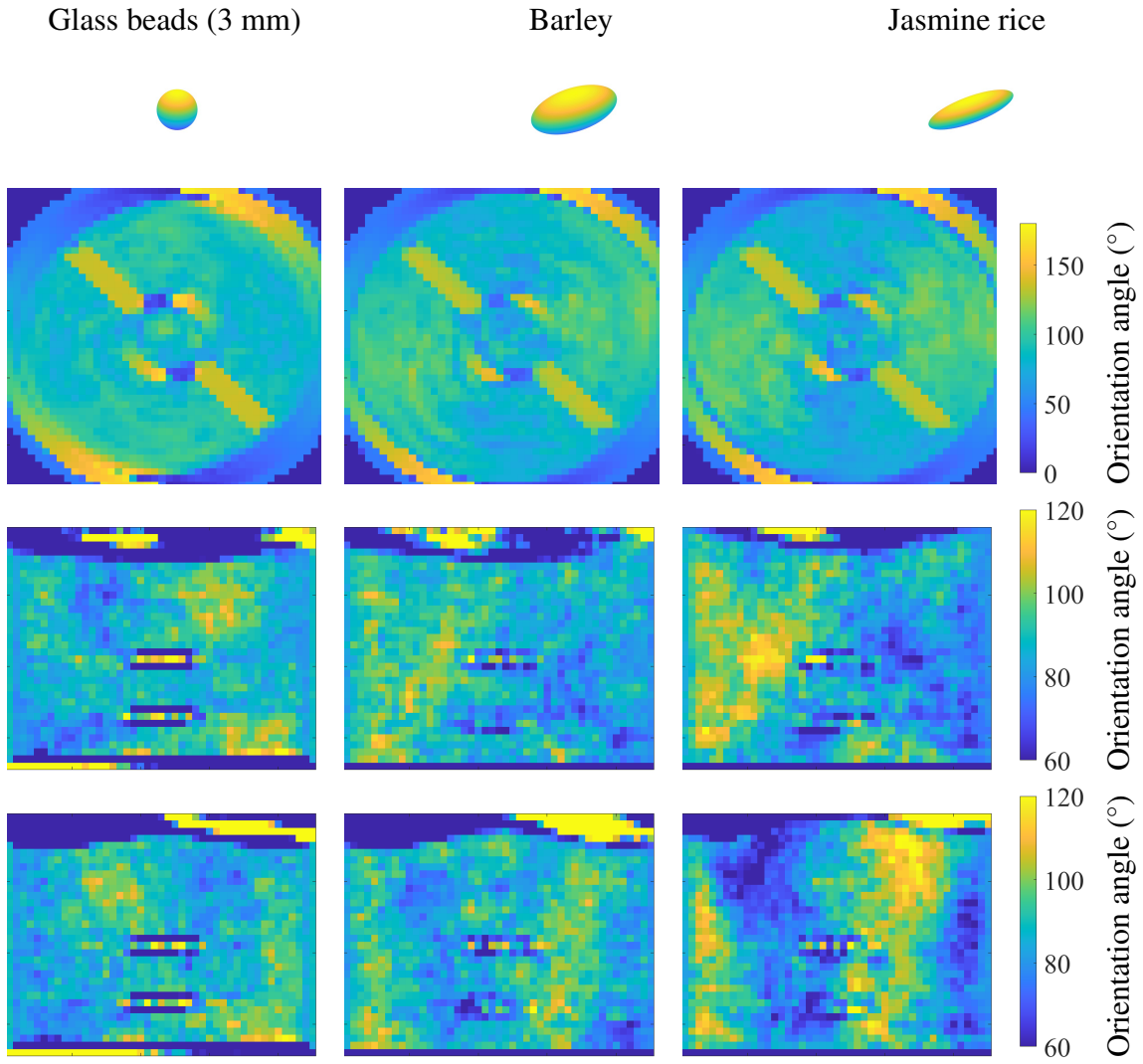


FIGURE 5.16: Depth averaged principal orientation angle fields of the particles in the simulation

The two side views of the materials further provide insight into the principal orientation of the particles. Elongated particles such as jasmine rice and barley continue to exhibit a clear preference for alignment. However, analysis using both the simulated and experimental X-ray radiographs reveals patches of apparent preferred orientation in the side views, particularly for the glass beads. These patches should not be interpreted as genuine alignment but rather as artefacts induced by the X-ray measurement process. To better understand these artefacts, we examine the ordering parameter, denoted as $\|\overrightarrow{T}\|$, which quantifies the degree of alignment of the particles. The ordering parameter ranges from 0 (completely random) to 1 (perfect alignment). As anticipated, glass beads exhibit a lower ordering parameter than elongated particles such as jasmine rice and barley (see Figure 5.17).

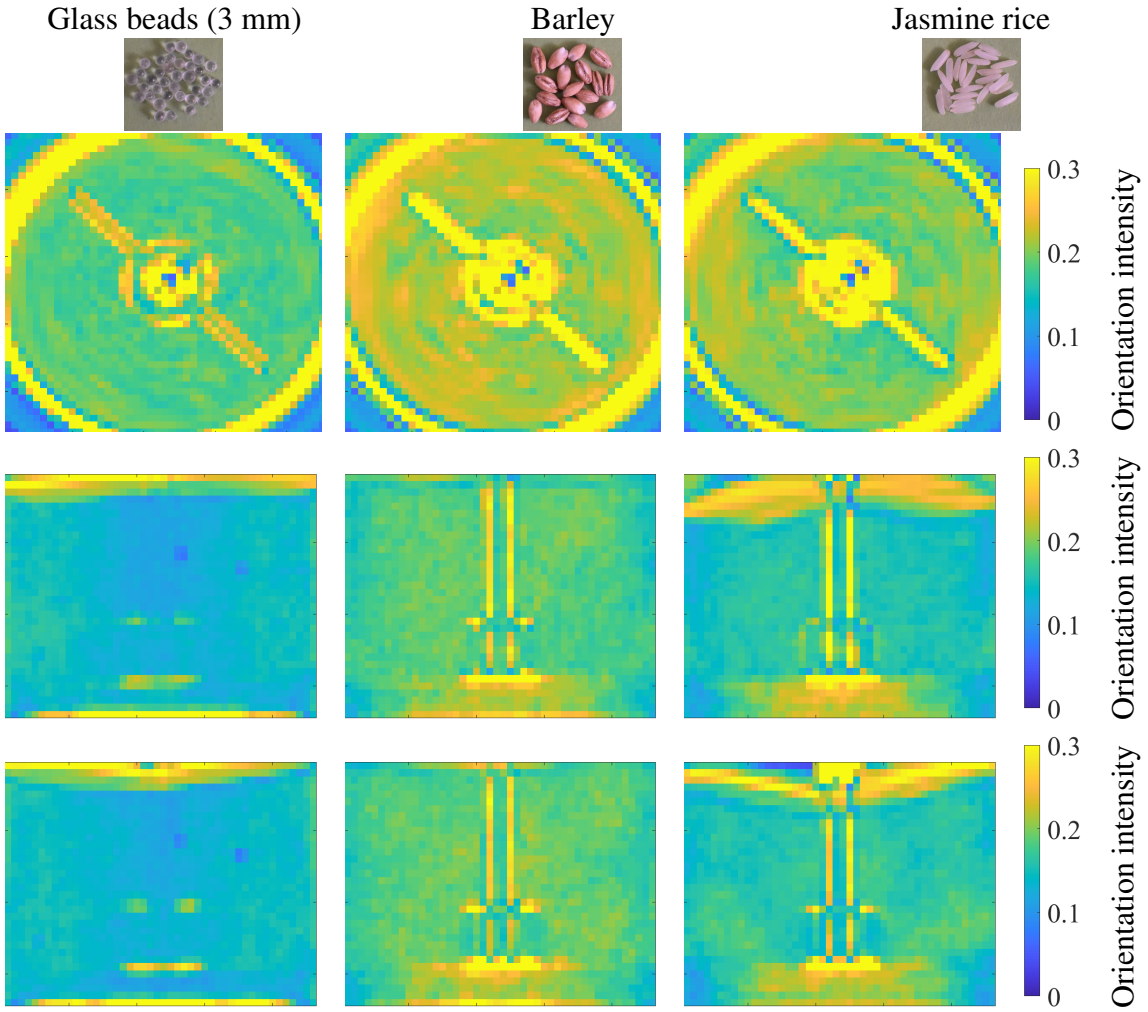


FIGURE 5.17: Depth averaged orientation intensity fields (for Figure 5.15) in the experiments

In an ideal scenario, the ordering parameter for the glass beads would be close to zero, indicating no preferential alignment. However, some variation is observed because of noise and other factors, such as velocity trails and pixel alignment in the detector. These findings align with the $\|\overrightarrow{T}\|$ values derived from the simulated radiographs in Figure 5.18. The two dark blue patches in the results $\|\overrightarrow{T}\|$ for glass beads (Figure 5.17) can also be attributed to such artefacts, as the simulated results do not show these patches (see Figure 5.18).

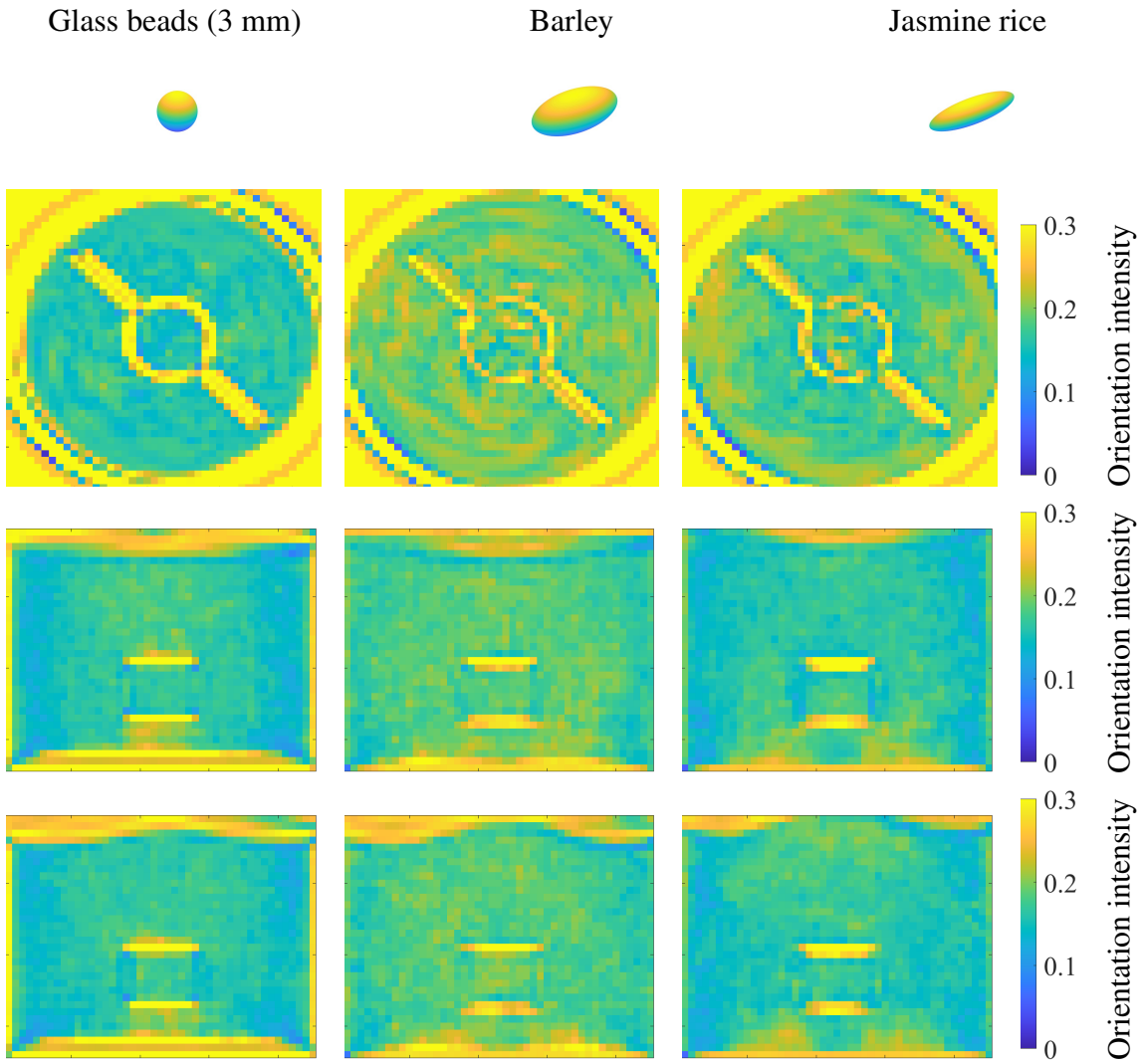


FIGURE 5.18: Depth averaged orientation intensity fields (for Figure 5.16) in the DEM simulations

This suggests that the orientation angle patches shown in the orientation angle plots (see Figures 5.15 and 5.16) do not accurately reflect the alignment of the particles in the case of glass beads. Moreover, the X-ray scattering process generates an intensity gradient across

the image, which can be misinterpreted as a preferred orientation. These findings support the hypothesis formed during the observation of radiographs for elongated particles, where strong alignment along the major axis is expected during flow. This supports the hypothesis that elongated particles align more consistently during flow. Interestingly, the results suggest that barley has a stronger order (higher $\|\overrightarrow{T}\|$) than jasmine rice, which may be associated with its oblate rather than prolate shape.

### 5.3.4 Fabric analysis in 3D

After cross-validating our DEM model with experimental data on fabric alignment in the depth-projected scenario, we used all the potential of the DEM information to reconstruct the entire three-dimensional (3D) fabric alignment field, as shown in Figure 5.19.

This reconstruction overcomes the inherent limitation of X-ray studies, which only provide depth-averaged insights into particle alignment. By applying a coarse graining technique to the discrete particle orientation data, we could determine particle alignment relative to the horizontal bed of the mixer (see Figure 5.19 a). This approach enabled us to conduct a more detailed analysis across different observation planes, revealing distinctive alignment patterns for elongated and spherical particles. For example, in Figure 5.19 b, we observed a preferential alignment in elongated particles, while spherical particles showed a random distribution in line with expectations. To further validate these findings, we examined cross-sectional views in two additional planes (see Figures 5.19 c and d), which provided deeper insights into how shear forces due to the blade impact particle orientation at various heights within the mixer, especially regarding particle shape. In particular, elongated particles showed significant alignment above the blade, whereas those near the bottom of the mixer followed a circular motion due to lower shear effects. These observations are consistent with the fact that the major axis of elongated particles aligns almost horizontally with the flow direction in regions that exhibit circular motion. Above the blade, the particles align more closely with the induced shear flow direction, confirming that the major axes of the elongated particles orient themselves with the flow direction (Nadler et al. 2018). This alignment shift highlights the critical role of particle shape in determining granular mixing kinematics, offering valuable insights to optimise mixing

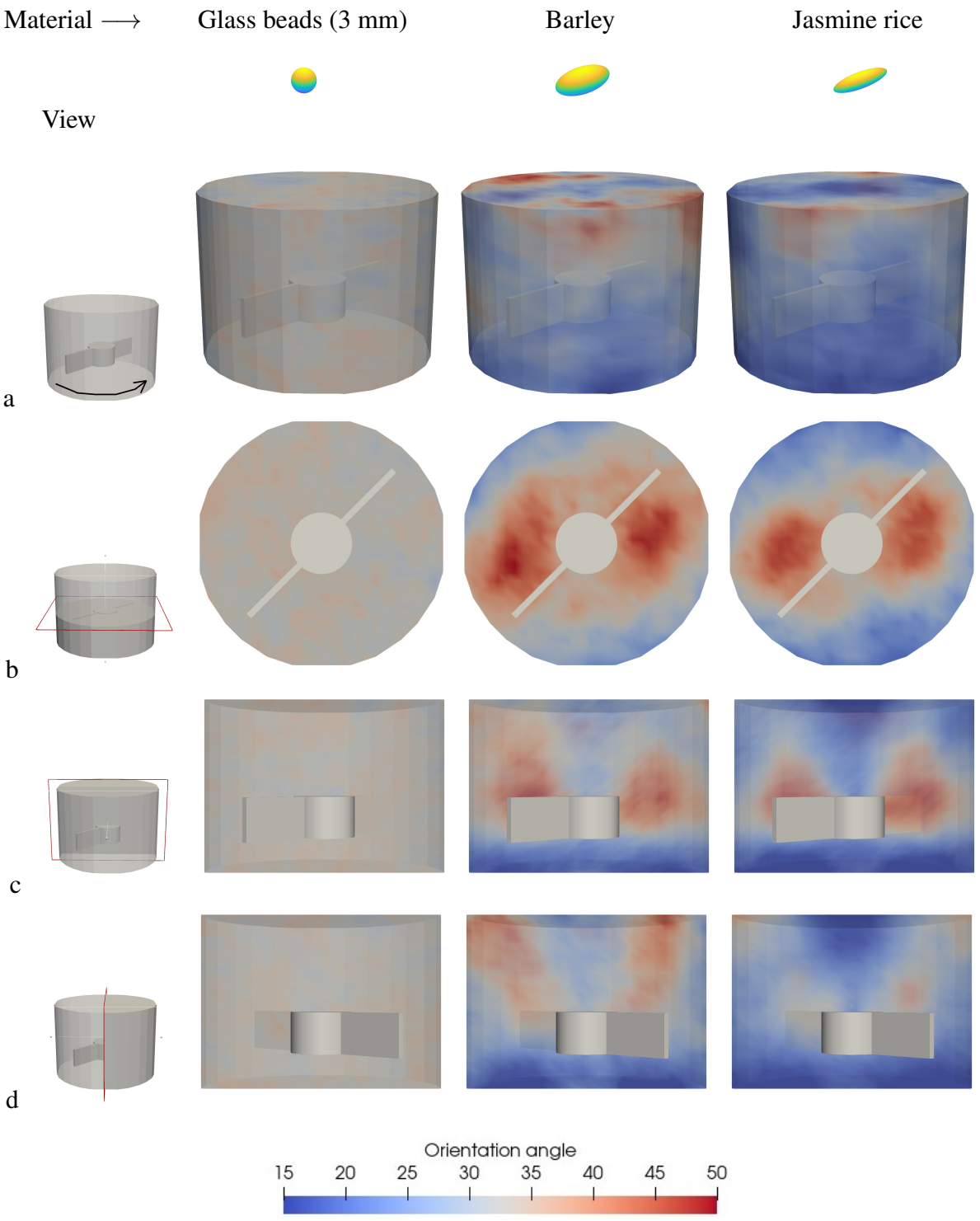


FIGURE 5.19: Plot showing fabric alignment for jasmine rice, barley, and glass beads using DEM: (a) a transparent 3D field; and (b, c, d) cross-sections across three orthogonal planes.

processes in industries such as powder processing, pharmaceutical blending, and other granular mixing applications.

## 5.4 Summary

This chapter explores the behaviour of granular mixing by linking reconstructed velocities with fabric orientation, providing insights into the mixing behaviours of jasmine rice, barley, and spherical glass beads under varying impeller blade geometries. The velocity field analysis demonstrates that mixing elongated particles, such as jasmine rice, is affected by blade angles, resulting in distinct axial and tangential velocity variations. In contrast, spherical particles show minimal flow differences between blade configurations. Fabric analysis explains these differences because elongated particles align preferentially along their major axes, whereas spherical beads maintain an isotropic distribution with negligible orientation effects.

CHAPTER 6

# Conclusion and future outlook

Understanding granular mixing kinematics is vital in various sectors, such as pharmaceuticals, food processing, and engineering. Traditionally, researchers have predominantly used basic photography to analyse granular mixing kinematics. This technique allows for qualitative evaluation through images taken through transparent barriers or open free surfaces and uses particle image velocimetry (PIV) for quantitative assessments of particle motion near boundaries. Although these methods offer significant insights, they are restricted to surface or near-wall behaviour, leaving the bulk mixing's internal dynamics largely unexamined. The inherently opaque nature of granular substances presents a considerable obstacle which impedes direct observation of particle movements within the bulk. Moreover, numerous other experimental methodologies within this domain frequently disrupt the inherent mixing dynamics of the granular system due to the employment of invasive agents such as index matched fluids.

The discrete element method (DEM) has become the most widely used theoretical approach to studying granular mixing. DEM facilitates the examination of the movement and interactions of individual particles, offering detailed insight into mixing dynamics. Nevertheless, due to computational limitations, most DEM research is limited to spherical particles because of their simpler mathematical representation. This simplification does not accurately reflect the wide range of particle shapes in practical applications, where shape significantly influences mixing dynamics. DEM simulations address this by approximating nonspherical particles with overlapping or bonded spheres, a method that, while useful, does not entirely capture the intricate contact mechanics and interactions of nonspherical particles. Moreover, since DEM models yield numerical predictions, experimental validation is crucial to confirm their precision and applicability. Many studies of granular mixing neglect this vital validation step, reducing the reliability of their conclusions. These experimental and computational challenges highlight the need for more sophisticated techniques.

Our study tackles these issues by utilising novel experimental techniques. We used non-invasive X-ray imaging to delve into the internal dynamics of granular mixing, going beyond the limits of traditional surface observations confined to transparent boundaries. This method allows for tracking of particle movements throughout the system without interrupting natural mixing. For our study, we designed a granular mixer to examine the three-dimensional (3D) velocities involved in granular mixing. Past studies have largely concentrated on two-dimensional (2D) observations, which do not adequately capture the complexity of bulk dynamic processes. To address this limitation, we incorporated X-ray rheography, an advanced imaging method, into our research. This technique employs high-speed X-ray radiography from three angles to reconstruct a 3D velocity field using the image analysis method of rheography techniques. This approach offers a more thorough analysis of 3D mixing kinematics within the bulk, surpassing the capabilities of conventional imaging methods.

The precision of our experimental methodology proved particularly sensitive when analysing antisymmetric flow scenarios involving two-blade impeller configurations. These configurations required careful consideration of the X-ray detector's positioning concerning the impeller's axis. We used a theoretical antisymmetric granular flow to produce simulated radiographs, demonstrating the essential role of X-ray alignment in visualising granular flow patterns marked by antisymmetry. Our results indicated that aligning the X-ray system with the antisymmetry axis decreased the precision of X-ray rheography under these conditions. In contrast, avoiding alignment with the antisymmetry axis improved the reconstruction of internal velocity fields, minimised antisymmetry-induced artefacts, and offered insight into antisymmetric flows. This understanding laid a fundamental experimental framework for tackling the antisymmetrical flow challenges associated with X-ray rheography in the study of granular mixing.

Following this fundamental study of the X-ray rheography method for assessing antisymmetric flow structures, we applied this technique to the analysis of mixing kinematics for spherical particles. The reliability of the methodology was cross-examined by comparing the experimental observations with numerical data from DEM simulations performed under similar mixing scenarios. The qualitative agreement between experimental outcomes and computational predictions for spherical particles underscores the effectiveness of the X-ray

method, validating its use in examining granular mixing for diverse particle shapes. As a result, our study was extended to investigate how variations in the shape of the particles and the angle of the impeller blade affect the dynamics of the granular mixing. This expansion required advanced computational models to complement the experimental insights. Thus, superquadric particles were introduced into DEM models to simulate the behaviour of nonspherical particles.

Examining 3D velocity fields is crucial, but similarly vital is understanding fabric's dynamic alignment, which reveals its orientation in the mixer, thus informing mixing kinematics. Fourier transformation was applied to radiographic images to determine the fabric orientation for different particle shapes. We observed distinct alignment behaviours by examining three types of particles: spherical glass beads, moderately elongated barley, and highly elongated jasmine rice. The jasmine rice particles exhibited a strong alignment along their principal axes, whereas the barley showed a similar alignment but to a lesser degree. As anticipated, spherical glass beads showed negligible alignment. Our study on kinematics and fabric orientation suggested that the shape of the particles and the angle of the impeller blades are critical factors that affect granular flow behaviour. We compared these findings with those obtained from DEM simulations and virtual radiographs to validate our results. The qualitative similarity between these data sets supports the reliability of both approaches. Furthermore, this cross-validation suggests that DEM simulations utilising superquadric models for elongated particles are reliable for obtaining a more comprehensive understanding of fabric orientation in three dimensions, surpassing the limitations of conventional depth-averaged perspectives that experimental methods cannot entirely capture.

This research marks a substantial progression in our understanding of granular mixing dynamics by combining experimental studies with DEM simulations. Clarifying the relationships between particle geometry, impeller blade angles, and flow kinematics offers deeper insights into how material shape affects flow behaviour. Noninvasive X-ray techniques help us understand the bulk behaviour better by allowing the observation of internal dynamics, thus surpassing the limitations imposed by surface imaging and PIV analysis due to boundary effects. Additionally, incorporating superquadric particles in DEM simulations refines how interactions between non-spherical particles are modelled, providing an enhanced depiction of granular flow mixing kinematics. These developments have wide-ranging implications for

the pharmaceutical, food processing, and geotechnical engineering industries. For example, the findings of this study could help optimise mixing processes in the pharmaceutical sector, where uniform mixing of powders is crucial to the efficacy of drug formulations. An improved understanding of mixing granular materials in food processing can improve product quality and consistency. Moreover, integrating superquadric particle modelling in DEM simulations offers a more accurate representation of particle alignment and interactions, which enhances predictive models for granular flows across various industrial applications.

## 6.1 Assumptions and limitations

This study uses established techniques such as deep velocimetry and rheography to determine the velocity from radiographic images. The precision and effectiveness of these methods are largely dependent on radiograph quality, which is influenced by parameters such as resolution, contrast, and noise. These factors affect the reliability of the derived velocity components. However, spatial limitations in our experimental setup can introduce artefacts, such as conical projection distortion, because of the restricted distance between the X-ray source and the detector. This limitation may compromise the accuracy of the velocity reconstruction.

The deep velocimetry technique is based on foundational assumptions, notably the linear relationship between projected images and velocity distributions. This relationship allows deconvolution techniques to infer velocity. However, deconvolution in velocity reconstruction presents an ill-posed inverse problem sensitive to noise. Regularisation techniques can stabilise this process, although they may introduce errors.

Additionally, our analysis assumes steady-state conditions in granular mixing, which are essential for accurate velocity assessments using sequential radiographs, as they reduce uncertainty and minimise transient effects during deconvolution. However, larger sample sizes can alter these steady-state conditions, as described in Chapter 4. Specifically, larger particle sizes, such as 6 mm grains, exhibit greater variation in their energy equilibration, making it challenging to select an appropriate sample size for the best prediction with such X-ray studies. The ideal sample size should maintain both the steady state condition and the necessary statistical variability in density fluctuations; excessively small samples can generate noise in velocity distributions because of less evident density fluctuations in radiographs. This issue is

highlighted in Chapter 4, where we discuss the difficulties in recovering velocities for 1 mm grain due to low-density fluctuations that compromise image correlation. In analyses involving smaller grains, the rheographic and numerical methods face limitations. DEM faces notable computational challenges because smaller particle sizes generate large datasets. This results in a rise in interactions that extend the duration of simulations, a typical drawback inherent to numerical simulations that rely on explicit time-step calculations.

Simulated radiographs have been used to validate experimental measurements at various stages, although with some simplifications. One simplification involves neglecting air attenuation, which, while less impactful than particle attenuation, still influences the comparison between experimental and simulated results. In addition, noticeable discrepancies often occur in the velocity data between the rheographic and coarse-graining methods, especially near the blade region. Chapter 4 provides a detailed analysis of tangential velocity fields, highlighting that the absence of the blade in the simulated radiographs creates a void where the blade should be. In contrast, the experimental radiographs are influenced by the presence of the blade during deconvolution, despite normalisation by radiographs of empty mixers. On the other hand, coarse-graining does not take the blade into account at all. This discrepancy may distort the interpretation of the velocity fields around the impeller. Another limitation of the X-ray method for fabric field orientation is that it only provides depth-projected results. In contrast, DEM simulations offer a more comprehensive view by providing detailed 3D information.

## 6.2 Future outlook

This research provides a solid foundation for advancing the study of granular mixing kinematics. However, several critical questions remain unaddressed, highlighting the need for further investigation into potential expansions, interdisciplinary connections, and practical applications. Exploring these areas will enhance our understanding and extend their utility in the scientific and industrial sectors.

A major limitation earlier was the reliance on DEM simulations. Although DEM effectively simulates dry granular mixing, it faces computational challenges in large-scale systems, particularly in modelling complex particle interactions influenced by cohesion, moisture, or clustering. Moreover, existing numerical models typically assume ideal conditions, neglecting the impact

of real-world environmental factors such as temperature and humidity, which can significantly affect particle flow and orientation, thereby impacting the models' industrial relevance. Future research should adopt experimental methods similar to ours or complementary ones for more accurate and scalable DEM modelling solutions. Future studies could explore LS-DEM and advanced discrete element methods (DEM) to better simulate irregular grain assemblies and their interactions, addressing the limitations of conventional DEM and allowing for more flexible representation of complex particle shapes.

Broadening the scope of experimental investigations is critical. Incorporating advanced imaging technologies alongside X-ray rheography could refine the analysis of granular mixing. One promising technology could be DynaTOM (De Boever et al. 2021), a new imaging system capable of capturing dynamic structural changes in granular systems. This technique offers insights that current X-ray methods can only provide through depth-projected assessments. DynaTOM could be particularly useful for examining particle aggregation scenarios affected by cohesion or moisture. Furthermore, combining X-ray rheography with DynaTOM could give a more comprehensive understanding of granular mixing, especially in solid-fluid interactions. Despite being potentially suitable only for much smaller mixers, this hybrid approach could be beneficial for applications involving suspensions or high-moisture environments, where neither DEM nor computational fluid dynamics (CFD) can adequately capture the system's behaviour.

The implications of this research extend beyond the granular mixing and may be applicable in various fields. In geotechnical engineering, insight into granular flow in moist environments can improve soil stability assessments and landslide prediction models. Similarly, optimising mixing conditions for cohesive powders in pharmaceutical production can improve drug formulation processes. The food processing sector could also benefit from better modelling of granular mixing under moisture-rich conditions, such as during dough kneading or grain fermentation. Future research efforts should promote interdisciplinary collaborations integrating materials science, physics, and computational modelling expertise to drive innovation in these areas.

In the long term, this research sets the groundwork for developing autonomous monitoring systems that use advanced imaging and artificial intelligence (AI) - driven analytics to optimise granular mixing processes in real time. Such innovations can reduce material waste, improve

efficiency, and promote sustainable industrial practices. This study represents a crucial step in integrating experimental and computational methods to investigate granular mixing. However, future research must focus on advancing imaging technologies, computational simulations, and interdisciplinary applications to fully understand and improve granular mixing in diverse fields.

thesis

# Bibliography


Abbaspour-Fard, Mohammad Hossein (2000). 'Discrete element modelling of the dynamic behaviour of non-spherical particulate materials'. PhD thesis. Newcastle University.

Ai, Jun et al. (2011). 'Assessment of rolling resistance models in discrete element simulations'. In: *Powder Technology* 206.3, pp. 269–282.

Alizadeh, Ebrahim, Francois Bertrand and Jamal Chaouki (2014). 'Comparison of DEM results and Lagrangian experimental data for the flow and mixing of granules in a rotating drum'. In: *AIChE Journal* 60.1, pp. 60–75.

Andreotti, Bruno, Yoël Forterre and Olivier Pouliquen (2013). *Granular media: between fluid and solid*. Cambridge University Press.

Athanassiadis, Athanasios G et al. (2014). 'X-ray tomography system to investigate granular materials during mechanical loading'. In: *Review of Scientific Instruments* 85.8.

Bagster, DF and J Bridgwater (1967). 'The measurement of the force needed to move blades through a bed of cohesionless granules'. In: *Powder Technology* 1.4, pp. 189–198.

Bai, L, QJ Zheng and AB Yu (2017). 'FEM simulation of particle flow and convective mixing in a cylindrical bladed mixer'. In: *Powder Technology* 313, pp. 175–183.

Baker, James et al. (2018). 'X-ray rheography uncovers planar granular flows despite non-planar walls'. In: *Nature communications* 9.1, p. 5119.

Baker, James Lindsay and Itai Einav (2021). 'Deep velocimetry: Extracting full velocity distributions from projected images of flowing media'. In: *Experiments in Fluids* 62, pp. 1–18.

Barr, Alan H (1981). 'Superquadrics and angle-preserving transformations'. In: *IEEE Computer graphics and Applications* 1.01, pp. 11–23.

Baxter, G William et al. (1989). 'Pattern formation in flowing sand'. In: *Physical review letters* 62.24, p. 2825.

Bhattacharya, Sayantan and Pavlos P Vlachos (2020). 'Volumetric particle tracking velocimetry (PTV) uncertainty quantification'. In: *Experiments in Fluids* 61, pp. 1–18.

Bigun, Josef (1987). *Optimal orientation detection of linear symmetry*.

Boonkanokwong, Veerakiet (2018). 'Dynamics and scale-up of cohesionless and cohesive granular flows in a bladed mixer'. PhD thesis. Rutgers University-School of Graduate Studies.

Boonkanokwong, Veerakiet et al. (2016). 'The effect of the number of impeller blades on granular flow in a bladed mixer'. In: *Powder technology* 302, pp. 333–349.

Börzsönyi, Tamás et al. (2016). 'Packing, alignment and flow of shape-anisotropic grains in a 3D silo experiment'. In: *New Journal of Physics* 18.9, p. 093017.

Bridgwater, J (1976). 'Fundamental powder mixing mechanisms'. In: *Powder Technology* 15.2, pp. 215–236.

Bridgwater, J et al. (1969). 'Geometric and dynamic similarity in particle mixing'. In: *Powder Technology* 2.4, pp. 198–206.

Bridgwater, John (2003). 'The dynamics of granular materials–towards grasping the fundamentals'. In: *Granular Matter* 4, pp. 175–181.

Brodu, Nicolas, Joshua A Dijksman and Robert P Behringer (2015). 'Spanning the scales of granular materials through microscopic force imaging'. In: *Nature communications* 6.1, p. 6361.

Brücker, Ch (1997). '3D scanning PIV applied to an air flow in a motored engine using digital high-speed video'. In: *Measurement Science and Technology* 8.12, p. 1480.

Capece, M, RN Davé and E Bilgili (2015). 'On the origin of non-linear breakage kinetics in dry milling'. In: *Powder technology* 272, pp. 189–203.

Cleary, Paul W (2000). 'DEM simulation of industrial particle flows: case studies of dragline excavators, mixing in tumblers and centrifugal mills'. In: *Powder technology* 109.1-3, pp. 83–104.

— (2010). 'DEM prediction of industrial and geophysical particle flows'. In: *Particuology* 8.2, pp. 106–118.

Conway, Stephen L et al. (2005). 'Granular flow and segregation in a four-bladed mixer'. In: *Chemical Engineering Science* 60.24, pp. 7091–7107.

Cundall, Peter A (1988). 'Formulation of a three-dimensional distinct element model—Part I. A scheme to detect and represent contacts in a system composed of many polyhedral blocks'. In: *International journal of rock mechanics and mining sciences & geomechanics abstracts*. Vol. 25. 3. Elsevier, pp. 107–116.

Cundall, Peter A and Otto DL Strack (1979). 'A discrete numerical model for granular assemblies'. In: *geotechnique* 29.1, pp. 47–65.

De Boever, Wesley et al. (2021). 'Dynamic micro-CT: Nondestructive imaging in the fourth dimension'. In: *Microscopy & Analysis, EMEA ed., Nanotechnology Supplement*, S4–S6.

Desrues, Jacques et al. (1996). 'Void ratio evolution inside shear bands in triaxial sand specimens studied by computed tomography'. In: *Géotechnique* 46.3, pp. 529–546.

Dijksman, Joshua A et al. (2012). 'Invited article: Refractive index matched scanning of dense granular materials'. In: *Review of Scientific Instruments* 83.1.

Dubsky, S et al. (2010). 'Computed tomographic x-ray velocimetry'. In: *Applied Physics Letters* 96.2.

Ehrichs, EE et al. (1995). 'Granular convection observed by magnetic resonance imaging'. In: *Science* 267.5204, pp. 1632–1634.

Elsinga, Gerrit E et al. (2006). 'Tomographic particle image velocimetry'. In: *Experiments in fluids* 41.6, pp. 933–947.

Gallas, Brandon D et al. (2004). 'An energy-and depth-dependent model for x-ray imaging: Energy-and depth-dependent x-ray imaging'. In: *Medical physics* 31.11, pp. 3132–3149.

Goldhirsch, Isaac (2010). 'Stress, stress asymmetry and couple stress: from discrete particles to continuous fields'. In: *Granular Matter* 12.3, pp. 239–252.

Govender, Nicolin et al. (2018). 'Large-scale GPU based DEM modeling of mixing using irregularly shaped particles'. In: *Advanced Powder Technology* 29.10, pp. 2476–2490.

Grudzień, Krzysztof et al. (2011). 'Quantitative estimation of volume changes of granular materials during silo flow using X-ray tomography'. In: *Chemical Engineering and Processing: Process Intensification* 50.1, pp. 59–67.

Guillard, François, Benjy Marks and Itai Einav (2017). 'Dynamic X-ray radiography reveals particle size and shape orientation fields during granular flow'. In: *Scientific reports* 7.1, p. 8155.

Guo, Yu et al. (2017). 'Predicting breakage of high aspect ratio particles in an agitated bed using the Discrete Element Method'. In: *Chemical Engineering Science* 158, pp. 314–327.

Hall, Stephen A et al. (2010). 'Discrete and continuum analysis of localised deformation in sand using X-ray $\mu$CT and volumetric digital image correlation'. In: *Géotechnique* 60.5, pp. 315–322.

Hamilton, William Rowan (1844). 'Ii. on quaternions; or on a new system of imaginaries in algebra'. In: *The London, Edinburgh, and Dublin Philosophical Magazine and Journal of Science* 25.163, pp. 10–13.

Han, Endao, Ivo R Peters and Heinrich M Jaeger (2016). 'High-speed ultrasound imaging in dense suspensions reveals impact-activated solidification due to dynamic shear jamming'. In: *Nature communications* 7.1, p. 12243.

Hare, CL and M Ghadiri (2013). 'Influence of measurement cell size on predicted attrition by the Distinct Element Method'. In: *Powder technology* 236, pp. 100–106.

Hasan, A and KA Alshibli (2010). 'Experimental assessment of 3D particle-to-particle interaction within sheared sand using synchrotron microtomography'. In: *Géotechnique* 60.5, pp. 369–379.

Havlica, J et al. (2015). 'The effect of rotational speed on granular flow in a vertical bladed mixer'. In: *Powder technology* 280, pp. 180–190.

Hill, Kimberly M, Arvind Caprihan and James Kakalios (1997a). 'Bulk segregation in rotated granular material measured by magnetic resonance imaging'. In: *Physical Review Letters* 78.1, p. 50.

Hill, KM, A Caprihan and J Kakalios (1997b). 'Axial segregation of granular media rotated in a drum mixer: Pattern evolution'. In: *Physical Review E* 56.4, p. 4386.

Huang, N et al. (2005). 'Flow of wet granular materials'. In: *Physical review letters* 94.2, p. 028301.

Jackson, Daphne F and David J Hawkes (1981). 'X-ray attenuation coefficients of elements and mixtures'. In: *Physics Reports* 70.3, pp. 169–233.

Kähler, Christian J and Jürgen Kompenhans (2000). 'Fundamentals of multiple plane stereo particle image velocimetry'. In: *Experiments in Fluids* 29.Suppl 1, S070–S077.

Katti, Girish, Syeda Arshiya Ara and Ayesha Shireen (2011). 'Magnetic resonance imaging (MRI)–A review'. In: *International journal of dental clinics* 3.1, pp. 65–70.

Katz, Joseph and Jian Sheng (2010). 'Applications of holography in fluid mechanics and particle dynamics'. In: *Annual review of fluid mechanics* 42, pp. 531–555.

Kawaguchi, Toshihiro, Kenji Tsutsumi and Yutaka Tsuji (2006). 'MRI measurement of granular motion in a rotating drum'. In: *Particle & Particle Systems Characterization* 23.3-4, pp. 266–271.

Keane, Richard D and Ronald J Adrian (1992). 'Theory of cross-correlation analysis of PIV images'. In: *Applied scientific research* 49, pp. 191–215.

Kerur, BR, SR Thontadarya and B Hanumaiah (1991). 'A novel method for the determination of x-ray mass attenuation coefficients'. In: *International journal of radiation applications and instrumentation. Part A. Applied radiation and isotopes* 42.6, pp. 571–575.

Kloss, Christoph et al. (2012). 'Models, algorithms and validation for opensource DEM and CFD–DEM'. In: *Progress in Computational Fluid Dynamics, an International Journal* 12.2-3, pp. 140–152.

Kou, Binquan et al. (2017). 'Granular materials flow like complex fluids'. In: *Nature* 551.7680, pp. 360–363.

Kremmer, M and JF Favier (2001). 'A method for representing boundaries in discrete element modelling—part I: Geometry and contact detection'. In: *International Journal for Numerical Methods in Engineering* 51.12, pp. 1407–1421.

Krinitzsky, EL (1970). 'Radiography in the earth sciences and soil mechanics'. In.

Kruggel-Emden, H et al. (2008). 'A study on the validity of the multi-sphere Discrete Element Method'. In: *Powder Technology* 188.2, pp. 153–165.

Laurent, BFC, J Bridgwater and DJ Parker (2000). 'Motion in a particle bed agitated by a single blade'. In: *AIChE journal* 46.9, pp. 1723–1734.

Lee, Sang Joon, Han Wook Park and Sung Yong Jung (2014). 'Usage of CO2 microbubbles as flow-tracing contrast media in X-ray dynamic imaging of blood flows'. In: *Journal of Synchrotron Radiation* 21.5, pp. 1160–1166.

Lee, Sang-Joon and Guk-Bae Kim (2003). 'X-ray particle image velocimetry for measuring quantitative flow information inside opaque objects'. In: *Journal of Applied Physics* 94.5, pp. 3620–3623.

Lekhal, Azzeddine et al. (2006). 'Characterization of granular flow of wet solids in a bladed mixer'. In: *AIChE journal* 52.8, pp. 2757–2766.

Litster, James Donald et al. (2002). 'Scale-up of mixer granulators for effective liquid distribution'. In: *Powder Technology* 124.3, pp. 272–280.

Liu, Xiaoyan et al. (2017). 'DEM study on the surface mixing and whole mixing of granular materials in rotary drums'. In: *Powder technology* 315, pp. 438–444.

Lucy, Leon B (1977). 'A numerical approach to the testing of the fission hypothesis'. In: *Astronomical Journal, vol. 82, Dec. 1977, p. 1013-1024.* 82, pp. 1013–1024.

Lueptow, RM, A Akonur and TJEiF Shinbrot (2000). 'PIV for granular flows'. In: *Experiments in Fluids* 28.2, pp. 183–186.

Marigo, M et al. (2013). 'Application of Positron Emission Particle Tracking (PEPT) to validate a Discrete Element Method (DEM) model of granular flow and mixing in the Turbula mixer'. In: *International journal of pharmaceutics* 446.1-2, pp. 46–58.

Markauskas, Darius et al. (2010). 'Investigation of adequacy of multi-sphere approximation of elliptical particles for DEM simulations'. In: *Granular Matter* 12, pp. 107–123.

Mateo-Ortiz, Daniel and Rafael Méndez (2015). 'Relationship between residence time distribution and forces applied by paddles on powder attrition during the die filling process'. In: *Powder technology* 278, pp. 111–117.

Mathews, Jonathan P et al. (2017). 'A review of the application of X-ray computed tomography to the study of coal'. In: *Fuel* 209, pp. 10–24.

Metzger, Matthew J, Brenda Remy and Benjamin J Glasser (2011). 'All the Brazil nuts are not on top: Vibration induced granular size segregation of binary, ternary and multi-sized mixtures'. In: *Powder technology* 205.1-3, pp. 42–51.

Miller, Thomas et al. (2013). 'Eddy viscosity in dense granular flows'. In: *Physical review letters* 111.5, p. 058002.

Morin, Pierre (1988). 'Density of granular materials derived from X-ray photographs: calibration, reliability, and recommended procedures'. In: *Canadian Geotechnical Journal* 25.3, pp. 488–499.

Mottram, Nigel J and Christopher JP Newton (2014). 'Introduction to Q-tensor theory'. In: *arXiv preprint arXiv:1409.3542*.

Mueth, Daniel M et al. (2000). 'Signatures of granular microstructure in dense shear flows'. In: *Nature* 406.6794, pp. 385–389.

Muzzio, Fernando J et al. (2003). 'Solids mixing'. In: *Handbook of Industrial Mixing: Science and Practice*, pp. 887–985.

Nadler, B, F Guillard and I Einav (2018). 'Kinematic model of transient shape-induced anisotropy in dense granular flow'. In: *Physical review letters* 120.19, p. 198003.

Nakagawa, Masami et al. (1993). 'Non-invasive measurements of granular flows by magnetic resonance imaging'. In: *Experiments in fluids* 16, pp. 54–60.

Nedderman, RM and C Laohakul (1980). 'The thickness of the shear zone of flowing granular materials'. In: *Powder Technology* 25.1, pp. 91–100.

Novosad, J (1964). 'Studies on granular materials. I. Kinematics of granular materials mixed by a mechanical impeller'. In: *Collection of Czechoslovak Chemical Communications* 29.11, pp. 2681–2696.

— (1968). 'Studies on granular materials. V. Experimental determination of movement of granular materials mixed by a mechanical impeller'. In: *Collection of Czechoslovak Chemical Communications* 33.12, pp. 4164–4170.

Ottino, Julio M and Devang V Khakhar (2000). 'Mixing and segregation of granular materials'. In: *Annual review of fluid mechanics* 32.1, pp. 55–91.

Pellico, Juan et al. (2024). 'In vivo real-time positron emission particle tracking (PEPT) and single particle PET'. In: *Nature Nanotechnology*, pp. 1–9.

Penn, Alexander et al. (2017). 'Real-time probing of granular dynamics with magnetic resonance'. In: *Science advances* 3.9, e1701879.

Podlozhnyuk, Alexander, Stefan Pirker and Christoph Kloss (2017). 'Efficient implementation of superquadric particles in discrete element method within an open-source framework'. In: *Computational Particle Mechanics* 4, pp. 101–118.

Pourdeyhimi, B, R Dent and H Davis (1997). 'Measuring fiber orientation in nonwovens part III: Fourier transform'. In: *Textile Research Journal* 67.2, pp. 143–151.

Prasad, Ajay K (2000). 'Stereoscopic particle image velocimetry'. In: *Experiments in fluids* 29.2, pp. 103–116.

Remy, Brenda, Benjamin J Glasser and Johannes G Khinast (2010a). 'The effect of mixer properties and fill level on granular flow in a bladed mixer'. In: *AIChE journal* 56.2, pp. 336–353.

Remy, Brenda, Johannes G Khinast and Benjamin J Glasser (2009). 'Discrete element simulation of free flowing grains in a four-bladed mixer'. In: *AIChE Journal* 55.8, pp. 2035–2048.

Remy, Brenda et al. (2010b). 'Experiments and simulations of cohesionless particles with varying roughness in a bladed mixer'. In: *Chemical Engineering Science* 65.16, pp. 4557–4571.

Rognon, Pierre G et al. (2015). 'Long-range wall perturbations in dense granular flows'. In: *Journal of Fluid Mechanics* 764, pp. 171–192.

Rognon, Pierre Grégoire, Itai Einav and Cyprien Gay (2011). 'Flowing resistance and dilatancy of dense suspensions: lubrication and repulsion'. In: *Journal of Fluid Mechanics* 689, pp. 75–96.

Royer, John R et al. (2005). 'Formation of granular jets observed by high-speed X-ray radiography'. In: *Nature Physics* 1.3, pp. 164–167.

Saadatfar, Mohammad et al. (2012). 'Mapping forces in a 3D elastic assembly of grains'. In: *Journal of the Mechanics and Physics of Solids* 60.1, pp. 55–66.

Sanvitale, Nicoletta and Elisabeth T Bowman (2016). 'Using PIV to measure granular temperature in saturated unsteady polydisperse granular flows'. In: *Granular Matter* 18, pp. 1–12.

Sanvitale, Nicoletta, Claudio Gheller and Elisabeth Bowman (2022). 'Deep learning assisted particle identification in photoelastic images of granular flows'. In: *Granular Matter* 24.2, p. 65.

Shinbrot, Troy, Keirnan LaMarche and Benjamin J Glasser (2006). 'Triboelectrification and razorbacks: geophysical patterns produced in dry grains'. In: *Physical review letters* 96.17, p. 178002.

Slominski, Cezary, Maciej Niedostatkiewicz and Jacek Tejchman (2007). 'Application of particle image velocimetry (PIV) for deformation measurement during granular silo flow'. In: *Powder Technology* 173.1, pp. 1–18.

Stannarius, Ralf (2017). 'Magnetic resonance imaging of granular materials'. In: *Review of Scientific Instruments* 88.5.

Stewart, RL, J Bridgwater and DJ Parker (2001). 'Granular flow over a flat-bladed stirrer'. In: *Chemical Engineering Science* 56.14, pp. 4257–4271.

Tahvildarian, Parisa, Farhad Ein-Mozaffari and Simant R Upreti (2013). 'Circulation intensity and axial dispersion of non-cohesive solid particles in a V-blender via DEM simulation'. In: *Particuology* 11.6, pp. 619–626.

Taillandier-Thomas, Thibault, Stéphane Roux and François Hild (2016). 'Soft route to 4D tomography'. In: *Physical review letters* 117.2, p. 025501.

Weinhart, Thomas et al. (2012). 'From discrete particles to continuum fields near a boundary'. In: *Granular Matter* 14, pp. 289–294.

Westerweel, Jerry, Gerrit E Elsinga and Ronald J Adrian (2013). 'Particle image velocimetry for complex and turbulent flows'. In: *Annual Review of Fluid Mechanics* 45, pp. 409–436.

Wiederseiner, Sébastien et al. (2011). 'Refractive-index and density matching in concentrated particle suspensions: a review'. In: *Experiments in fluids* 50, pp. 1183–1206.

Windows-Yule, CRK et al. (2014). 'Effects of packing density on the segregative behaviors of granular systems'. In: *Physical review letters* 112.9, p. 098001.

Windows-Yule, CRK et al. (2022). 'Recent advances in positron emission particle tracking: A comparative review'. In: *Reports on Progress in Physics* 85.1, p. 016101.

Zhou, Y C, A B Yu and J Bridgwater (2003). 'Segregation of binary mixture of particles in a bladed mixer'. In: *Journal of Chemical Technology & Biotechnology: International Research in Process, Environmental & Clean Technology* 78.2-3, pp. 187–193.

Zhou, YC et al. (2004). 'Microdynamic analysis of the particle flow in a cylindrical bladed mixer'. In: *Chemical engineering science* 59.6, pp. 1343–1364.

Zhou, Yincai (2002). ‘Granular dynamics with special reference to piling and mixing processes’. PhD thesis. UNSW Sydney.

Zhu, HP et al. (2008). ‘Discrete particle simulation of particulate systems: a review of major applications and findings’. In: *Chemical Engineering Science* 63.23, pp. 5728–5770.